

Accuracy and Acceleration of Arterial Spin Labeling in
Magnetic Resonance Imaging

A Dissertation

Presented to

the faculty of the School of Engineering and Applied Science

University of Virginia

in partial fulfillment

of the requirements for the degree

Doctor of Philosophy

by

Li Zhao

August

2014

APPROVAL SHEET

The dissertation
is submitted in partial fulfillment of the requirements
for the degree of
Doctor of Philosophy



AUTHOR

The dissertation has been read and approved by the examining committee:

Craig H. Meyer

Advisor

John A. Hossack

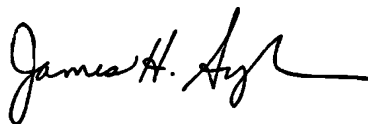
Max Wintermark

John P. Mugler, III

Frederick H. Epstein

Christopher M. Kramer

Accepted for the School of Engineering and Applied Science:



Dean, School of Engineering and Applied Science

August

2014

Abstract

Cerebral perfusion imaging provides information about the blood supply of tissue. It reveals functional changes of the brain before and after structural changes, which can be used to improve the sensitivity and accuracy of stroke and tumor diagnosis. There has been an increasing interest in developing methods for non-contrast perfusion imaging, because of the risk of nephrogenic systemic fibrosis (NSF) in patients with kidney dysfunction and the need for repeated blood flow measurements in a short period of time for functional studies. Magnetic resonance imaging (MRI) provides a safer option for perfusion imaging without a contrast agent: arterial spin labeling (ASL). In this work, we propose several new techniques to improve the quality and quantification of ASL MRI.

Using the water spins of blood as a tracer makes ASL safer than other perfusion imaging methods, but also results in a low signal-noise-ratio (SNR). Conventionally, ASL uses lengthy scan times to improve image quality and compensate for motion. However, this strategy is typically used to measure the perfusion bolus at a single time point, which can limit the accuracy of perfusion quantification, particularly in the setting of disease. Measuring multiple time points, which is called dynamic ASL, can improve quantification of cerebral

blood flow (CBF) and yield additional information, but long scan times may be needed. In this work, we describe the following advances that can be used to improve dynamic ASL: (1) accurate reference T_2 mapping; (2) robust and rapid single-shot data acquisition; (3) dynamic model-based image reconstruction; and (4) optimal experiment design.

As a parameter estimation problem, CBF is quantified based on other reference parameters, such as T_1 and T_2 . Here, I introduce a novel T_2 mapping paradigm, which combines the conventional image reconstruction and parameter regression steps into one state tracking step. Using the unscented Kalman filter (UKF), the proposed method uses a T_2 decay model to estimate T_2 information from k-space data directly and efficiently. It achieves accurate estimation up to an undersampling factor of 8, which is comparable to a compressed sensing method with model-based sparsity. This new paradigm can be adapted to Cartesian and non-Cartesian trajectories, and other parameter mapping models.

In order to improve ASL image quality, a rapid and robust ASL sequence was developed with a combined parallel and compressed sensing image reconstruction. Pseudo continuous radio frequency (RF) pulses are used to tag the proximal blood. A 3D turbo spin echo sequence with stack-of-spiral readouts [1] is used to acquire k-space data. Additionally, pulsatile motion artifacts are corrected by exploiting the redundancy among multiple receiver coils. A dual-density spiral trajectory is used to achieve single-shot imaging, which improves the SNR and freezes motion. ASL image quality and SNR are further improved by parallel reconstruction with spatial sparsity constraints.

Accurate CBF mapping requires dynamic ASL imaging at multiple observation times, but the scan time for each ASL image must be short if the total scan time is limited. This limits the image SNR further. However, in dynamic ASL perfusion imaging, the similar spatial

structure of images at different delay times and prior information about their temporal evolution can be exploited to improve the image quality and the estimates of perfusion parameters. By using the sparsity of dynamic ASL perfusion images in the domain of a perfusion model, we can efficiently use the relationship between different time frames and not just reconstruct each frame separately. The resulting image reconstruction suppresses both random noise and physiological motion artifacts, because they do not conform to the underlying perfusion model. The proposed method results in rapid and robust, 3D dynamic ASL imaging in a clinically practical time.

In dynamic ASL imaging, the selection of observation times can influence the accuracy of CBF quantification. We design an optimal observation time scheme based on minimization of the Cramér-Rao lower bound (CRLB). Additionally, in the low SNR situation of ASL images, noise in the magnitude image is more accurately described by a Rician model, instead of a Gaussian model. Therefore, a maximum likelihood estimator is designed based on Rician noise, which provides unbiased CBF estimation. Further, the optimal observation time scheme is designed based on Rician noise.

The main contributions described in this work attempt to extend ASL imaging from a 'static' measurement with a single post label delay to dynamic perfusion imaging with multiple observation times, which includes sequence design, reconstruction and experiment design. The state of the art in ASL is represented by 'static' clinical imaging and functional brain imaging. Dynamic perfusion imaging is another important step in the evolution of ASL. The rich information that can be obtained using dynamic perfusion imaging will be interesting to explore in the future.

Acknowledgments

If the knowledge and technique of a human being is a great forest, I have been wondering and playing in it for more than 20 years. At this time, I arrived at the edge of the forest and decided to plant my little plant here. I hope it can be a small flower or a giant tree, and can make some additional fun for the new arrivals.

Five years ago, when I decided to come to this 'new land', my primary goal was to find out my potential and capability. The first question I asked Dr. Craig Meyer was how to do research. But he didn't answer me at that moment. Maybe I should say he was showing me the answer in all of the following five years. From sequence debugging to group discussion, Craig's agile thinking, wide experience and solid knowledge have provided an excellent answer. His enthusiasm encouraged me to make progress further. What I have achieved today was what he pointed out before. More importantly, Dr. Meyer is always ready to support me with all his resources and suggestions, and meanwhile leaves me plenty of free time to discover my interests. This working style gave me the opportunity to exploit the problem myself and learn the strategy to solve an unknown problem. More importantly, it gave me the time to think about what the research should be, not only what it is required

to be. I have spent plenty of time doing something interesting, even it may be not useful right away. Like playing in the forest, you never know what is the fun of climbing the next tree or what is the next animal you will meet. Realists build the life, and idealists give the direction of life. I think this free working style is the latter one. Because of this freedom, I come to the idea of T_2 mapping by Kalman filter. No matter how this method will go in the future, it already makes a valuable moment in my Ph.D life. Therefore, Dr. Meyer is the first one that I have to say thanks sincerely.

I also need to thank Dr. Kui Ying in Tsinghua University, who introduced me into the MRI and taught me the first MRI principles. I need to thank Dr. Lei Zhao in XinaoMDT Co., who gave the first vision and determination of research work.

I also would like to thank Dr. Max Wintermark so much. He guided me and worked with me in the whole arterial spin labeling project. Dr. Wintermark taught me a lot of basic knowledge of brain physiology and stroke pathology, which helps me bridge the gap between technique development and clinical requirements.

I must thank Dr. John Mugler, who gave me a lot of important suggestions on sequence design and RF pulse design. I would like to thank Dr. Wilson Miller, too, who led me into the area of MR thermometry and helped me with every experiment.

I also would like to thank Dr. Fred Epstein. His experience in perfusion experiments helped me make significant progress in the early ASL work and his course helped me to further understand the variants and beauty of MR. I also thank Dr. John Hossack and Dr. Christopher Kramer for their service on my committee and their valuable suggestions over the years.

Thanks to all of my colleagues in the MR groups of the University of Virginia. Dr.

Xue Feng taught me a lot about spiral acquisition and reconstruction. Yang Yang gave great suggestions about ASL tagging pulse design. Xiao Chen introduced me to the field of compressed sensing. Dr. Samuel Fielden greatly supported me in the sequence design of 3D ASL and MR thermometry. Dr. Meihan Wang helped me develop the ASL sequence. Dr. Ken Johnson helped me on the spiral image reconstruction. Nivedita Naresh and Bhairav Mehta gave wide discussions on the perfusion imaging and compressed sensing. Dr. Patrick Antkowiak helped me understand ASL models. Sometimes, I even asked a specific question about details, such as 'which value should I use'. These guys always showed patience and enthusiasm, and helped me figure out the problem. I have to say I learned most of the practical skills from these colleagues.

I would like to thank the previous graduate students in Dr. Meyer's lab. Drs. Peng Hu, Chris Sica, Weitian Chen, and Hao Tan. All your great former work built the essential foundation of this dissertation.

I must thank Dr. Cheng Ouyang from University of Illinois at Urbana-Champaign. We discussed the details of ASL sequence design and methods to test ASL imaging many times. She shared her experience generously and gave me many practical suggestions. I also must thank Li Cheng from University of Pennsylvania. We discussed almost everything in MRI, from compressed sensing to thermometry, from sequence design to any new topic in MR. His wide erudition and deep insight always helped me find the way to solve problems.

My family gave me priceless support and understanding of my Ph.D work. Xi Li, my wife, your kindness, your wisdom, and your smile give me bravery and strength. Your presence makes my life so colorful and meaningful. Thank you for being here with me. Thank you for completing me.

Contents

Abstract	ii
Acknowledgments	v
Table of Contents	xii
List of Figures	xv
List of Tables	xvi
1 Introduction	1
1.1 Background	2
1.2 Magnetic Resonance Imaging	3
1.3 Perfusion	5
1.4 Arterial Spin Labeling	7
1.4.1 The Perfusion Model of ASL	7
1.4.2 Simplification of ASL Model	13
1.4.3 Measurement of M_0	14

<i>CONTENTS</i>	ix
1.4.4 Arterial Input Function	15
1.4.5 ASL Sequence	15
1.4.6 Problems in ASL	18
1.5 Dissertation Overview	19
2 Accelerated T_2 mapping	22
2.1 Introduction	22
2.2 Theory	24
2.2.1 Kalman Filter	24
2.2.2 T_2 Signal Model	26
2.2.3 Unscented Kalman Filter	27
2.2.4 Multiple-Channel Data	30
2.2.5 Two-Parameter Estimation	30
2.2.6 Parameter Initialization	31
2.3 Methods	32
2.3.1 Simulation	32
2.3.2 Experiments	33
2.4 Results	35
2.4.1 Simulations	35
2.4.2 Experiments	36
2.5 Discussion	40
2.6 Conclusion	46
3 Robust ASL with a Single PLD	47

3.1	Introduction	48
3.2	Sequence Design	49
3.2.1	3D Acquisition	49
3.2.2	Tagging Pulse	50
3.3	Motion Robustness	53
3.3.1	Constant-density and Parallel Imaging	53
3.3.2	Single-shot Spiral and Parallel Imaging	58
3.4	Noise Suppression by Spatial Sparsity	61
3.5	Conclusion	66
4	Dynamic ASL	67
4.1	Introduction	68
4.2	Algorithms	70
4.2.1	Dictionary Representation	70
4.2.2	ASL Model and Over-complete Dictionary	71
4.2.3	Compressed Sensing Solver	73
4.3	Pulse-sequence Design	74
4.3.1	Blood Tagging	74
4.3.2	Vessel Suppression	76
4.3.3	Imaging Sequence	76
4.3.4	Dual Density Spiral	76
4.4	Simulation	78
4.5	In Vivo Measurements	79

<i>CONTENTS</i>	xi
4.5.1 Dynamic ASL Protocol	79
4.5.2 ASL Image Analysis	80
4.6 Results	84
4.6.1 Simulation Results	84
4.6.2 Experiments Results	87
4.7 Discussion	90
4.8 Conclusion	93
5 Optimal ASL Experiment	94
5.1 Introduction	95
5.2 Theory	96
5.2.1 Cramér-Rao Lower Bound	96
5.2.2 Gaussian Noise	98
5.2.3 Rician Noise	99
5.3 Methods	102
5.3.1 Simulation	102
5.3.2 Experiment	103
5.4 Results	104
5.5 Discussion	108
5.6 Conclusion	110
5.A Derivation of CRLB with Gaussian Noise	110
5.B Derivation pf CRLB of ASL model with Gaussian Noise	112
6 Conclusion	115

<i>CONTENTS</i>	xii
6.1 Overview of Findings	115
6.2 Future Directions	117
6.2.1 Sequence	117
6.2.2 Model-based Reconstruction	119
6.2.3 Parameter Tracking	119
6.3 Collaborations and Contributions	120
Bibliography	121

List of Figures

2.1	T_2 mapping paradigms	25
2.2	T_2 data sampling scheme in k-p-space	32
2.3	UKF performance with SNR level and number of encoding states	36
2.4	T_2 estimation with compressed sensing and UKF on numerical phantom . . .	37
2.5	Quantification of estimated T_2 map error in the simulation	38
2.6	T_2 maps from the compressed sensing and UKF methods with an ex-vivo brain phantom	39
2.7	Quantification of the T_2 maps from compressed sensing method and the two- parameter UKF method	40
2.8	T_2 maps from the compressed sensing method and the two-parameter UKF method from a volunteer scan	41
2.9	Estimation errors on retrospectively undersampled volunteer data	42
2.10	The performance of two-parameter UKF method with accelerated acquisition	42
3.1	Image acquired using a 3D TSE stack-of-spirals acquisition	50

3.2	The schematic of pCASL with 3D TSE stack of spirals	51
3.3	3D pCASL images with TSE spiral sequence	52
3.4	Point spread function for pulsatile motion	54
3.5	Single shot and multiple shot spiral in ASL.	55
3.6	SPIRiT Correction for Ring Artifacts.	57
3.7	Additional pulsatile motion correction	58
3.8	Constant-density and Dual-density Spiral	59
3.9	Single-shot dual density ASL images	60
3.10	Dual density spiral trajectory freezes motion	61
3.11	Spatial sparsity for noise suppression on numerical phantom	63
3.12	Spatial sparsity improved the structural similarity in numerical phantom	64
3.13	Spatial sparsity improves ASL images	65
4.1	Evolution of dynamic ASL signal in a numeric phantom	73
4.2	General description of model based reconstruction	75
4.3	The dual density spiral with 3D TSE	77
4.4	A general weighted delay in ATT calculation	82
4.5	The trained dictionary represents the ASL signal	84
4.6	Model based sparsity reduced motion artifacts in multiple OTs ASL images	85
4.7	Regularization parameters searching in compressed sensing	86
4.8	Simulated ASL images reconstructed by compressed sensing	86
4.9	The selected volunteer's dynamic pCASL perfusion images	89
4.10	Statistic analysis of CBF estimation residue and ASL image SNR in volunteers.	90

5.1	Improved estimation by optimal OT design	105
5.2	Biased estimation by a LS estimator with low SNR signal	105
5.3	MLE provides unbiased estimation in low SNR Rician noise	106
5.4	Comparison of optimal observation time designs	107
5.5	Optimal OTs experiment result	107

List of Tables

3.1	Neuroradiologist grading results with gridding, CS and CS-MC reconstruction	66
4.1	Observation Time Design (ms)	80
4.2	Improvement of ASL images quality and CBF map by compressed sensing. .	87
4.3	Mean rating of images and parameter maps from six volunteers in a blinded evaluation by a neuroradiologist.	90

Introduction

Cerebral perfusion imaging can improve the diagnosis of stroke and cancer, by providing hemodynamic information. However, the typical measurement with dynamic susceptibility contrast imaging (DSC) [2] is contraindicated and potentially life-threatening for patients with renal dysfunction [3, 4]. This represents a significant impediment in acute stroke patients, where approximately 25% have kidney issues, but the limited stroke therapeutic time window does not always allow time to check renal function.

Arterial spin labeling (ASL) [5, 6] with magnetic resonance imaging (MRI) is an alternative method for perfusion imaging without administering contrast material. However, ASL inherently has low signal-to-noise ratio (SNR) and is sensitive to motion artifacts. In order to achieve stable images and sufficient SNR, currently ASL imaging is limited to relatively low spatial resolution and a single post label delay (PLD) measurement, which is insufficient to fully characterize cerebral perfusion in stroke in a way that is clinically relevant.

In the following work, we will develop a method for accurate and accelerated ASL for robust and high quality perfusion images, achieving whole brain coverage in a clinically

feasible scan time.

1.1 Background

Evaluation of cerebral perfusion has gained significant importance in the modern care of stroke and brain tumor patients. Currently, cerebral perfusion is routinely assessed by contrast-enhanced CT and MR perfusion imaging. In stroke patients, this information is used to improve the sensitivity and accuracy of stroke diagnosis, exclude stroke mimics, and better assess the infarct core and collateral flow. Proper early treatment of stroke can significantly help salvageable brain tissue reperfuse and stop stroke lesion expansion. In brain tumor patients, the information is used to characterize tumor angiogenesis, monitor response to antiangiogenic agents, distinguish tumor recurrence from radiation necrosis, and differentiate between brain tumor and brain tumor mimics. Physicians can select a therapeutic approach based on perfusion imaging, which can provide cerebral information such as cerebral blood volume (CBV), cerebral blood flow (CBF), and a number of descriptors of the timing and dynamics of contrast transit through the cerebral capillary network.

However, typical perfusion measurement is performed with contrast administration, for example dynamic susceptibility contrast imaging (DSC) in MRI, which is risky for patients with acute kidney injury and chronic kidney disease at stages 4 and 5 (glomerular filtration rate < 30 mL/min/1.73m²) [4]. This is a potentially life-threatening condition that can result, if patients with severe chronic kidney disease are exposed to gadolinium. Because stroke patients tend to be elderly, there is more concern about their renal function. Usually, patients older than 65 years, are highly suggested to check renal dysfunction before being given a

contrast agent. On the other hand, because of the urgency associated with stroke, there is often not time to perform a blood draw and determine the safety of administering contrast. For all these reasons, a contrast-free perfusion imaging method would be appealing to all physicians taking care of stroke patients, especially one that could be repeated as often as needed without concern for the dose of contrast used or the renal function of the patient.

Arterial spin labeling (ASL) is a non-contrast and non-invasive perfusion imaging method with MRI. By inverting the natural blood signal in arteries using radio frequency (RF) pulses, it builds a blood bolus and can measure the hemodynamics as the bolus flows through brain. High correlation between ASL and DSC has been demonstrated [7]. Therefore, ASL can be a valuable perfusion imaging method.

1.2 Magnetic Resonance Imaging

Magnetic resonance imaging (MRI) [8] is a powerful medical imaging technique, which can provide rich anatomical and functional information from the human body. It has been widely applied clinically for a range of applications, including neuroimaging, cardiovascular imaging and musculoskeletal imaging. Comparing with other medical imaging methods, such as X-ray, computed tomography (CT) and positron emission tomography (PET), MRI has the advantages of non-ionizing radiation, flexible imaging plane orientation and excellent soft tissue contrast [9–11].

MRI is a tomographic technique that acquires local tissue information in three steps. First, polarization in a main magnetic field. In an atom, protons, electrons and neutrons all have spin. When spins are paired (e.g., an even number of neutrons and an even number

of protons), the nucleus has no overall spin. A nucleus with an odd number of neutrons and/or an odd number of protons has net spin, and thus is active in nuclear magnetic resonance (NMR). A hydrogen atom contains only one proton and its net spin has two possible orientations. Typically, the spins in body tissue have random direction, because of thermal movement. When the hydrogen atoms in the human body are exposed to a strong magnetic field, spins are lined up along the main field direction, also called the longitudinal direction. There are slightly more atoms in the parallel state along the main field than in the anti-parallel state, and thus there is net magnetization along the longitudinal direction. These spins precess about the direction of the main field at the Larmor frequency. Second, excitation by a radio frequency (RF) pulse. The MRI scanner deposits energy to the tissue of interest using an oscillating RF pulse in the transverse plane at the frequency of the spins' precession. Then, the net magnetization is precessing about RF and main field, which tips the net magnetization from the longitudinal direction to the transverse direction. Third, spatial encoding by linear gradients. After turning off the RF pulse, the net magnetization gradually returns to the longitudinal direction and releases the energy in the form of radio frequency energy. With gradient magnetic fields applied that cause the magnetic field to vary linearly in space, spins at different locations emit signals at different frequencies. These signals are collected by receiver coils and Fourier transformation is used to determine the frequency distribution, which provides information about spins at different locations.

The intensity of magnetic resonance (MR) images depends on multiple parameters of local tissue; therefore, the images can have rich contrast. The signal relaxation rates are highly correlated to pathology, such as tumors. The signal phase can indicate temperature change, which can guide focused ultrasound therapy. Deoxygenated hemoglobin attenuates

the MR signal, so MRI can reveal the oxygen consumption and neural activity in brain. The drawbacks of MRI include long scan time, low sensitivity and a noisy environment for the patient.

1.3 Perfusion

Perfusion is a physiological process by which the body delivers blood to the microvasculature, where oxygen and glucose exchange with local tissue. Some diseases can be diagnosed by this functional change before structural changes [12].

The brain metabolic rate indicates brain activity and related pathologies. This important parameter can be measured by the cerebral metabolic rate of oxygen ($CMRO_2$), which describes the amount of oxygen consumed per unit tissue per minute. Cerebral blood flow is an effective measure of brain metabolism, because of the direct relationship between $CMRO_2$ and CBF :

$$CMRO_2 = OEF \cdot CBF \cdot [O_2]_a \quad (1.1)$$

$[O_2]_a$ is the concentration of oxygen in arterial blood. It is about 8 $\mu\text{mol/mL}$. CBF describes the volume of blood that moves through vessels per minute. It is about 50 ml/100g tissue/minute for gray matter and about 1/3 of that level for white matter. Skeletal muscle perfusion is about 1/10 that of gray matter CBF at rest and reaches 80 ml/100g/minute during exercise. OEF is oxygen extraction fraction, which describes the fraction of oxygen that leaves blood and metabolizes glucose. It is about 40%.

How much blood is supplied to the tissue also depends on blood velocity and blood volume. Cerebral blood volume (CBV) describes the fraction of tissue volume occupied

by blood vessels. It is about 4%. CBV is composed of an arterial portion (aCBV), a capillary portion and a venous portion. Blood velocity is pulsatile in the large vessels, with a periodicity related to the cardiac cycle. Blood velocity in capillaries is much slower (1 mm/s) and appears to be stable in the macrocosm, but is irregular in the microcosm, because of the obstruction of blood cells.

The central volume principle uses the mean transit time (MTT or τ) to connect the concepts of CBF and CBV:

$$CBV = \tau \cdot CBF \quad (1.2)$$

The typical value of τ is 4 s.

Several methods have been used to measure CBF, including positron emission tomography (PET), Doppler ultrasound, dynamic susceptibility contrast MRI and ASL[13]. In DSC MRI, the introduced contrast agent induces a signal drop. The kinetic signal change can be described as a sum over the past history of delivery to the local tissue weighted by the fraction that remains in the voxel:

$$\begin{aligned} C &= CBF \cdot \int_0^t AIF(t') \cdot r(t' - t) dt' \\ &= CBF \cdot AIF * r \end{aligned} \quad (1.3)$$

where C is the concentration of contrast agent; r is the residue function, which describes the fraction of contrast delivered at time t' and still in the image voxel at observation time t ; and $*$ is the convolution operator.

This model assumes that the contrast agent achieves equilibrium immediately when it arrives at local tissue. It is referred to as a single compartment model. This framework

can also be used as the foundation of ASL model development [14]. More complex models have also been developed that include transport between tissue and the microvascular bed, including two compartment models [15] and four compartment models [16]. However, in ASL imaging, low SNR and time-consuming scans limit the information that can be detected in a practical experiment, and thus the complexity of the signal model. Therefore, most researchers focus on the classic single compartment model described in the following section.

1.4 Arterial Spin Labeling

Conventional perfusion measurement can be done with PET (with ^{15}O targeted on water or glucose), SPECT (with ^{133}Xe), CT (with Xenon or Iodine) and ultrasound [13]. MRI with a contrast agent can also quantify perfusion. ASL uses freely diffusable water as a tracer instead of an exogenous contrast agent.

1.4.1 The Perfusion Model of ASL

Here, we will derive the ASL signal model [6, 14] from the Bloch equations [5].

The basic Bloch equation is

$$\frac{d\mathbf{M}}{dt} = \mathbf{M} \times \gamma \mathbf{B} - \frac{M_x \mathbf{i} + M_y \mathbf{j}}{T_2} + \frac{M_0 - M_z}{T_1} \mathbf{k} \quad (1.4)$$

where \mathbf{i} , \mathbf{j} and \mathbf{k} are unit vectors; \mathbf{M} is the magnetization vector; \mathbf{B} is the magnetic field; and M_0 is the equilibrium magnetization, which is along the direction of the main magnetic field. T_1 is longitudinal relaxation time and T_2 is transversal relaxation time.

When we only consider the longitudinal magnetization recovery along \mathbf{k} direction, the

Bloch equation can be simplified as

$$\frac{dM}{dt} = \frac{M_0 - M}{T_1}. \quad (1.5)$$

Additionally, when we consider the blood flow and the static tissue [6] together, it becomes

$$\frac{dM}{dt} = \frac{M_0 - M}{T_1} + f(M_a - M_v) \quad (1.6)$$

where M is the longitudinal magnetization; M_a is the magnetization of arterial inflow blood per ml; M_v is the magnetization of venous outflow blood per ml; and f is the blood flow, with units of ml/100g tissue/min.

We will assume a single compartment model, where blood and tissue exchange and achieve equilibrium immediately [6]. Thus, the magnetization in the vein is proportional to the spins in the tissue:

$$M_v = \frac{M}{\lambda} \quad (1.7)$$

where λ is the partition coefficient, which describes the ratio of water per gram of brain tissue to water per gram of blood.

Therefore, the equation becomes

$$\frac{dM}{dt} = \frac{M_0 - M}{T_1} + fM_a - \frac{f}{\lambda}M. \quad (1.8)$$

To image blood flow, we collect two sets of data in ASL imaging: one with ‘labeled’ blood, where the spin in blood is inverted or saturated, and the other with ‘control’ blood, where

the spin is positive (although maybe not fully recovered, because of a limited repetition time). These two sets of signal are described by the following equations:

$$\frac{dM_{label}}{dt} = \frac{M_0 - M_{label}}{T_1} + fM_{a,label} - \frac{f}{\lambda}M_{label} \quad (1.9)$$

$$\frac{dM_{control}}{dt} = \frac{M_0 - M_{control}}{T_1} + fM_{a,control} - \frac{f}{\lambda}M_{control} \quad (1.10)$$

where $M_{a,label}$ and $M_{a,control}$ are the arterial input blood signal in the label and control scans, respectively; and M_{label} and $M_{control}$ are the tissue signal in label and control scans.

To show the perfusion signal and eliminate the background signal from static tissue, the label image is subtracted from the control image. Let us define ΔM as the perfusion contrast:

$$\Delta M = M_{control} - M_{label} . \quad (1.11)$$

The subtraction of Eqs. 1.9 and 1.10 results in the following equation:

$$\frac{d\Delta M}{dt} = -\Delta M \left(\frac{1}{T_1} + \frac{f}{\lambda} \right) + f(M_{a,control} - M_{a,label}) \quad (1.12)$$

Now let us define

$$\frac{1}{T} = \frac{1}{T_1} + \frac{f}{\lambda} , \quad (1.13)$$

which is the ‘apparent T_1 ’, including blood flow.

Define arterial blood function A :

$$A = M_{a,control} - M_{a,label} \quad (1.14)$$

This can be expressed as

$$A = 2\alpha M_0 f a * m \quad (1.15)$$

where α is the labeling efficiency, and $0 < \alpha < 1$ with 1 corresponding to a fully inverted blood signal. a is a dispersion kernel, describing the shape of the labeled blood bolus, normalized to 1. m is the decay of inverted blood signal:

$$m = e^{-t/T_{1b}} \quad (1.16)$$

T_{1b} is the T_1 of blood. t is the time the labeled blood arrives at the local tissue. In pulsed ASL, the labeled region is wide, so the blood arriving at the image plane has experienced different amounts of signal recovery, according to the imaging time t . In pseudo continuous ASL (pCASL), the labeling plane (about 30 mm) is thinner than pulsed ASL (PASL), where global inversion is implemented in most cases. Labeled blood in pCASL can be simplified by a constant recovery time when it arrives at the image plane. This time is usually referred to as the arterial transit time (ATT or Δt).

If we ignore the dispersion of the blood bolus and assume $a = 1$, then for pCASL

$$A = 2\alpha M_0 f e^{-\Delta t/T_{1b}} \quad (1.17)$$

The original equation 1.12 becomes

$$\frac{d\Delta M}{dt} + \frac{\Delta M}{T} = A \quad (1.18)$$

This is a standard first-order ordinary differential equation (ODE), and the solution is derived as follows.

Define μ , which satisfies:

$$\frac{d\mu\Delta M}{dt} = \mu A \quad (1.19)$$

It means:

$$\mu \frac{d\Delta M}{dt} + \Delta M \frac{d\mu}{dt} = \mu A \quad (1.20)$$

Dividing by μ on both sides:

$$\frac{d\Delta M}{dt} + \Delta M \frac{1}{\mu} \frac{d\mu}{dt} = A \quad (1.21)$$

Therefore, to satisfy Eq. 1.18, μ should be chosen as

$$\frac{1}{\mu} \frac{d\mu}{dt} = \frac{1}{T} \quad (1.22)$$

The solution is

$$\mu = e^{t/T} \quad (1.23)$$

The ODE Eq.1.19 is solved as follows:

$$\begin{aligned} \Delta M &= \frac{1}{\mu} \int \mu A dt \\ &= e^{-t/T} \int_{lb}^{ub} e^{t/T} A dt \\ &= ATQ \\ &= 2\alpha M_0 f e^{-\Delta t/T_{1b}} TQ \end{aligned} \quad (1.24)$$

The lower limit of the integral, lb , is the time of arrival of the blood bolus (Δt in pCASL). The upper limit of the integral, ub , is the smaller of the observation time, t , and the end of the blood bolus, $\tau + \Delta t$. Therefore, for pCASL,

$$Q(n) = \begin{cases} 0 & \text{if } 0 < t < \Delta t \\ 1 - \exp\left(-\frac{t-\Delta t}{T}\right) & \text{if } \Delta t \leq t \leq \Delta t + \tau \\ \exp\left(-\frac{t-\tau-\Delta t}{T}\right) - \exp\left(-\frac{t-\Delta t}{T}\right) & \text{if } \Delta t + \tau < t \end{cases} \quad (1.25)$$

Similar results can be derived following the contrast perfusion model in Eq. 1.3. Including signal recovery, m , in the residue function, r , yields the following expressions:

$$R = rm \quad (1.26)$$

$$\Delta M = A * R \quad (1.27)$$

The residue function is given as [14]:

$$r = e^{-ft/\lambda} \quad (1.28)$$

Therefore, the ASL signal is expressed as:

$$\Delta M = A * (rm) \quad (1.29)$$

More details of each function and parameter will be discussed in the following sections.

1.4.2 Simplification of ASL Model

If the post-label delay (PLD) is longer than the arterial transit time, all of the labeled blood bolus has arrived at the microvascular bed at the time of signal acquisition. Under this condition, the ASL signal will be insensitive to the arterial transit time and can be quantified by a single PLD measurement. When $PLD > \Delta t$, it equals to $t > \tau + \Delta t$. The ASL signal is described by the third part of Eq. 1.24:

$$\Delta M = 2\alpha M_0 f T e^{-\Delta t/T_{1b}} \left(e^{-(t-\tau-\Delta t)/T} - e^{-(t-\Delta t)/T} \right) \quad (1.30)$$

Assume that there is little change in T_1 in the tissue by introducing the labeled blood bolus.

$$T \approx T_{1b} \quad (1.31)$$

Then, CBF can be quantified by single PLD measurement [7]:

$$\Delta M = 2\alpha M_0 f T_{1b} \left(e^{-(t-\tau)/T_{1b}} - e^{-t/T_{1b}} \right) \quad (1.32)$$

Because the difference in T_1 between blood (1650 ms) [17] and gray matter (1500 ms) [18] at 3T is less than 10%, the T_1 of brain tissue is also used in some work [19, 20]:

$$\Delta M = 2\alpha M_0 f T_{1b} \left(e^{-(t-\tau)/T_1} - e^{-t/T_1} \right) \quad (1.33)$$

1.4.3 Measurement of M_0

In a single-compartment model, when we quantify CBF, the signal is usually normalized by the M_0 of blood first. Generally, there are two methods to calculate the normalization factor: one method measures the M_0 of local tissue, then estimates the local blood signal as M_0/λ ; the other measures the M_0 of global blood.

M_0 can be estimated along with T_1 using multiple T_1 -weighted independent measurements. If scan time is limited, the first excitation that is used to establish the steady state can also be used to calculate M_0 . Here, we list three blood M_0 estimation methods used in this situation [21].

Global M_0 from CSF

$$M_0 = R M_{CSF} e^{(TE/T_{2CSF}^* - TE/T_{2b}^*)} \quad (1.34)$$

where R is 0.87 [22]. M_{CSF} is the average value of the top 20% of pixels in the CSF region. T_{2CSF}^* is the T_2^* of CSF, 74.9 ms. T_{2b}^* is the T_2^* of blood, 43.6 ms. One drawback of this method is that there could be a problem with the accuracy of the T_2^* values, which may be different from scanner to scanner.

Global M_0 from white Matter

This method is similar to the CSF method, but uses the signal in white matter. Replace T_2^* of CSF by the white matter T_{2w}^* , which is about 44.7 ms and R is 1.19.

Local M_0 by local λ

This is similar to the method of local tissue M_0/λ , but instead of a global λ , some

researchers use more accurate values of λ for each region. In gray matter, $\lambda = 0.98$, and in white matter, $\lambda = 0.84$.

1.4.4 Arterial Input Function

The AIF function A mentioned in Eq. 1.24 describes the temporal profile of the blood bolus and its dispersion. Most AIF models are based on the convolution of the ideal AIF and a dispersion function [23].

The ideal AIF is described by a boxcar function, without dispersion:

$$a = \begin{cases} 0 & t < \Delta t \\ 1 & \Delta t < t < \Delta t + \tau \\ 0 & t > \tau \end{cases} \quad (1.35)$$

This sharp-edged blood bolus cannot be achieved in practice. Thus, the AIF function is usually convolved with a dispersion function (e.g., log-normal distribution). However, only a few researchers consider the AIF function [24] and most groups use the ideal AIF to simplify the quantification.

1.4.5 ASL Sequence

Current development of ASL mainly focuses on improvement pulse sequences. An ASL sequence can be separated into three parts: tagging pulses, preparing pulses and signal acquisition. There are several excellent reviews about ASL [25–28], so here I only give the basic ideas.

Tagging Pulse

Usually, researchers categorize an ASL method according to its tagging method.

The first ASL experiment followed flow-driven inversion theory and is known as continuous ASL (CASL)[29–31]. CASL tags arterial blood in a proximal slice for a long time (1-2 s), waits for the signal of blood to accumulate in tissue and then images the tissue. This method requires extra coil hardware for tagging, which limits its range of application.

In the 1990s and early 2000s, variants of blood tagging methods were developed with a short RF, which is feasible on commercial scanners, known as pulsed ASL (PASL). PASL methods include PICORE [32], TILT [33] and FAIR [34]. These methods tag a large region in a short time, then wait for the blood in this region to flow into the imaging slice. They have lower specific absorption rate (SAR) values, yield robust results and have been included in commercial protocols. However, the distal blood signal decays before it flows into the imaging slice and this results in lower SNR. The length of the blood bolus is uncertain, which reduces the accuracy in CBF quantification. Velocity selective ASL [35] provides robust quantification, but it uses the saturation of blood instead of inversion labeled blood. Currently, PASL has advantages in dynamic ASL imaging and complex blood flow regions, such as myocardial [36] and lung [37] perfusion imaging.

In 2005, a new breakthrough was achieved in ASL tagging and was named pseudo continuous ASL or pulsed continuous ASL (pCASL) [38–40]. pCASL is similar to CASL, but uses the body RF coil for tagging. It uses a series of short duration RF pulses separated by short time intervals to approach the flow driven inversion condition, which inverts the spins of blood in the feeding artery and builds up a blood bolus. Relatively high SNR and clean

background signal are its benefits. Further improvement has been achieved by including multiple labeling phases [41].

Starting in 2010, territorial ASL [42] became popular, which can tag a selected artery and show the blood supply of a specific brain region. However, only a few large arteries can be selected separately (e.g. left and right internal carotid arteries, left and right vertebral arteries), so it cannot reveal more detailed information about blood supplied by smaller arteries.

Preparing Pulses

ASL images the blood flow delivered to local tissue. The blood signal in large vessels can introduce quantitative error. Researchers use flow suppression method to eliminate this signal. For example, motion sensitive gradients [20, 43] can be used. Another way to suppress flow is to saturate the blood signal before it comes into the image slices, using methods such as QUIPSS [44] and Q2TIPS [45].

ASL has low SNR and is vulnerable to motion artifacts [25]. To stabilize the image and suppress unknown artifacts, background suppression [46, 47] is used to null the signal from static tissue. But this technique also attenuates the ASL signal [48].

Acquisition

ASL is time-consuming, because the tagged blood requires about 1-2 seconds to transit to the image region and more than 10 averages are conventionally performed to improve the image quality. ASL is also motion sensitive. Therefore, a fast acquisition in a single shot is preferable. Echo planar image (EPI) and spiral scanning are widely used in 2D

ASL. Similarly, GRASE and stack-of-spirals perform well in 3D acquisitions [49]. Parallel imaging techniques (e.g. GRAPPA) are used to accelerate acquisition and achieve single-shot imaging. Other fast acquisition methods, such as SSFP [37], has also been described in the literature. SSFP is of particular interest in applications with large susceptibility variations that require short readouts, such as lung perfusion.

In summary, the state-of-art of ASL includes: about 1.8 second pCASL tagging pulse, about 1.5 second post label delay, background suppression pulses, flow suppression pulses and 3D readout. Most ASL sequences achieve resolution from $5\text{ mm} \times 5\text{ mm} \times 5\text{ mm}$ up to $3\text{ mm} \times 3\text{ mm} \times 4\text{ mm}$, with whole brain coverage.

1.4.6 Problems in ASL

The low SNR of ASL requires a large number of signal averages (typically more than 10), which makes imaging time-consuming. To achieve stable images and sufficient SNR, currently ASL is limited to low spatial resolution and single post label delay (PLD) imaging, instead of dynamic imaging.

The ASL signal decays with T_1 when the tagged blood travels from the tagging plane into the imaging slice. This arterial transit time is subject dependent and its variance can lead to inaccuracy in perfusion estimation. One commonly adopted strategy in minimizing the uncertainty of ATT is to use a long PLD, which ensures that all blood bolus reaches the tissue, but this requires prior knowledge of ATT. An over-long PLD may miss peak perfusion and reduce SNR. Velocity selective labeling minimizes ATT uncertainty by selecting blood flowing with a certain velocity, but this reduces labeling efficiency and SNR.

The acquisition of ASL at a single delay time is insufficient to fully characterize cerebral

perfusion in stroke and brain tumor patients clinically. Moreover, the CBF values computed using a single delay time can be inaccurate if the bolus is delayed in a particular region of the brain, which often occurs in patients with cerebrovascular conditions. Dynamic ASL is an emerging alternative that collects a series of perfusion images and can yield more accurate CBF maps and maps of other parameters required for patient management, such as ATT. However, collecting this information robustly with high image quality in three dimensions in a clinically feasible scan time is an extremely challenging technical problem.

Researchers have become interested in dynamic ASL, a strategy that acquires images at multiple PLD times for accurate CBF estimation [50] and potential ATT map formation. Different strategies can be pursued to resolve the dilemma between scan time and multiple PLD frames. The temporal fast data sampling Look-Locker method acquires a series of images with different PLDs in one preparation [51]. Novel ASL Hadamard encoding tagging [52, 53] combines different PLD preparations to improve signal. However, all of the above techniques focus on improving the image for each PLD frame separately using pulse sequence design. This dissertation also explores using advanced image reconstruction methods to improve dynamic ASL.

1.5 Dissertation Overview

The remainder of this dissertation is organized as follows:

Parameter mapping is essential for quantification of ASL perfusion. Furthermore, quantification of parameter maps is increasingly providing widely accepted and important information in clinical diagnosis. In Chapter 2, we propose a method for accurate and accelerated

parameter estimation. We designed a highly accelerated and direct parametric map estimation method using the unscented Kalman filter and extended the proposed method with parallel reconstruction and two-parameter estimation. To evaluate the performance of the proposed method, we compared this novel method to the compressed sensing method with k-p sparsity on phantom and volunteer data. Furthermore, we adapted the undersampling scheme into the acquisition pulse sequence and verified it in an accelerated acquisition.

We developed a robust and fast 3D pCASL sequence with parallel and compressed sensing image reconstruction. In Chapter 3, 3D turbo spin echo with a stack-of-spirals k-space trajectory was designed to compensate for the low speed and low SNR of ASL. A pseudo continuous labeling scheme improved the perfusion signal. To reduce susceptibility artifacts, maintain moderate resolution and be insensitive to motion, including rigid bulk motion and pulsatile blood flow, we developed parallel image reconstruction with a dual-density spiral trajectory. Further, compressed sensing was used to suppress noise and improve image quality.

Dynamic ASL requires multiple measurements with different observation times, which enables the estimation of ATT and an accurate CBF. We exploited the similar spatial structure among frames and prior information about signal evolution to improve image quality and CBF estimation accuracy. In Chapter 4, we developed a compressed sensing reconstruction with sparsity based on a perfusion model and dictionary learning. We then validated the proposed method in simulation, experiments and through evaluation by a neuroradiologist.

Multiple observation times (OT) ASL provides accurate CBF maps by fitting to a dynamic perfusion model. The variance of CBF can be further reduced by optimal OT design. This could significantly improve CBF accuracy in the low SNR situation of ASL. In Chapter

5, we improve CBF estimation in dynamic ASL by designing optimal observation times based on Gaussian and Rician noise, which reduces the variance of CBF estimation. Further, an unbiased maximum likelihood estimator was designed with a Rician noise model. Then, the new designs were validated in simulation and a volunteer scan.

Accelerated T_2 mapping

2.1 Introduction

Tissue parameter mapping shows substantial promise for improved disease characterization. For example, T_1 and T_2 changes have shown high correlation with tumor [54, 55], stroke [56], cardiac lesions [57] and Parkinson disease [58]. Furthermore, the accuracy of T_1 and T_2 maps limit the quantification of other MR techniques, such as cerebral blood flow estimation in arterial spin labeling.

To achieve accurate parameter mapping and multiple component analysis [59], several measurements are usually required along the parameter encoding direction (p-space). A classic example is imaging at multiple TEs for T_2 mapping. Nevertheless, long acquisition times have slowed the adoption of parameter mapping, because they make the parameter map vulnerable to motion and limit the coverage in certain applications (e.g., cardiac T_1 mapping). Therefore, an accelerated parameter mapping paradigm is desirable.

Parameter maps can be accelerated using parallel imaging. In addition, sparsity between k-space and p-space has been exploited by compressed sensing methods for higher acceler-

ation rates. One of the successful constraints for compressed sensing acceleration is model based sparsity. It assumes the image structures are similar at each TE measurement and signals from different pixels follow a similar evolution pattern in p-space. Model-based compressed sensing [60, 61] could include a nonlinear T_2 decay model as a data fidelity term and pursue the parameter map in the reconstruction directly, but this approach is computationally complex. In recent work, the T_2 model has been linearized using principal component analysis [62] and an over-complete dictionary in the K-SVD method [63]. These methods use compressed sensing to reconstruct images, which is then followed by parameter estimation. Moreover, in most compressed sensing reconstructions, the quality and accuracy of the T_2 map depends on the sparse representation and the regularization parameters.

T_2 mapping can be generalized as an estimation problem. In MRI, we do not directly measure the T_2 map, but rather signals that are nonlinear functions of local T_2 . In other words, we observe the dynamic process of the T_2 map at multiple encoding states in p-space. The Kalman filter has been widely used for state tracking and parameter estimation. Recently, Sümbül [64] and Feng [65] successfully adopted it in dynamic MRI by exploiting spatial and temporal redundancy. By viewing the parameter of interest as the state of a dynamic system, we can model the multi-TE measurement process and use the Kalman filter to recursively improve our estimate of a T_2 map.

In this chapter, we seek to explore a new paradigm for parameter mapping, which combines image reconstruction and optimal parameter estimation. A model based unscented Kalman filter (UKF) [66] was applied to accelerate T_2 mapping and combined with parallel imaging. The proposed method was compared with a compressed sensing reconstruction on a numerical phantom and retrospective volunteer data. Then, the accelerated sequence was

developed for prospective acceleration. To our knowledge, this is the first work of parameter mapping in MRI using the unscented Kalman filter.

2.2 Theory

The key to this method is that we track the T_2 map in k-p-space by the UKF directly. The conventional method reconstructs the T_2 weighted images from k-space data and regresses the T_2 map pixel by pixel in image space (Fig. 2.1a). In the proposed method, T_2 weighted images at multiple TEs are not reconstructed, but are modeled as a part of the measurement function (Fig. 2.1b) in k-p-space.

2.2.1 Kalman Filter

The Kalman filter [67] is a recursive and efficient method to estimate the state of a system from noisy measurements. Generally, the Kalman filter describes a dynamic system by two steps: state transition and measurement. The general Kalman filter is given by the following equations:

$$\begin{aligned}
 x_k &= f(x_{k-1}, w_{k-1}) \\
 z_k &= h(x_k, v_k) \\
 p(w) &\sim N(0, Q) \\
 p(v) &\sim N(0, R)
 \end{aligned}
 \tag{2.1}$$

where f is the state transition function; x_k is the k^{th} state of system; w is the system noise, assumed to be white Gaussian noise with covariance matrix Q ; h is the measurement function of state x_k ; z_k is the measured data; and v is the measurement noise, also assumed to be

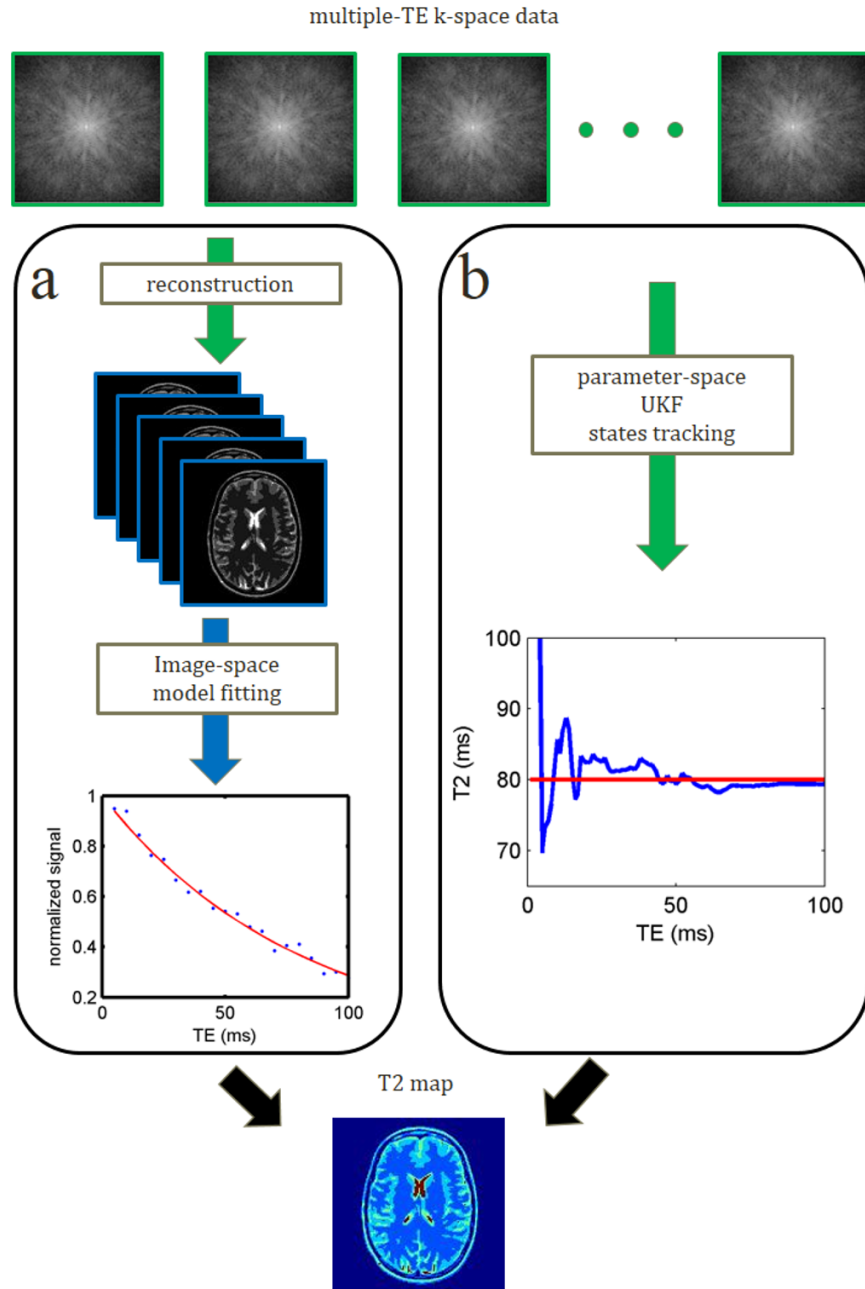


Figure 2.1: T_2 mapping paradigms. With multiple-TE measurements, a T_2 map is commonly processed as shown in (a). k-space data are reconstructed to T_2 -weighted images. The intensity of each pixel (blue dots) is regressed to the signal decay model (red line) and results in the local T_2 value. The proposed method (b) tracks the T_2 value in parameter-space using the UKF, which produces the T_2 map from the k-space data directly. The red line indicates the true T_2 value. The blue line illustrates the tracking process, which approaches the true T_2 value as more measurements are included.

white Gaussian noise with covariance matrix R .

2.2.2 T_2 Signal Model

In the special case of T_2 mapping, we observe the signal decay at a rate of T_2 in p-space. Here we set the T_2 map as the system state, which is assumed to be constant in time and invulnerable to noise. Therefore, the state transition function is given by

$$f(x_{k-1}, w) = x_{k-1} \quad (2.2)$$

Each k-space data sample z_k is one measurement of state x_k with encoding position t_k . The measurement function $h(t_k)$ is composed of signal decay, Fourier transform and measurement noise:

$$h(x_k, v) = U_k F M(t_k) + v \quad (2.3)$$

where F is the Fourier transform and U_k is an undersampling pattern at state t_k that results in a k-p space undersampling scheme. $M(t_k)$ is a T_2 -weighted image at echo time t_k .

The T_2 weighting process is represented using a single-compartment exponential T_2 model

$$M(t_k) = \rho e^{-\frac{t_k}{T_2}} \quad (2.4)$$

where t_k is the echo time.

With constant echo spacing, the model can be simplified as

$$\begin{aligned} M(k) &= \rho \exp(-kx_k), k = 0, 1, 2, \dots, K \\ x_k &= \frac{\Delta t}{T_2} \end{aligned} \tag{2.5}$$

Here, we treat the shortest TE measurement as $\rho \exp(-\Delta t/T_2)$. When the shortest TE equates to the echo spacing, Δt , ρ equals to a proton density image. When the shortest TE is longer than Δt , ρ is a T_2 weighted image, one step backward. k is the index of parameter encoding states.

Given the state transition function f and measurement function h , the Kalman filter estimation problem is now defined. The system state x_k — the desired T_2 map — can be estimated by the UKF, as described in the following section.

2.2.3 Unscented Kalman Filter

The basic Kalman filter uses linear state transition and measurement functions. It can be adapted to nonlinear models using various approximations. An early version of this approach was the extended Kalman filter (EKF), which linearizes the filter using a Jacobian matrix. The EKF has limited accuracy for highly nonlinear problems. The unscented Kalman filter represents the nonlinear model by the unscented transform, follows the state distribution using a deterministic sampling approach and achieves higher order approximation of the measurement.

When we estimate the state x_k from the former state x_{k-1} and measured data z_k , $2N+1$ sigma vectors $\chi_{k-1,i}$ are used to approximate the state transition and the signal measurement.

N is the length of the vector x .

$$\chi_{k-1,i} = \begin{cases} x_{k-1} & \text{if } i = 0 \\ x_{k-1} + T_i & \text{if } i = 1, \dots, N \\ x_{k-1} - T_i & \text{if } i = N + 1, \dots, 2N \end{cases} \quad (2.6)$$

where T_i is the i th column of matrix square root of $(N + \lambda)P_{k-1}$.

$$TT' = (N + \lambda)P_{k-1} \quad (2.7)$$

α and κ describe the distance between the sigma vector and x_{k-1} :

$$\lambda = \alpha^2(N + \kappa) - N \quad (2.8)$$

The sigma states are transformed by the function f , which for this problem propagates the prior state unchanged:

$$\chi_{k,i} = \chi_{k-1,i} \quad (2.9)$$

The estimated state x_k^- is represented by the current sigma vectors:

$$x_k^- = \sum_{i=0}^{2N} w_i^m \chi_{k,i} \quad (2.10)$$

where

$$\begin{aligned} w_0^m &= \frac{\lambda}{\lambda + N} \\ w_{i \neq 0}^m &= \frac{0.5}{\lambda + N} \end{aligned} \quad (2.11)$$

The covariance of x_k^- is approximated by:

$$P_k^- = \sum_{i=0}^{2N} w_i^c (\chi_{k,i} - x_k^-) (\chi_{k,i} - x_k^-)' + Q \quad (2.12)$$

where

$$\begin{aligned} w_0^c &= \frac{\lambda}{\lambda + N} + 1 + \alpha^2 + \beta \\ w_{i \neq 0}^c &= \frac{0.5}{\lambda + N} \end{aligned} \quad (2.13)$$

$\beta = 2$ is optimal for a Gaussian distribution of x [68]. The measured data are approximated by the measurement function h :

$$\begin{aligned} \zeta_i &= U_k F \rho \exp(-k \chi_{k,i}) \\ z_k^- &= \sum_{i=0}^{2N} w_i^m \zeta_i \end{aligned} \quad (2.14)$$

The posterior covariance of measurement z_k is:

$$P_z = \sum_{i=0}^{2N} w_i^c (\zeta_{k,i} - z_k^-) (\zeta_{k,i} - z_k^-)' + R \quad (2.15)$$

The next step is to update the gain matrix:

$$P_{xz} = \sum_{i=0}^{2N} w_i^c (\chi_{k,i} - x_k^-) (\zeta_{k,i} - z_k^-)' \quad (2.16)$$

$$G = P_{xz} P_z^{-1}$$

The final step of the iteration is to correct the state estimate and the covariance matrix:

$$\begin{aligned} x_k &= x_k^- + G(z_k - z_k^-) \\ P_k &= P_k^- - GP_z G' \end{aligned} \tag{2.17}$$

2.2.4 Multiple-Channel Data

Parallel image reconstruction uses multiple-channel data to accelerate scans and improve image quality. Here we will exploit the redundancy among multiple channel data following the SENSE method [69].

To generalize the UKF for multiple-channel data, we add an n -channel sensitivity map S_i to the measurement function h :

$$h(x_k, v) = U_k F \begin{bmatrix} S_1 \\ S_2 \\ \vdots \\ S_n \end{bmatrix} \rho \exp(-kx_k) + \begin{bmatrix} v_1 \\ v_2 \\ \vdots \\ v_n \end{bmatrix} \tag{2.18}$$

To simplify the calculation, we assume that the noise from different channels follows the same distribution R .

2.2.5 Two-Parameter Estimation

We will refer to the above method as the single UKF, because it estimates a T_2 map based on prior knowledge of ρ . A pre-scan to obtain a ρ map is feasible, but this requires additional scan time and could introduce more measurement error. We can incorporate ρ into the

estimated state, which will double the number of variables to be estimated and increase computational complexity. We will call this the two-parameter UKF model. In the two-parameter UKF model, Eq. 2.2 becomes:

$$f \left(\begin{bmatrix} x_{k-1} \\ \rho_{k-1} \end{bmatrix}, \begin{bmatrix} w_x \\ w_\rho \end{bmatrix} \right) = \begin{bmatrix} x_{k-1} \\ \rho_{k-1} \end{bmatrix} \quad (2.19)$$

As for the single UKF, we assume the minimum TE map ρ is constant in time and invulnerable to noise.

2.2.6 Parameter Initialization

To reduce the matrix size in the calculations, we first localize the image pixels using a 1D Fourier transform along the readout direction, as in Feng et. al (12). The minimum TE weighted ρ map is prior knowledge in the single UKF and is initialized using data from shortest TE acquired in the two-parameter UKF. The T_2 map is typically initialized to a constant value. If the initial guess of T_2 is 80 ms, the T_2 map can be written as $x_0 = \Delta t / 80$. The initial estimation error covariance matrix P_0 is empirically chosen as a diagonal matrix proportional to the noise level σ^2 of the measured image.

The distribution of noise v is assumed to be a stationary process, which does not change during the scan. Its covariance matrix R becomes a diagonal matrix with each diagonal element equal to $\sigma^2 I$ in the case of white Gaussian noise. This assumption is more reliable for T_2 measurements of the brain than of the heart, because there is less motion and volume change. There should be no change between each state T_2 , which results in $Q = 0$ in theory. However, we empirically choose a small Q to stabilize the estimation. Tuning the parameters

Q and R can influence the performance of the UKF.

2.3 Methods

2.3.1 Simulation

A realistic analytical phantom [70] was used to simulate the T_2 mapping acquisition, reconstruction and parameter estimation process. We represented the grey and white matter by four ROIs with $T_2 = 50, 80, 120$, and 250 ms. To simulate multiple TEs, 100 parameter encoding states were measured with echo spacing equal to 3 ms. These images were sampled by a Cartesian trajectory with a matrix size of 128×128 .

To evaluate the tolerance of the proposed method, we validated T_2 maps according to noise level and number of available encoding states. The single-parameter UKF was tested on the fully sampled data. In the noise tolerance test, the generated data was contaminated by Gaussian complex noise with SNR from 10 to 100 according to the shortest TE measurement [63]. In the test of number of available measurements, the T_2 maps were estimated with the number of available measurement states from 10 to 100 at SNR 50.

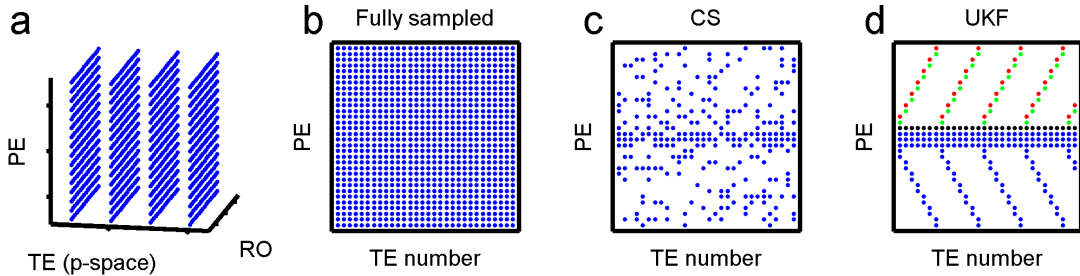


Figure 2.2: T_2 data sampling scheme in k-p-space. (a) and (b) fully sampled data in k-space and p-space (data are always fully sampled in the RO direction). (c) is the incoherent random sampling pattern for compressed sensing with acceleration ratio 4. At each TE encoding state, PE lines are acquired according to the polynomial probability function. (d) is alternative undersampling pattern for the UKF with acceleration factor of 4.

To verify the performance of UKF methods with an accelerated acquisition, we retrospectively undersampled k-space by factors of 2, 4, 6, and 8 at each TE. As shown in Fig. 2.2d, the undersampling pattern included a few fully-sampled central phase-encoding lines and undersampled outer k-space lines at each TE. This pattern is designed to contain the same number of phase encoding lines at each TE measurement, so that it was compatible with a multiple contrast spin echo pulse sequence. The proposed methods were compared to the model-based compressed sensing method with over-complete dictionary trained by K-SVD [63]. To achieve incoherence in the compressed sensing reconstruction, k-space was undersampled following a polynomial distribution in the phase encoding direction (Fig. 2.2c). An over-complete dictionary was trained based on the T_2 decay model. The training data included T_2 values over the range of 1-300 ms, and 100 prototypes were obtained from 1000 synthetic T_2 decay signals. The T_2 decay signal was represented by at most three prototypes. Wavelet thresholding was performed on each frame and the termination tolerance was $\epsilon < e^{-3}$. K-SVD and spatial wavelet sparsity were performed on the real and imaginary parts separately at each pixel. The T_2 map was calculated to minimize the least squared error pixel by pixel across the reconstructed images.

The results were compared with the fully sampled noiseless T_2 map and quantified by structure similarity index (SSIM) [71] and normalized root mean squared error (NRMSE).

2.3.2 Experiments

T_2 mapping data with multiple TE encoding were acquired on healthy volunteers. All the experiments were performed on a 3T Siemens Trio scanner (Erlangen, Germany) with a 12-channel receiver array head coil. The study followed an IRB protocol approved by our

institution with written informed consent from volunteers.

A spin echo sequence was used for validation scans of an ex-vivo brain. The parameters were as follows: matrix size 128×128 , FOV $180 \text{ mm} \times 180 \text{ mm}$, TR 500 ms and slice thickness 4 mm. TE varied from 14 ms to 144 ms with a step size of 2 ms.

A modified multiple contrast spin echo sequence was used to scan normal volunteers. The same phase encoding lines were acquired in one echo train at different TEs. The parameters were as follows: TR 2.5 s, slice thickness 5 mm, FOV $220 \text{ mm} \times 220 \text{ mm}$ and matrix size 192×192 . 70 spin echoes were acquired with echo spacing of 5.5 ms. The total scan time was about 8 minutes.

The volunteer data was retrospectively undersampled by factors of 2, 4, 6 and 8 with the same undersampling scheme used for the simulation. Without prior knowledge of proton density, the two-parameter UKF method and the compressed sensing method with K-SVD were used to reconstruct the T_2 map. The results were evaluated using SSIM and NRMSE by comparison to the standard T_2 map, which was obtained from fully sampled data and least squared error model fitting.

To accelerate the acquisition in practice, we adapted the undersampling scheme into a multiple contrast spin echo sequence. After excitation, the sequence collected 70 spin echoes with echo spacing 5 ms, with each echo designed to acquire a phase encoding value according to the undersampling scheme. For example, the first echo train collected the highest line in each k-space cluster, shown as the red dots in Fig. 2.2d. T_2 maps were estimated by the proposed methods with undersampling factors of 4 and 8. Other scan parameters were as follows: TR 2 s, slice thickness 5 mm, FOV $200 \text{ mm} \times 200 \text{ mm}$ and image matrix size 128×128 . For fully sampled k-space, the scan time would have been approximately 4 minutes.

With the accelerated sequence, the scan times were reduced to approximately 1 minute and 30 seconds for undersampling factors of 4 and 8, respectively.

This reconstruction was carried out in MATLAB 2012b (The MathWorks, Inc) with a 4x GTX 680 Workstation (Amax Information Technologies, Inc). 12 CPU cores (Intel Xeon E5-2640 2.50 GHz Processor LGA2011) were used for parallel computation.

2.4 Results

2.4.1 Simulations

The accuracy of T_2 estimation highly depends on the quality of images and the SNR of the acquired signal. Different SNR level signals were used to test the performance of the model-based UKF. Compared with the noiseless T_2 map, the results in left plot of Fig. 2.3 show that the estimated T_2 map has reduced error and increased similarity as the SNR of the acquisition increases. The amount of available data is also essential to the quality of estimation. As shown in right plot of Fig. 2.3, as the number of TE measurements increases, estimation errors are reduced and similarity index is increased. However, acquiring more than 60 TE measurements yields limited improvement in T_2 map quality.

Figure 2.4 shows the T_2 map estimated of a numerical phantom with an undersampling factor of 8 and $\text{SNR} = 50$. There were negligible undersampling artifacts with any of the reconstruction methods. The compressed sensing method ($\text{NRMSE} = 0.1125$) resulted in lower SNR ($\text{SNR} = 10.4$) and missed some fine structures, as shown in the middle row of Fig. 2.4. Absolute error relative to a fully-sampled noiseless T_2 map for each method is shown in the bottom row. As expected, the single-parameter UKF filter provided most accurate

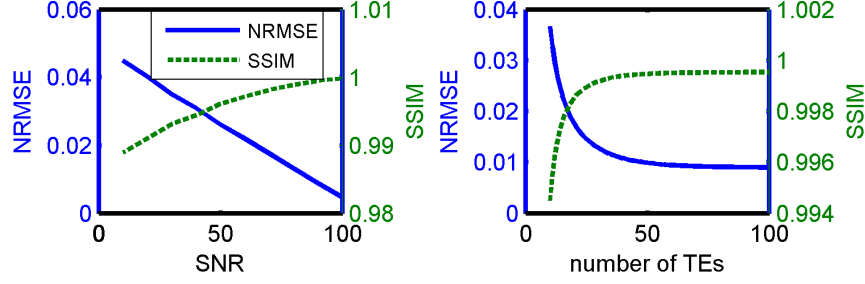


Figure 2.3: UKF performance with SNR level and number of encoding states. With high SNR data, the UKF method results in improved similarity and less estimation error (left). The UKF can improve T_2 map estimation by introducing more measurements, but limited improvement is achieved beyond 60 measurements.

estimation (NRMSE = 0.0272, SNR = 40.4); it benefited from prior knowledge of proton density. Compared with the compressed sensing method, two-parameter UKF reduced the estimation error by a factor of 2 (NRMSE = 0.0507, SNR = 26.6).

Figure 2.5 plots the quantitative results of the compressed sensing reconstruction and proposed UKF methods at different acceleration factors. The single-parameter UKF benefited from prior knowledge of proton density map, resulting in lower estimated errors, higher structure similarity and SNR. Two-parameter UKF estimated both the T_2 map and proton density map, but still resulted in more accurate estimates than the compressed sensing method.

2.4.2 Experiments

Ex-vivo brain scans are shown in Fig. 2.6. The scans were acquired with a standard spin echo pulse sequence to directly show the performance of the parameter map estimation methods independent of pulse sequence factors, such as RF inhomogeneity and eddy currents. With undersampling factors up to 8, both the compressed sensing and UKF methods resulted in negligible undersampling artifacts. Compared with the fully-acquired data set, the proposed

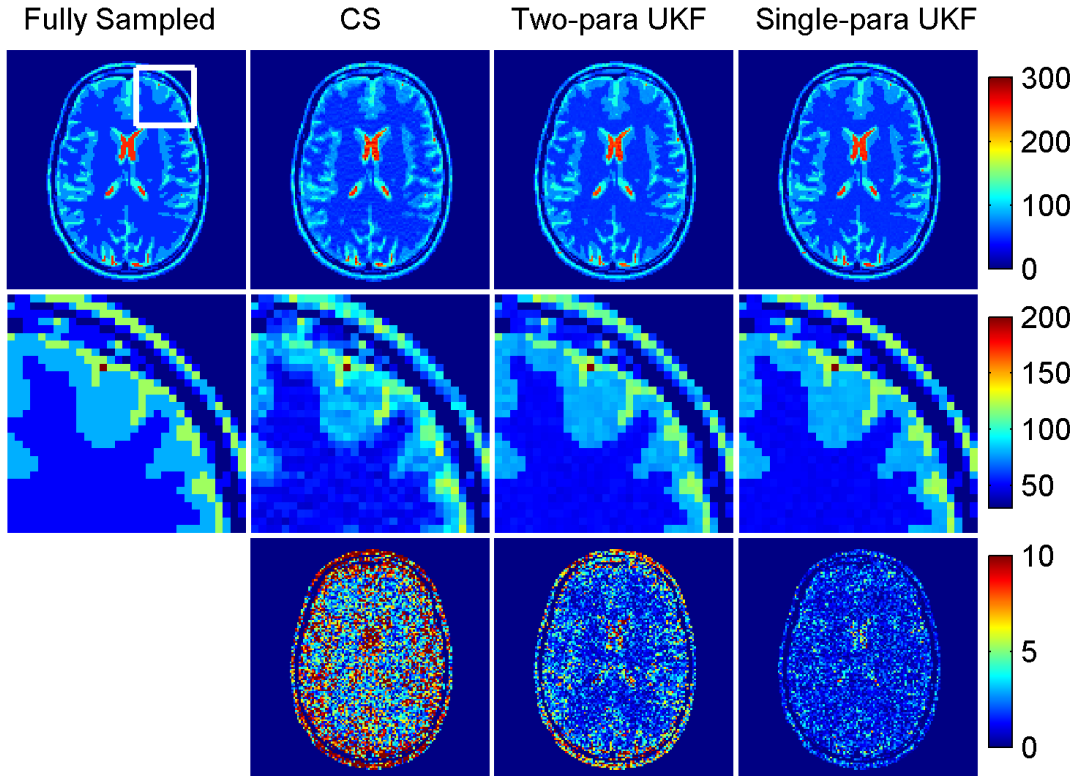


Figure 2.4: T_2 map estimation on the numerical phantom with compressed sensing, two-parameter UKF and single-parameter UKF. With an acceleration rate of 8, the resulting T_2 maps (top) had negligible artifacts. Zoomed-in images (middle row) showed that the UKF methods maintained the fine structures better than the compressed sensing method. The absolute error maps (bottom row) show that the UKF methods had lower estimation error. Maps are shown in ms.

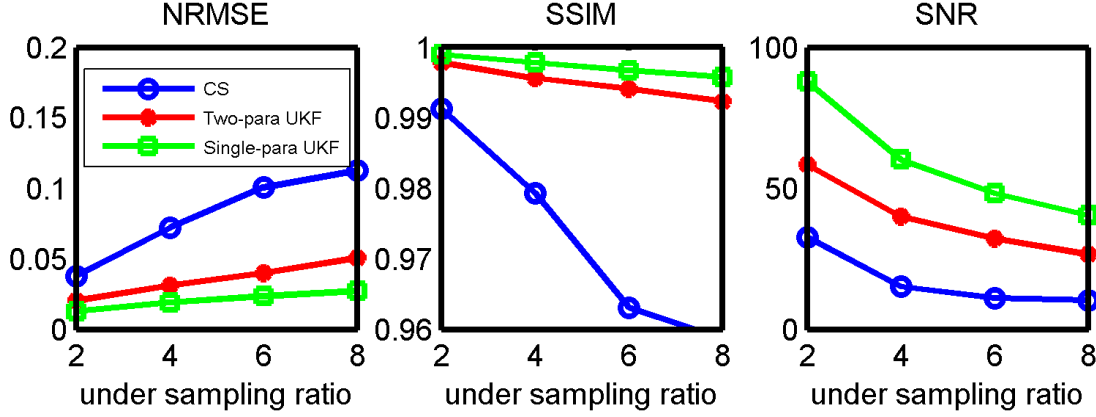


Figure 2.5: Quantification of estimated T_2 map error in the simulation. With acceleration rates of 2, 4, 6 and 8, single UKF estimation results in lowest NRMSE (left), highest similarity index (middle) and highest local SNR (right). Even without prior knowledge of proton density, the two-parameter UKF method still improves accuracy compared to the compressed sensing method.

method yielded lower absolute error than the compressed sensing reconstruction.

The T_2 maps from undersampled data set were quantified by comparing to the fully sampled data, as shown in Fig. 2.7. The proposed method yielded more accurate T_2 maps, with less estimation error and higher structural similarity index. This result held for undersampling factors of 2, 4, 6 and 8.

Volunteer results with retrospective undersampling are shown in 2.8. As in the simulation results, the two-parameter UKF estimated the T_2 map accurately, based on comparison with fully sampled data. At this high acceleration factor of 8, T_2 maps from both methods revealed lower SNR and more error at the interfaces between cerebrospinal fluid and gray matter. The compressed sensing method (NRMSE = 0.0744) began to show undersampling artifacts, as shown in the zoomed-in images along the the middle row, but the two-parameter UKF method maintained negligible artifacts and reduced the estimation error by a factor of 1.6 (NRMSE = 0.0452).

Quantifications of the above results are shown in Fig. 2.9. As the acceleration rate in-

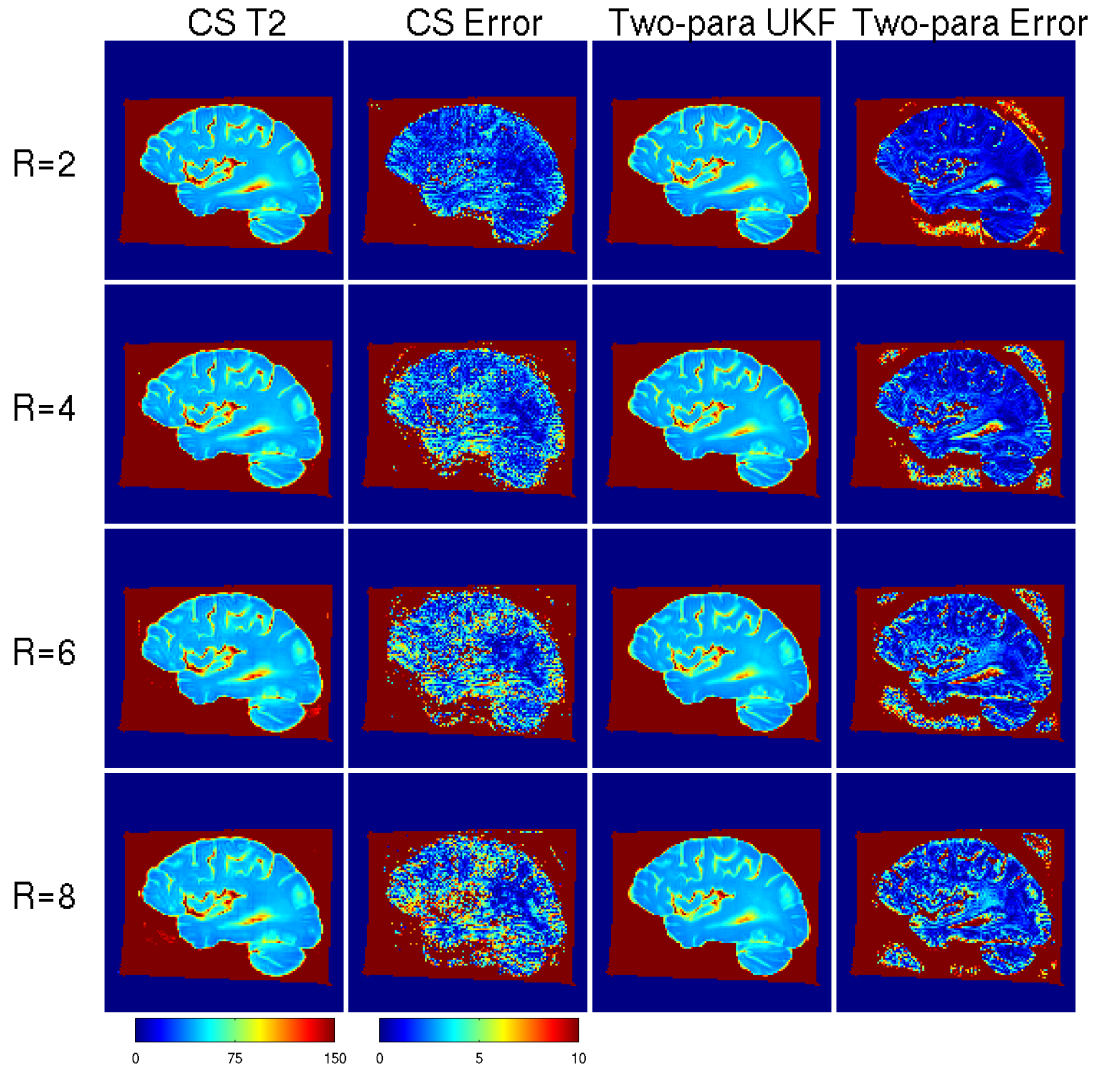


Figure 2.6: T_2 maps from the compressed sensing and UKF methods with an ex-vivo brain phantom. Fully sampled k-space data were retrospectively undersampled by factors of 2, 4, 6 and 8. Both compressed sensing and the two-parameter UKF methods resulted in T_2 maps without notable undersampling artifacts. As shown in the absolute error maps, the two-parameter UKF resulted in lower error than the compressed sensing method, as compared with the fully sampled data set. Maps are shown in ms.

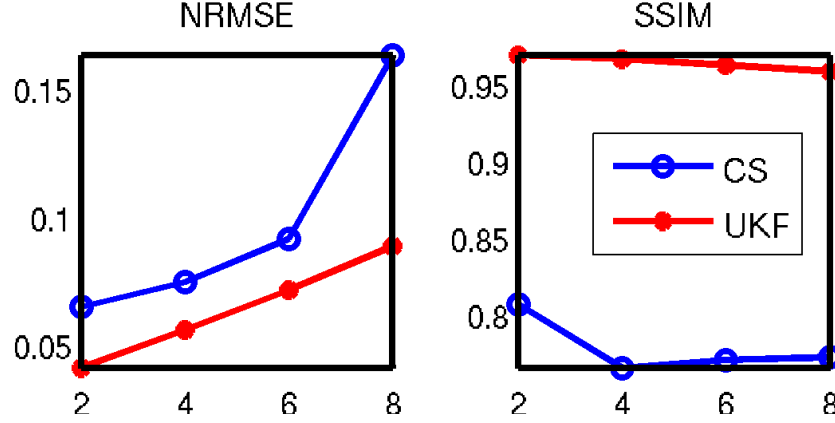


Figure 2.7: Quantification of the T_2 maps from compressed sensing method and the two-parameter UKF method. Undersampled by factors of 2, 4, 6 and 8, the two-parameter UKF method resulted in more accurate T_2 estimation with less RMSE and higher SSIM than the compressed sensing method.

creased, estimation errors increased and structure similarity reduced. The two-parameter UKF method resulted in lower NRMSE and higher SSIM for each retrospectively undersampled case.

Fig. 2.10 shows the T_2 map from accelerated acquisitions with the undersampled sequence. The two-parameter UKF method recovered T_2 maps with undersampling rates of 4 (Fig. 2.10, middle) and 8 (Fig. 2.10, right). Compared to the T_2 map from fully sampled k-p space (Fig. 2.10, left), the proposed method has lower SNR as expected, but few aliasing artifacts and negligible difference overall.

2.5 Discussion

In this chapter, we have developed an unscented Kalman filter model, which provided a novel diagram describing parameter mapping as a state tracking problem in k-p-space. The proposed method uses MR parameters as the fundamental state space and the MR signal model as the dynamic system model. By monitoring the propagation of this dynamic system,

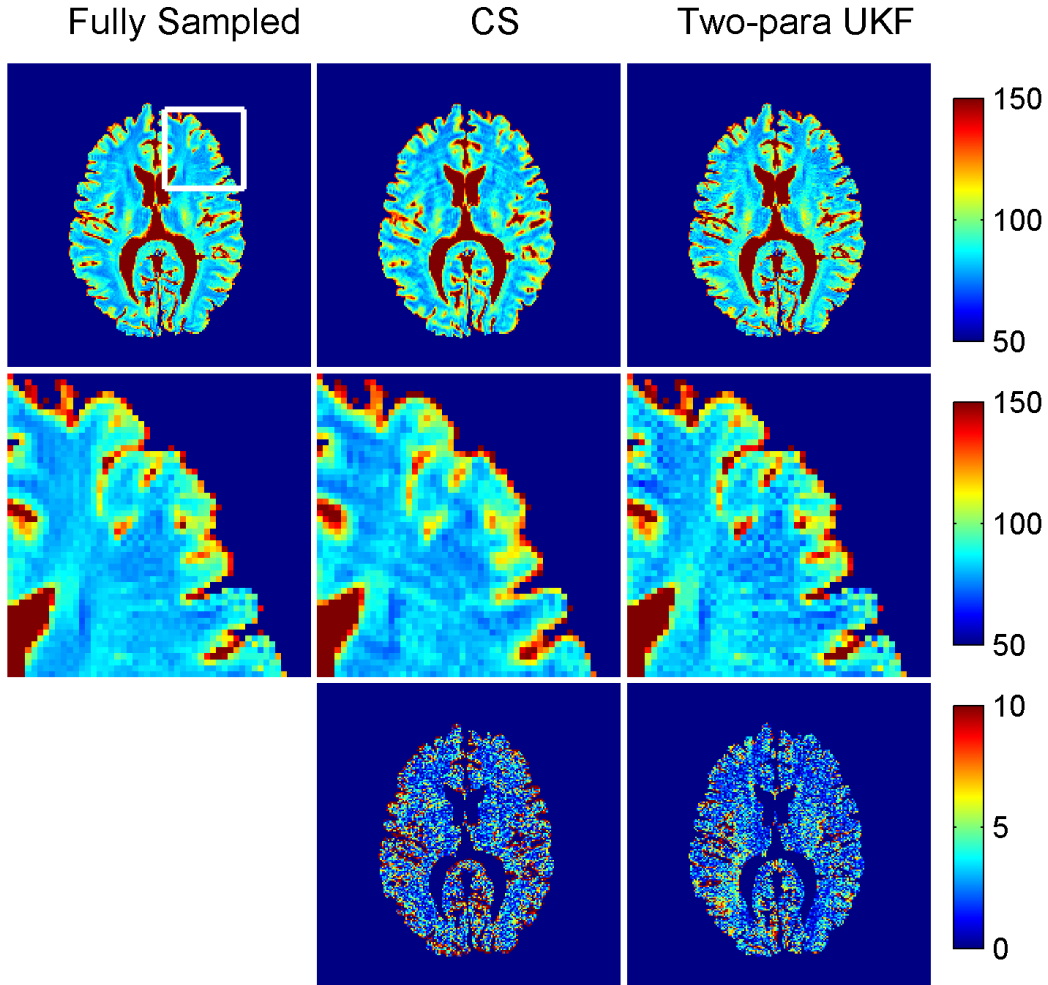


Figure 2.8: T_2 maps from the compressed sensing method and the two-parameter UKF method from a volunteer scan. With a retrospective undersampling factor of 8, the compressed sensing method showed some undersampling artifacts (middle row). By comparison, the two-parameter UKF method maintained the fine structures and only resulted in lower SNR, as expected. Absolute error maps were calculated by comparison with fully sampled data (bottom row). Maps are shown in ms.

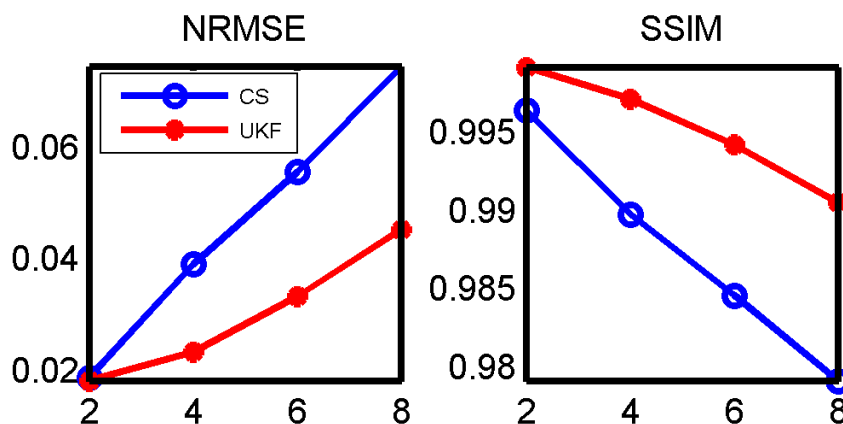


Figure 2.9: Estimation errors on retrospectively undersampled volunteer data. The two-parameter UKF method resulted in more accurate estimation with less NRMSE (left) and higher SSIM (right).

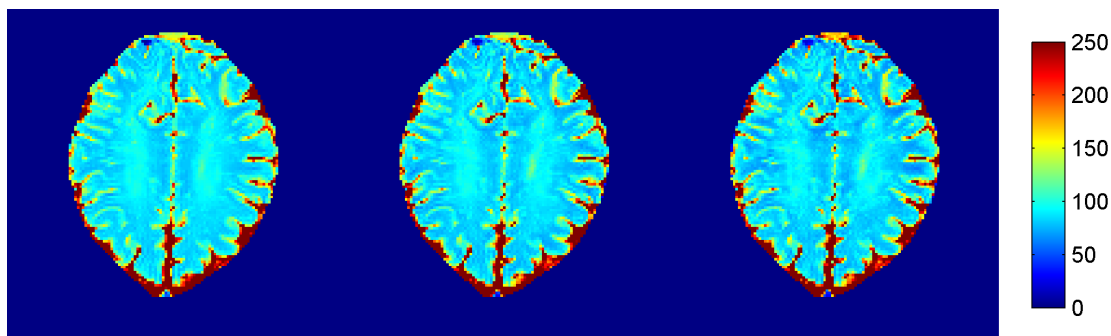


Figure 2.10: The performance of two-parameter UKF method with accelerated acquisition. Compared with the T_2 map from fully sampled k-space data (left), the two-parameter UKF method provided T_2 maps with negligible differences at acceleration rate 4 (middle) and acceleration rate 8 (right). Maps are shown in ms.

it provides quantitative parameter maps directly without image reconstruction.

This method was specialized to the problem of T_2 mapping from highly undersampled k-space data. This method combines image reconstruction and parameter estimation into a UKF measurement model. It achieves high accuracy in parameter estimation with under sampling factors of 2, 4, 6 and 8, which is comparable to compressed sensing methods.

The proposed method was derived for T_2 estimation, but the unscented Kalman filter method can be easily adapted into other parameter measurements, such as T_1 mapping with a Look-Locker pulse sequence. Since the Fourier transform operator is linear, the non-linearity of the signal model limits the performance of the UKF estimator. The proposed method can be used to estimate multiple parameters by adopting a new signal model in Eq. 2.4. However, a complex model could reduce the accuracy of estimation and require more measurements.

The proposed method was tested for T_2 mapping, focusing on grey matter and white matter on 3T, so we limited the T_2 values in simulation from 50 to 250 ms and the initial T_2 was set around 80 ms for gray matter. A wider T_2 range could be included to include cerebrospinal fluid and other long T_2 species, which would mean that the proposed method would be used to track a wider parameter range. The performance of the method under these conditions would need to be evaluated.

The accuracy of parameter estimation is limited by the number of measured states in p-space. The Kalman filter achieves maximum likelihood estimation, which approaches the minimum variance estimator when number of encoding states is large enough. More measurements along p-space increase the estimation accuracy. However, the length of the echo train in a multiple contrast spin echo sequence is also limited by the readout bandwidth

and SNR. The measurements with long TE have low SNR and yield limited improvement to the estimate. The number of measurements in p-space is also limited by the specific application. In T_2 mapping, it costs little time to measure more states in the same echo train, but this method can cost extra time in some applications (e.g., conventional diffusion-weighted imaging).

An alternative way to improve the estimation accuracy is to improve the convergence of the UKF estimator. The first few iterations of a Kalman filter can be seen as the training the covariance P . A small initial P_0 can stabilize the propagation of the covariance matrix P and also constrains the range of estimated values to be near the initial value. More accurate initialization of T_2 and proton density maps could help with convergence, but this will slow down the training of covariance matrix.

The direct estimation of the T_2 map contains only a real value, which is different from complex image estimation. Here, we simply assume the phase of image comes from coil sensitivity. In a single coil measurement, the proposed method performs better with a sensitivity map, which provides the phase information for data fidelity. When using multiple channel data, the UKF method adopts the features of parallel imaging reconstruction, which helps to improve the estimation parameter map quality. The SENSE scheme is a theoretical extension of UKF methods. But the accuracy of sensitivity maps will directly affect the estimation of T_2 map. It should be possible to add sensitivity estimation to the UKF model, which would enable simultaneous estimation of a sensitivity map and a T_2 map. However, this would also significantly increase the estimation complexity.

The accuracy of the estimated T_2 map also depends on pulse sequence design. The multiple contrast spin echo sequence is time efficient compared to a conventional spin echo

sequence, but the signal is not accurately modeled by a mono-exponential T_2 decay model. It includes multiple signal pathways, is limited by the accuracy of the refocusing RF pulses, and contains diffusion attenuation from crusher gradients. Additionally, in fully sampled k-p-space, the same phase encoding lines are acquired in one excitation, but in undersampled k-p-space some of the phase encoding lines are acquired in different echo trains. The order of phase encoding lines could introduce more variation in the quantification of the T_2 map. In this work, our main focus was on the design of the parameter tracking algorithm; additional improvements are possible with better sequence design.

The 1D simplification achieved by performing a 1D Fourier transform along the read-out direction before the UKF reduces the error covariance matrix P size and makes the calculation memory efficient. However, it also reduces the correlation information between different phase encoding lines, and thus does not capitalize on some potential improvements in estimation accuracy.

The proposed method computes T_2 maps directly, without reconstructing T_2 -weighted images. For applications that require T_2 -weighted images, a T_2 -weighted image can be generated based on the resulting T_2 and proton density maps.

The performance of compressed sensing highly depends on the undersampling scheme, and this is also true for UKF methods. We used simple undersampling patterns in this work. As shown in Fig. 2.2(c) and (d), the incoherent pattern in compressed sensing reconstruction is distributed polynomially along the phase encoding direction and distributed uniformly in p-space. The UKF undersampling scheme covers k-space at each measured state equally to simplify pulse sequence implementation. Optimal pattern design [72] could improve the performance of both compressed sensing and UKF methods, but it is beyond the scope of

this chapter.

One possible reason for the better performance of the UKF method is that it exploits the signal model more efficiently. Compressed sensing methods assume the image can be represented by a few atoms in a dictionary, including a spatial dictionary (e.g. wavelet transform bases) and a model based dictionary (e.g. K-SVD and PCA). But the signal decay model can be fully described by two parameters. By comparison, the two-parameter UKF method estimates the two parameters in T_2 model directly. This feature could more efficiently exploit the redundant information of the parameter encoding states, can represent the measured signal better and help recover each TE image from undersampled k-space data.

2.6 Conclusion

In this work, we developed a new paradigm of parameter mapping based on the unscented Kalman filter. This method estimates the parameter map of interest directly from k-p-space data and provides accurate estimation of the parameter at high acceleration rates.

Robust ASL with a Single PLD

ASL has low SNR and is sensitive to motion. Therefore, preserving perfusion contrast and suppressing artifacts are necessary for accurate CBF estimation. In this chapter, we will develop a robust ASL pulse sequence and image reconstruction methods to improve image quality. This chapter has three sections. The first section describes an efficient ASL pulse sequence. The ASL signal is generated by pCASL tagging pulses and acquired by using a 3D spin echo train with a stack-of-spirals k-space trajectory for high SNR. The second section describes methods to improve motion robustness. Parallel image reconstruction is used to suppress motion artifacts by efficiently exploiting coil redundancy. Single-shot imaging with a dual-density spiral trajectory is also developed to accelerate ASL imaging. The third section describes techniques for noise suppression. Spatial sparsity constraints are used to improve conventional ASL images. Numerical phantoms and normal volunteers were used for assessing these new methods.

This chapter is focused on static ASL imaging with single post label delay, but it lays the groundwork for the dynamic ASL methods described in Ch. 4 and Ch. 5.

3.1 Introduction

ASL has good repeatability in brain [73] and kidney [74, 75] imaging. ASL has been compared to PET [76] and DSC [7] to confirm that it provides reliable information about pathology. However, the signal from labeled blood produces low signal-noise-ratio ASL images, which typically contain only 1% of the signal of conventional MR images. Therefore, ASL image quality is a key to accurate ASL quantification.

The quality of ASL images can be improved with respect to three components: contrast generation, signal acquisition and image reconstruction. Recently, researchers have made substantial progress in these areas. As a blood tagging method, pseudo continuous ASL (pCASL) has higher SNR than pulsed ASL, because of its high labeling efficiency and long labeled blood bolus. As a signal acquisition method, turbo spin echo with 3D stack-of-spirals [1] can give images comparable to a Cartesian trajectory with a shorter scan time. This method also maintains the motion insensitivity of spiral readouts, which is important for motion-sensitive ASL imaging. A dual density spiral trajectory fully-samples the center of k-space and under-samples the outer region k-space, so that it is possible to achieve single-shot imaging with parallel reconstruction. As an image reconstruction and recovery method, compressed sensing [77] has been successful in accelerating MR imaging and improving image quality. For accurate parameter estimation, we will focus on these three components to improve ASL image quality in this chapter: (a) development of an SNR and time efficient pCASL sequence by using 3D stack of spirals; (b) motion robustness by parallel imaging and spiral trajectory design; and (c) noise suppression by compressed sensing with spatial sparsity.

3.2 Sequence Design

3.2.1 3D Acquisition

Whole-brain coverage can be achieved using multi-slice 2D imaging with echo-planar or spiral readouts. However, 3D echo-train techniques yield higher SNR and sample the perfusion bolus at the same time throughout the brain [78]. Conventional TSE is typically not fast enough, but researchers have successfully used 3D GRASE and 3D TSE with stack-of-spirals for 3D ASL [39].

Spiral trajectories cover k-space rapidly and are robust to motion artifacts [79, 80]. Our lab has developed a 3D spiral TSE pulse sequence [1, 81], where a 3D stack-of-spirals trajectory is traversed by inserting spiral readouts into the refocusing intervals of a TSE pulse sequence. Symmetric phase encoding along the slice direction provides a true 3D image. Each echo train repetitively samples a particular spiral interleaf. Slab excitation and chopping are performed by alternating the phase of the refocusing pulses during signal averaging. Crusher gradients along all three axes are used to eliminate banding artifacts.

This sequence is capable of using various spiral trajectory designs. Flexible on-line spiral gradient design can be used for constant-density or variable-density spiral scanning. Gridding image reconstruction is performed on-line.

An image acquired using the 3D TSE stack-of-spirals pulse sequence is shown in Fig. 3.1. The image shows a resolution phantom scanned in a Siemens 3T Trio scanner. A constant density spiral with 16 interleaves achieved in-plane resolution of 1.5 mm by 1.5 mm. Slab selective RF excited a region of 28 slices with slice thickness 3.5 mm. The result demonstrates



Figure 3.1: Image acquired using a 3D TSE stack-of-spiral acquisition. (a) Coronal view of a phantom. (b) Sagittal view. (c) Transverse view.

good in-plane image quality and a good through-plane slice profile.

3.2.2 Tagging Pulse

Pseudo continuous arterial spin labeling (pCASL) [39] was used to generate the blood bolus. This technique approaches the flow-driven-inversion condition by breaking each long duration RF pulse into a series of small duration RF pulses with a short inter-pulse interval, which is feasible on most commercial scanners. The RF pulse train was built by repeating Hanning pulses of 500 μ s duration with a 500 μ s gap before the next pulse. The mean B1 amplitude was 1.63 μ T and the mean gradient was 0.2 mT/m, corresponding to $\eta_b = 7\%$ [40]. Control and label scans were switched by controlling the phase of RF pulses. The tagging plane was placed 80 mm below the anterior commissure (AC) - posterior commissure (PC) line.

The proposed pulse sequence that combines pCASL tagging with 3D TSE stack of spirals is shown in Fig. 3.2. A 3D ASL image of a normal volunteer acquired with this pulse sequence is shown in Fig. 3.3.

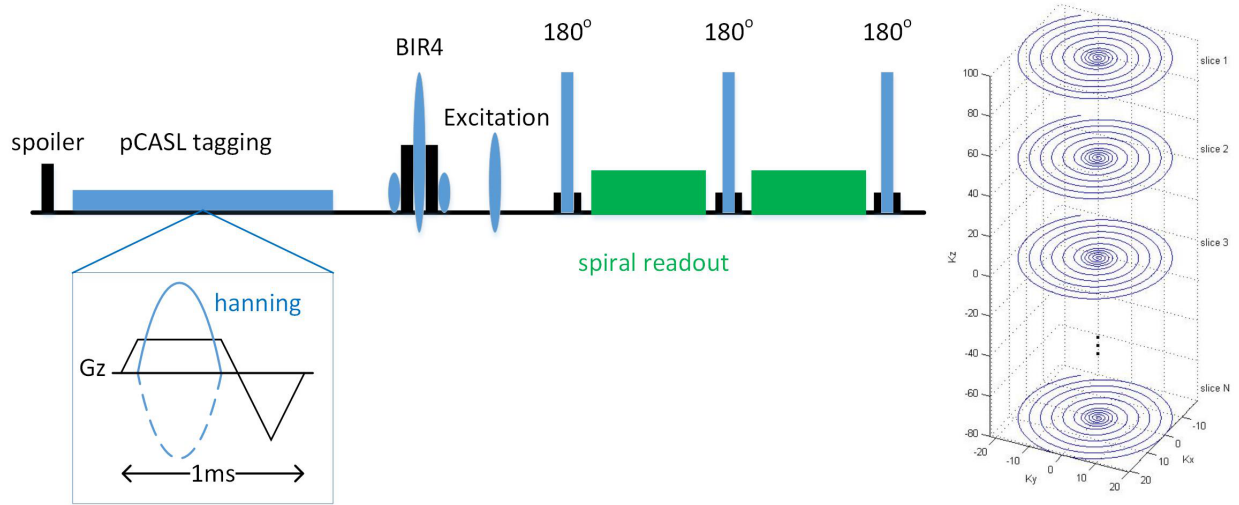


Figure 3.2: The schematic of pCASL with 3D TSE stack of spirals. ASL tagging is achieved by a large number of small flip angle and short (500 us) Hanning RF pulses with the same phase in label images and alternating phase in control images. Vessel blood signal is eliminated by a BIR4 RF pulse module with flow-spoiling gradients. Signal is excited by a slab selective pulse and chopping is performed by alternating the phase of the refocusing pulses during signal averaging. k-space is sampled using a 3D turbo spin echo with spiral readouts and phase encoding along the z direction. Each echo train repetitively samples a particular spiral interleaved as the z phase encoding symmetrically samples kz. Crushers before and after inversion pulses are used to eliminate banding artifacts.

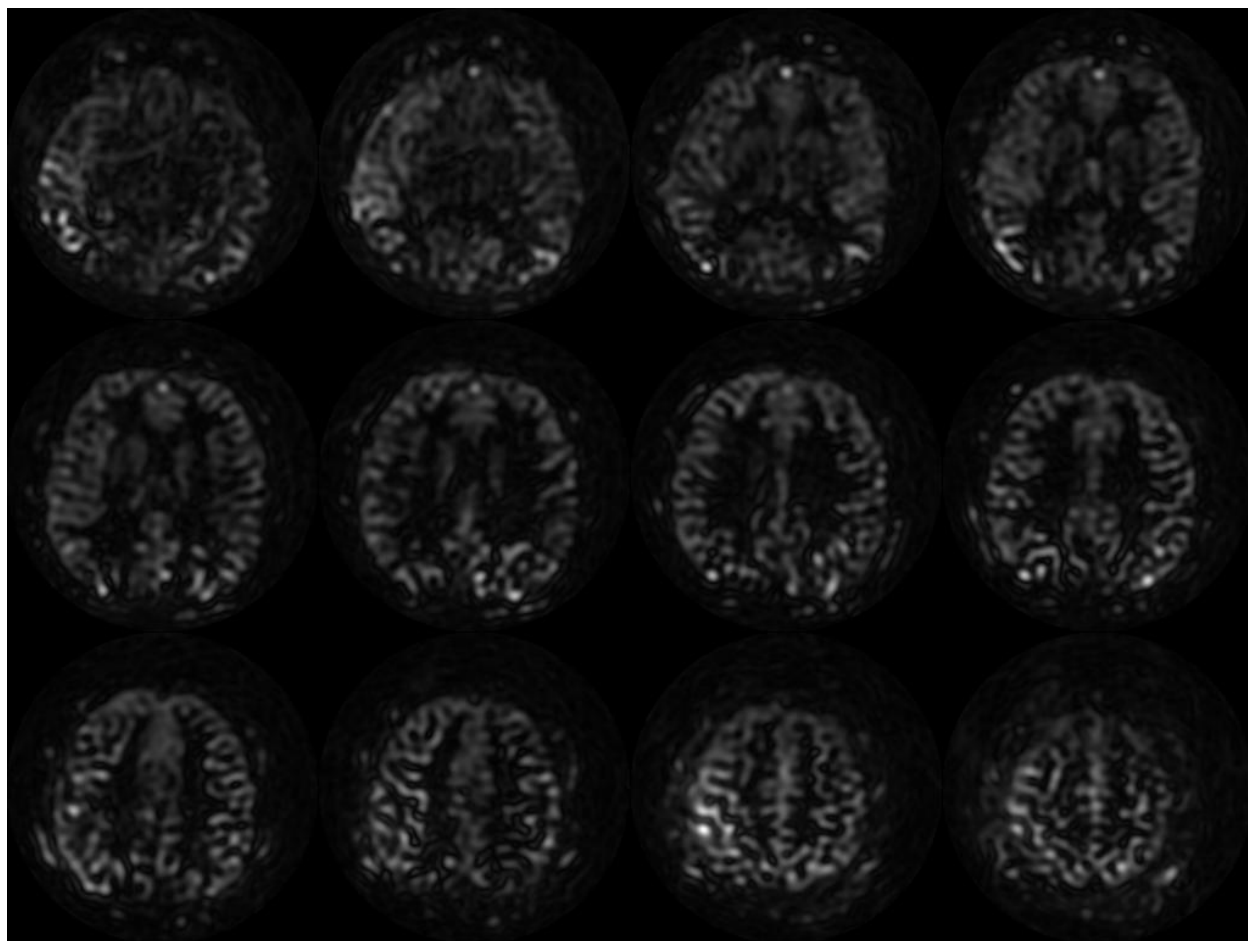


Figure 3.3: 3D pCASL images with TSE spiral sequence. 12 slices with slice thickness 5 mm. Constant density spiral trajectory with 6-ms readouts and three interleaves. Eight averages were used to improve SNR.

3.3 Motion Robustness

3.3.1 Constant-density and Parallel Imaging

A 3D spiral TSE pulse sequence is a rapid and SNR-efficient pulse sequence that can be used for ASL without using accelerated image reconstruction techniques. One option is to cover all of k-space in a single shot and then perform signal averaging to gain SNR and motion robustness. However, the conventional spiral trajectory design yields modest (about 5 mm in-plane) spatial resolution and its long readout becomes sensitive to susceptibility artifacts. An interleaved spiral acquisition yields improved resolution, but is more sensitive to patient and physiological motion (e.g., flow in large vessels).

Single-shot spiral ASL with conventional image reconstruction method yields robustness to motion, but at the cost of low spatial resolution and susceptibility to artifacts. Multi-shot spiral scanning yields better resolution, but more sensitivity to motion artifacts.

One example of spiral ASL motion artifacts are ring artifacts centered on blood vessels. We simulated these artifacts by varying the intensity of the point spread function for each interleaved measurement. The simulation is shown in Fig. 3.4. From this simulation, we can see that data inconsistency across multiple spiral measurements results in a ring-like artifact. Compare this artifact with Fig. 3.5, which shows a ring-like artifact centered on the sagittal sinus, which pulsates with the cardiac cycle. When each interleaved spiral is acquired at different phase of cardiac cycle, the inconsistency will result in a ring-like artifact.

This artifact can be reduced by signal averaging, which also improves SNR. When a long scan time is feasible, more averaging is always preferable in ASL. The artifact can also be

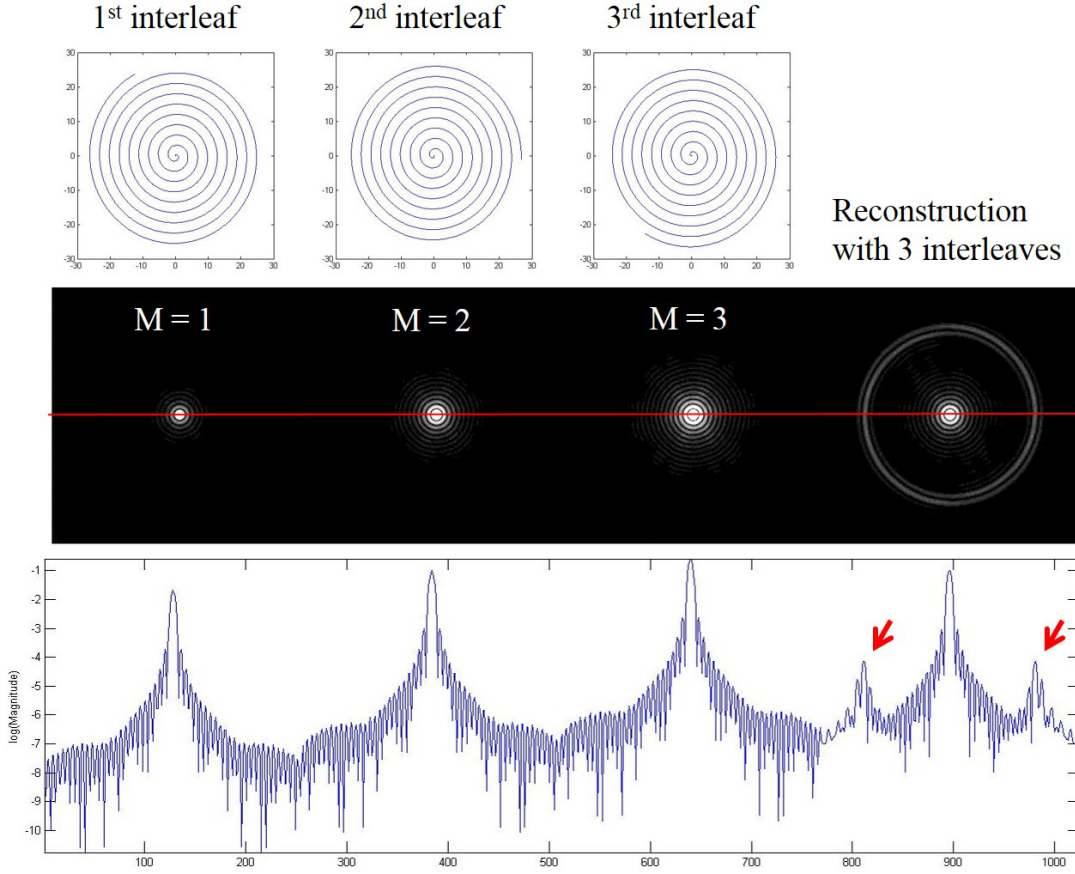


Figure 3.4: Simulation of a spiral point spread function with pulsatile motion. The intensity of large vessels varies according to the cardiac cycle, which introduces data inconsistency in multiple-shot measurements. The target signal is changing (middle) at the sampling time for each interleaf (top). When combining the data from 3 interleaves, the reconstruction results in a ring artifact. The line plot (bottom) shows the aliasing artifact.

reduced by background suppression with additional RF preparation pulses, which is known to suppress motion artifacts and stabilize the resulting ASL subtraction images, although at the cost of a reduction in SNR.

Here, we exploit the redundant information in a multi-coil scan and use the SPIRiT parallel reconstruction method [77] to enforce the consistency of measurements so as to reduce the ring artifact in multi-shot spiral ASL. SPIRiT is a GRAPPA-like parallel imaging reconstruction, which can be adapted to an arbitrary trajectory. This method can be described

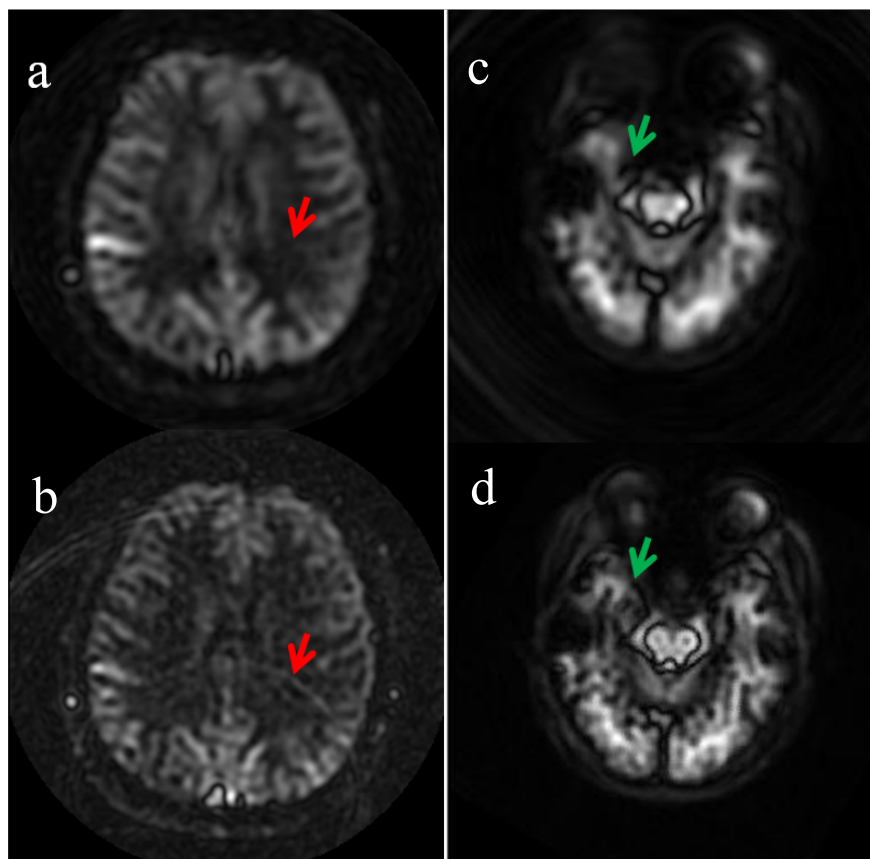


Figure 3.5: Single-shot spiral scanning results in a stable ASL image (a), but relatively low resolution and more susceptibility artifacts in the T_1 weighted images (c). The green arrows highlight the susceptibility artifacts. The multiple-shot spiral scan has better resolution and fewer susceptibility artifacts (b), but it is more sensitive to motion artifacts (d). As the red arrows highlight, the pulsatile motion results in ring-like artifacts.

using the following cost function:

$$\min : \|Fx - y\|_2 + \lambda \|(G - I)x\|_2 \quad (3.1)$$

where x is the target image and y is the acquired data. F is Fourier transform operator, which can be Cartesian or non-Cartesian, and usually includes undersampling. G is a calibration kernel, which is trained by the fully-sampled k-space center and describes the relationship between the acquired and missing data.

Here, SPIRiT reconstruction was performed on each interleaf of the component image separately and then the complex images from each interleaf were added together to form the final component image. The component images were subtracted using either complex or magnitude subtraction to form the perfusion image. For comparison, images were also reconstructed by gridding the data from the interleaves together.

As shown in the Fig. 3.6, gridding yields component images with no visible motion artifacts from either bulk or venous motion. However, the subtraction images show the pulsatile motion artifact, which manifests as a ring artifact in a multi-shot spiral scan. The artifact is significant when using complex subtraction (c), because of phase inconsistency. The artifact is reduced when using magnitude subtraction (d), where negative values are ignored, but some artifact remains (red arrow). The subtraction images are significantly improved by using SPIRiT to reconstruct each interleaf separately. The artifact is largely eliminated when using both complex (e) and magnitude (f) subtraction.

This method was tested on data from four extra volunteers, as shown as Fig. 3.7. The pulsatile motion in the vein resulted in ring-like artifacts with conventional gridding recon-

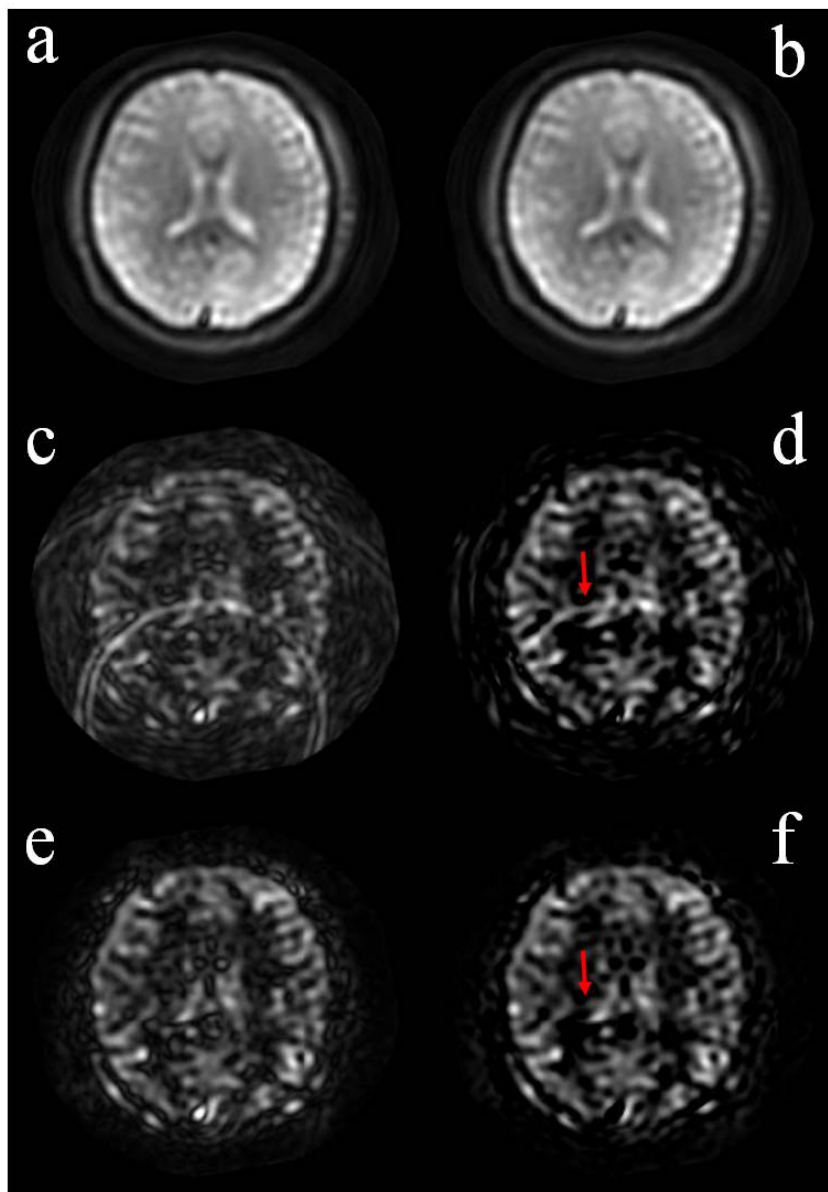


Figure 3.6: SPIRiT correction for ring artifacts. Gridding reconstruction: control image (a), label image (b), complex subtraction (c) and magnitude subtraction (d). SPIRiT reconstruction: complex subtraction (e) and magnitude subtraction (f).

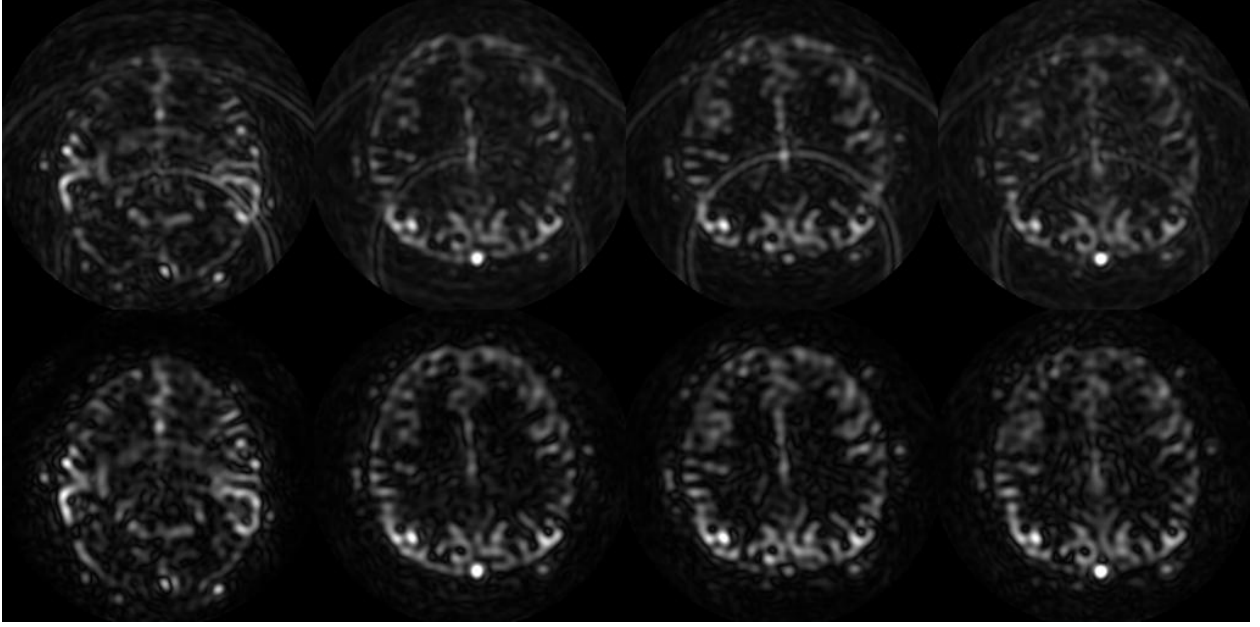


Figure 3.7: Four more volunteer images with pulsatile motion correction. The top row is conventional gridding image reconstruction with complex subtraction. The bottom row shows the corresponding parallel image reconstruction for each subject. The pulsatile motion artifacts is eliminated with parallel image reconstruction.

struction and complex subtraction (top). Using the proposed parallel reconstruction with SPIRiT, the artifact was eliminated.

3.3.2 Single-shot Spiral and Parallel Imaging

Using a parallel image reconstruction permits single-shot scanning at higher spatial resolution. Using the SPIRiT non-Cartesian parallel image reconstruction method [82] and a dual-density spiral acquisition, we demonstrated that parallel spiral acquisition allows single-shot acquisition with improved spatial resolution and good motion robustness.

ASL imaging provides perfusion contrast by subtracting a labeled image group from a control image group. In addition to the low SNR, this subtraction makes ASL more vulnerable to motion artifacts, which includes the rigid bulk motion and the pulsatile motion in large vessels corresponding to cardiac cycle. Motion artifacts can occur with motion

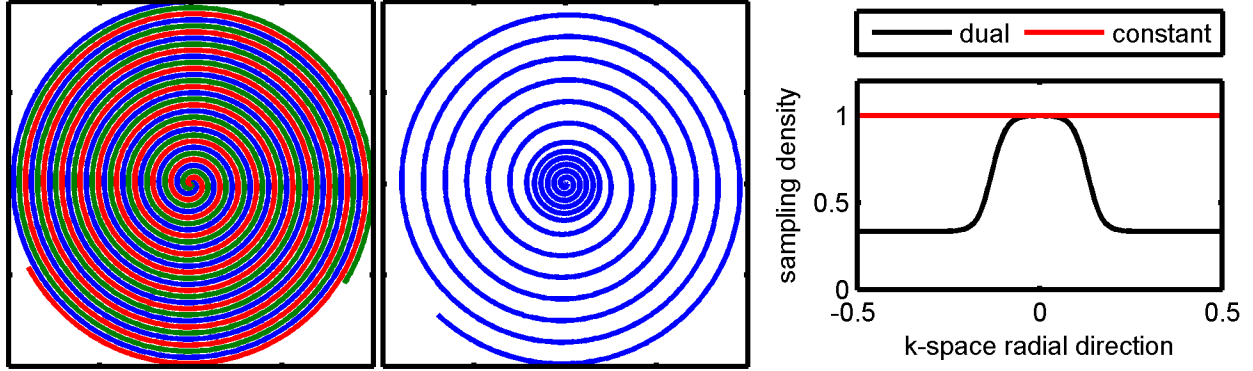


Figure 3.8: Constant-density and dual-density spiral. Left: Constant-density spiral trajectory with three interleaves. Middle: Dual density spiral trajectory with a single interleaf. Right: Sampling density along radial direction of k-space.

between the acquisition of different spiral interleaves, between multiple repetitions, and between the control and label images. Constant density spiral trajectories can cover the k-space with long readouts, but will introduce susceptibility artifacts and T_2/T_2^* shadowing. To cover the k-space fast and efficiently, we use a dual density spiral trajectory. Spiral trajectories are always oversampled in the angular direction. The trajectory is constant density when the sampling density in radial direction follows the Nyquist rule. Dual density spiral scans fully sample the center of k-space, but rapidly reduces to an undersampled density (e.g. 1/3 Nyquist ratio) in the outer k-space, as shown in Fig. 3.8. Here, we control the slope of the transition in density by a Fermi function.

Fig. 3.9 shows an image from a single-shot dual density spiral. This scan was carried out on a healthy volunteer with resolution 4 mm by 4 mm by 4 mm. Measurements were repeated 8 times to improve the SNR. k-space was covered by three dual density spiral trajectories with different initial angles. In the reconstruction, data were processed by a conventional gridding method on each spiral readout separately. The images show good contrast between white and grey matter, and little signal in the CSF region, which does not contain perfusion

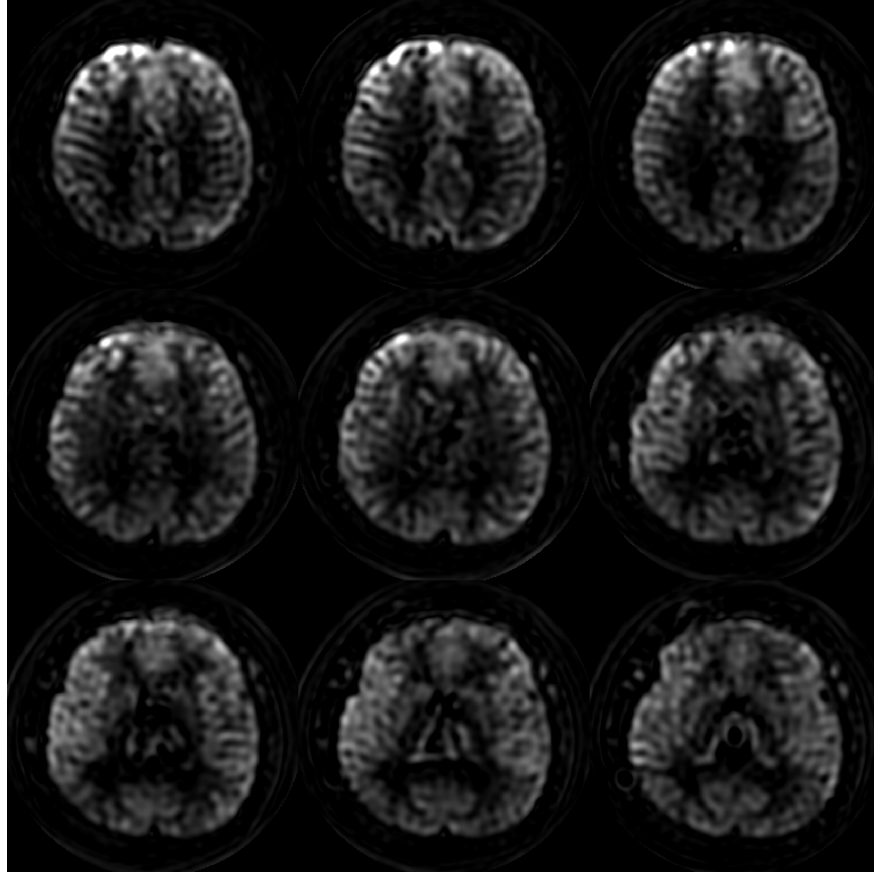


Figure 3.9: ASL images acquired with a 3D single-shot dual-density spiral scan.

signal. Better results can be achieved by parallel reconstruction. In particular, the image can be reconstructed by SPIRiT as mentioned above, but we used the gridding method here to compare the performance of the trajectory only.

With a constant-density spiral trajectory, it is difficult to correct for motion between multiple interleaves. Using single-shot dual-density trajectory and parallel image reconstruction, we can freeze the motion and use conventional registration methods to correct for it. To verify the method, we designed a dual-density spiral with three interleaves. Each interleaf can be reconstructed by the parallel method and three interleaves can be averaged in image domain, which is equivalent to repeating the measurement to improve the SNR. These three interleaves can also be combined to fill an over-sampled k-space, which can be reconstructed

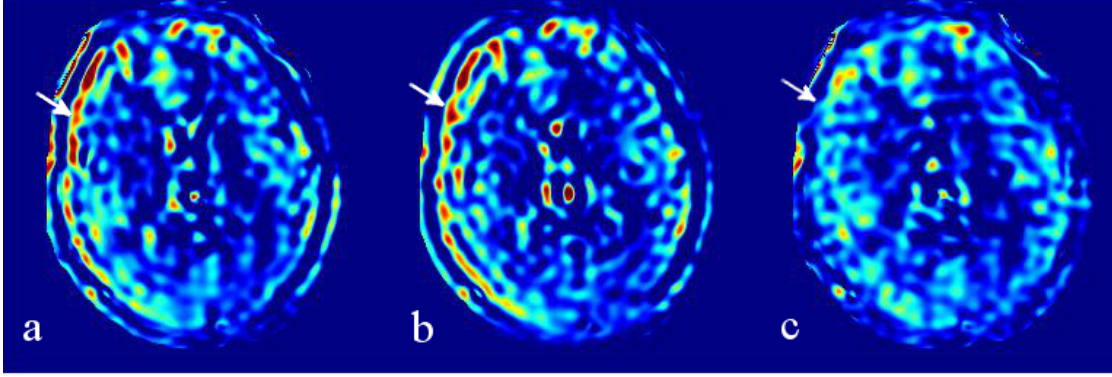


Figure 3.10: Dual density spiral trajectory freezes motion. (a) Conventional gridding reconstruction. (b) Parallel and compressed sensing reconstruction; (c) Compressed sensing reconstruction with image registration.

by a conventional gridding method, as with a constant-density trajectory. Using this design, we can determine the motion artifacts with the same data set. As shown in Fig. 3.10, the motion artifact is apparent as a bright edge in the ASL images (a) when the gridding reconstruction was used. The artifact is not reduced with a parallel and compressed sensing image reconstruction (b). When each interleaved leaf was reconstructed separately and was registered to the image from the first measurement, the motion artifact was reduced significantly.

3.4 Noise Suppression by Spatial Sparsity

Spiral parallel imaging is a very rapid imaging method, but there is an SNR penalty at high acceleration rates. Compressed sensing (CS) is another option for accelerated image reconstruction. It is based on exploiting sparsity of the data in some domain, and grew out of earlier research in nonlinear denoising methods. CS can simultaneously accelerate acquisition and provide denoising, and thus is an intriguing option for ASL image reconstruction. It can be combined with parallel imaging for highly accelerated image acquisition with excellent SNR. Compressed sensing methods based on spatial sparsity have been actively studied in

the past decade and used to reduce MR scan time and improve SNR. Different sparsity transforms were tested on high-resolution pCASL fully sampled data to improve the image quality.

Compressed sensing is a one example of constrained image reconstruction, which can exploit prior knowledge to improve image quality. For example, total variation is based the assumption that medical images are piece-wise smooth. By enforcing this constraint, called a sparse representation in compressed sensing, it is possible to suppress noise like artifacts and recover the image. Compressed sensing can be expressed as follows:

$$\begin{aligned} \min : & |\phi x|_p \\ \text{s.t.} & \|Fx - y\|_2 \end{aligned} \tag{3.2}$$

where x is the target image and y is the acquired data. F is a Fourier transform operator, which can be Cartesian or non-Cartesian, and usually includes undersampling. ϕ is a sparse transform operator on the image and p is the norm of this sparse representation.

The above optimization is solved by a Lagrange multiplier λ :

$$\min : \|Fx - y\|_2 + \lambda |\phi x|_p \tag{3.3}$$

It can also be combined with SPIRiT parallel reconstruction as described above:

$$\min : \|Fx - y\|_2 + \lambda |\phi x|_p + \|(G - I)x\|_2 \tag{3.4}$$

A numerical phantom [70] was used to test the performance of spatial sparsity. A control

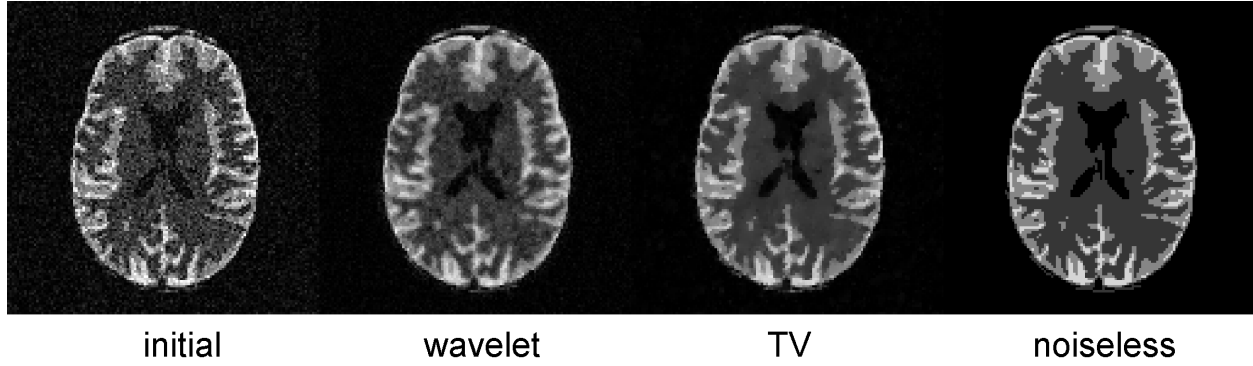


Figure 3.11: Noise suppression by enforcing spatial sparsity on a simulated phantom. Noise in the initial image was largely suppressed when spatial wavelet and TV sparsity were enforced. The compressed sensing method recovered the ASL image and approximated the noiseless image well.

image was generated without perfusion contrast, which corresponds to a proton density image with a long TR and short TE sequence. Therefore, the component images before subtraction will not provide information about structures and contrast for the ASL image. The label image and control image contained about 1% difference for perfusion contrast. Gaussian noise was added with SNR 10 for the ASL images. Control and label images were sampled to Cartesian k-space and separately reconstructed by the compressed sensing method.

Fig. 3.11 shows compressed sensing results enforcing different types of spatial sparsity. The initial noise image ($\text{RMSE} = 11.3\text{e-}4$) was recovered using a wavelet constraint ($\text{RMSE} = 7.4\text{e-}4$) and a total variation (TV) constraint ($\text{RMSE} = 5.9\text{e-}4$). Fig. 3.12 shows the structural similarity index map, where 1 stands for the same structure and 0 stands for not similar. The compressed sensing method improved the similarity in the low SNR white matter region.

One ASL experiment was performed on a 3 Tesla Siemens Trio scanner with a 12-channel receiver coil. There were 7 interleaves covering one slice; each interleaf had 3600 samples and a 7.2-ms readout, resulting in-plane normalized resolution of $2.0 \text{ mm} \times 2.0 \text{ mm}$. The

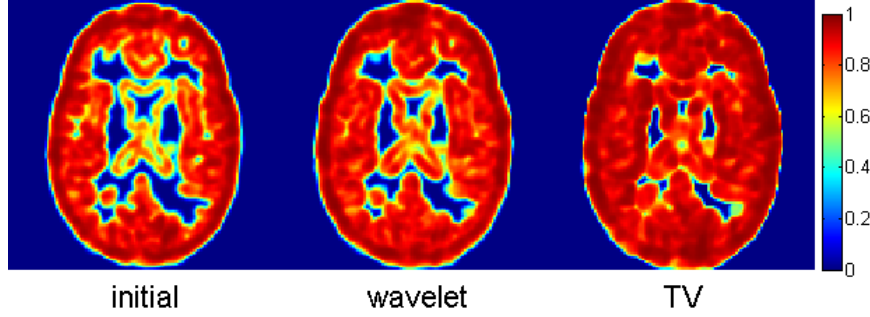


Figure 3.12: Enforcing spatial sparsity improves the structural similarity in a numerical phantom. Wavelet and TV sparsities improve the similarity to a noiseless ASL image. There is no perfusion signal in the CSF region, so the similarity shows limited improvement in this pure noise region.

same interleaved from difference slices were collected as one echo train with symmetric encoding in the z direction. 24 slices with thickness 4 mm were collected to cover the whole brain. Slab excitation and chopping were done by alternating the phase of refocusing RF pulses corresponding to odd and even average number. Crushers in z axis are used to eliminate the banding artifacts. Six averages and 3.5s TR resulted in a total scan time of about 5 min. Slice position was corrected first and a 1D FFT was performed along slice direction, and then the data from 13 slices were reconstructed. This ASL image has higher spatial resolution than common ASL images (e.g. $4.0 \text{ mm} \times 4.0 \text{ mm}$), so it has lower SNR. The compressed sensing reconstruction was performed with total variation and wavelet transform constraints.

The result is shown in Fig. 3.13. SPIRiT reconstruction revealed more fine structures in image, but it also amplified the noise. With the sparsity constraints, the noise in image was suppressed. This is consistent with the simulation results.

To evaluate the methods, pCASL images were acquired as part of dynamic ASL experiments (Chapter: 4). Three interleaved dual-density spiral scans were collected. The labeling

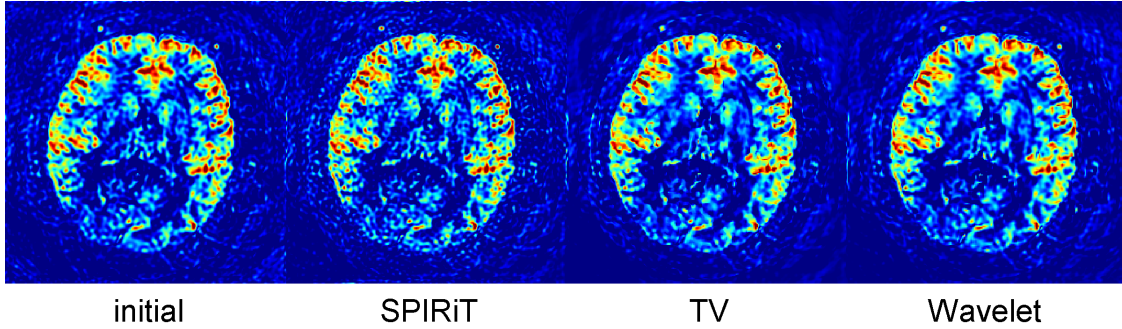


Figure 3.13: The performance of spatial sparsity on a high resolution ASL image. The initial image is noisy with conventional gridding reconstruction. The SPIRiT method revealed more detailed structures, but is also noisy. The compressed sensing method recovered an ASL image by enforcing spatial sparsity constraints. Both spatial sparsity constraints reduced the noise in the image.

duration was 2 s, post label delay was 1100 ms and resolution was $4.0 \text{ mm} \times 4.0 \text{ mm}$. Four averages and three interleaves were acquired. TR was 5 seconds and total scan time was about 2 minutes.

First, these three interleaves oversampled the center of k-space and fully sampled the rest of k-space, and thus they can be reconstructed by the gridding method, as in other published multiple-shot ASL spiral imaging scans. Second, each interleave can be reconstructed as a individual image by constrained reconstruction with spatial sparsity and multi-coil redundancy. Motion compensation (MC) was performed on the constrained reconstruction results before averaging and subtraction.

A neuroradiologist graded the images in a random order. A Likert scale was used with criteria of good quality of clinical diagnosis. 1 stands for strongly disagree; 2 stands for disagree; 3 stands for neither agree nor disagree; 4 stands for agree and 5 stands for strongly agree.

The scores in Table 3.1 show that motion compensation preserves or improves image quality in every volunteer but one (Volunteer 4).

Table 3.1: Neuroradiologist grading results with gridding, CS and CS-MC reconstruction

	Gridding	CS-MC
Volunteer 1	4	4
Volunteer 2	2	3
Volunteer 3	5	5
Volunteer 4	5	4
Volunteer 5	4	5
Volunteer 6	3	3
Volunteer 7	3	4
mean	3.7	4

3.5 Conclusion

In this chapter, we developed a robust ASL sequence with a single-shot 3D stack-of-spirals readout. The ASL image quality can be further improved by motion correction and compressed sensing image reconstruction. This protocol could provide more stable ASL imaging in the brain and provided a foundation for our study of dynamic ASL imaging.

Dynamic ASL

Dynamic ASL measures the perfusion bolus at multiple observation times and yields accurate estimates of CBF in the presence of variations in arterial transit time (ATT). ASL has intrinsically low signal-to-noise ratio (SNR) and is sensitive to motion, so that extensive signal averaging is typically required, leading to long scan times for dynamic ASL. The goal of this chapter was to develop an accelerated dynamic ASL method with improved SNR and robustness to motion using a model-based image reconstruction that exploits the inherent sparsity of dynamic ASL data. Both a sparse signal model and spatial sparsity were enforced in a compressed sensing and parallel image reconstruction of pseudo continuous arterial spin labeling (pCASL) k-space data acquired at nine observation times. Performance of the technique was verified using a numerical phantom. The technique was tested using data acquired from normal volunteers using a single-shot 3D turbo spin echo pulse sequence with a stack-of-spirals readout on a 3-Tesla scanner. The proposed method was compared to gridding and parallel image reconstruction.

4.1 Introduction

Since the blood magnetization is “labeled” upstream of the volume of interest, a portion of the ASL signal decays before arterial blood flows into the imaging slab, and the acquired signal thus depends on the tagged blood arrival time, called the arterial transit time (ATT), which in turn depends on both the blood flow velocity and the delay between labeling and image-data acquisition. Nevertheless, most ASL studies follow the single post label delay (PLD) protocol, which cannot provide a subject-dependent ATT map and may result in errors in CBF quantification [20, 83]. A PLD longer than the ATT can ensure the blood bolus has flowed into surrounding tissue and reduces estimation error [19], but this method may miss the peak ASL signal and requires prior knowledge of the ATT.

A multiple-PLD protocol can fully characterize the ASL dynamic model, improve CBF accuracy and provide rich hemodynamic information, but it is time-consuming. Therefore, researchers have focused on methods for accelerating dynamic ASL. However, accelerating each ASL measurement individually can reduce image quality. Background suppression has been applied to reduce background artifacts and stabilize images [46, 47, 84], but it also attenuates the ASL signal [48].

In this chapter, we propose to accelerate dynamic ASL image acquisition through a combination of three methods. First, we use a rapid and efficient data acquisition method: 3D turbo spin echo (TSE) imaging with a spiral k-space trajectory. (Other readouts can be used, such as 3D GRASE.) Next, we incorporate parallel imaging. Spiral TSE parallel imaging is a very rapid imaging method, enabling single-shot 3D scanning. However, there is an SNR penalty at high acceleration rates. So, we also incorporate compressed sensing [77],

which is based on exploiting sparsity of the data in some domain and grew out of earlier research in nonlinear denoising methods. Compressed sensing can simultaneously accelerate acquisition and provide denoising, and thus is an intriguing option for ASL image reconstruction. Here we combine compressed sensing with parallel imaging for highly accelerated image acquisition with excellent SNR.

The first step in applying compressed sensing to ASL image reconstruction is to apply a spatial sparsity transform; the denoising properties of this approach enable single-shot imaging with improved SNR. This is a promising technique in its own right, but the dynamic ASL problem is even richer with opportunities for compressed sensing. For this problem, we certainly need high acceleration. We also need high SNR, not only for the perfusion images, but also for the resulting parameter maps. The key hypothesis of this chapter is that for dynamic ASL perfusion imaging, the similar spatial structure of images at different delay times and prior information about their temporal evolution can be exploited to improve image quality and perfusion parameter estimation. By using the sparsity of dynamic ASL perfusion images in the domain of a perfusion model, we can efficiently use the relationship between different time frames and not just reconstruct each frame separately. The resulting image reconstruction suppresses both random noise and motion artifacts, because they do not conform to the underlying perfusion model. The proposed method results in rapid and robust dynamic ASL imaging, as demonstrated below.

4.2 Algorithms

In dynamic ASL, perfusion images with the same CBF information are measured at multiple observation times (OTs). These measurements are usually reconstructed separately. But they can be reconstructed more efficiently by combining all dynamic frames with an ASL dynamic model.

4.2.1 Dictionary Representation

Compressed sensing recovers images from noise or noise-like artifacts using a sparsity-promoting image reconstruction. This constrained optimization problem is usually solved by introducing Lagrange multipliers:

$$\hat{x} = \arg \min_x \|Fx - y\|_2 + \lambda \|R(x)\|_p \quad (4.1)$$

where, x is the target image. y is the acquired data. F is a Fourier transform operator that includes the k-space sampling trajectory and under-sampling pattern. $R(x)$ is the representation of x in the sparse transform domain, constrained in the minimization with norm p . λ is a regularization parameter.

Suppose the signal x can be represented by a linear combination of a few elements in the dictionary D , which contains n prototypes, $D = d_1, d_2, \dots, d_n$.

$$x = \sum_{i=1} s_i d_i + \epsilon \quad (4.2)$$

where, ϵ is the tolerant error, which limits the sparsity of the representation. s_i is the

coefficient on prototype d_i and is an element of a sparse coefficient vector $S = s_1, s_2 \dots, s_n$, where most elements are zeros. Compressed sensing improves image quality by enforcing the sparsity of S , while maintaining data fidelity.

$$\hat{x} = \arg \min_x \|Fx - y\|_2 + \lambda \|S\|_p \quad (4.3)$$

Additional sparsity constraints can be used to improve the image quality. The total variation (TV) constraint is commonly used for noise suppression and image recovery. Based on piece-wise smooth assumption, TV suppresses the noise-like variance and maintains the edge structure. With the additional constraint, the target function becomes:

$$\hat{x} = \arg \min_x \|Fx - y\|_2 + \lambda_1 \|x\|_{p1} + \lambda_2 \|TV(x)\|_{p2} \quad (4.4)$$

4.2.2 ASL Model and Over-complete Dictionary

K-SVD [85] is an algorithm to generate an over-complete dictionary D , which contains more prototypes than the dimension of signal x . Compared with an orthogonal dictionary, such as one obtained by principle component analysis (PCA) [62], the over-complete dictionary design achieves a sparser representation of the signal and improves compressed sensing performance on a limited dimension signal, such as dynamic ASL, where only a few number of OT encoding steps are present because of the limited scan time.

The K-SVD algorithm builds up the signal prototype dictionary iteratively from a training data set. Because each tissue pixel will follow a valid ASL signal evolution pattern Fig. 4.1, it can be described by prototypes based on the ASL dynamic model. Therefore, we trained

the K-SVD dictionary with a synthetic dataset generated from an ASL signal model. By using a large number of signal prototypes representing the realistic range of possible ASL parameters, we can represent any expected signal. The K-SVD algorithm then distills the representation down to a smaller dictionary that can still represent any expected signal accurately as a linear combination of a small number of signal prototypes.

The following single-compartment perfusion model [14, 20] was used to generate the training data:

$$\Delta M = 2M_0\alpha f T_1 \exp\left(-\frac{\Delta t}{T_{1,b}}\right) Q(t) \quad (4.5)$$

$$Q(n) = \begin{cases} 0 & \text{if } 0 < t < \Delta t \\ 1 - \exp\left(-\frac{t-\Delta t}{T_1}\right) & \text{if } \Delta t \leq t \leq \Delta t + \tau \\ \exp\left(-\frac{t-\tau-\Delta t}{T_1}\right) - \exp\left(-\frac{t-\Delta t}{T_1}\right) & \text{if } \Delta t + \tau < t \end{cases} \quad (4.6)$$

where, ΔM is the dynamic ASL signal, t is the observation time, Δt is arterial transit time and f is CBF, τ is the blood bolus duration, α is the labeling efficiency. T_1 and $T_{1,b}$ are the longitudinal relaxation times of brain tissue and blood. M_0 is the equilibrium magnetization of blood. Training data were comprised of 9600 ASL dynamic signals, with CBF 1-120 ml/100g/min and ATT 50-4000 ms. Each signal was sampled at 9 observation times (600, 1100, 1600, 2100, 2600, 3100, 3600, 4100, 4600 ms). The K-SVD algorithm generated 256 prototypes.

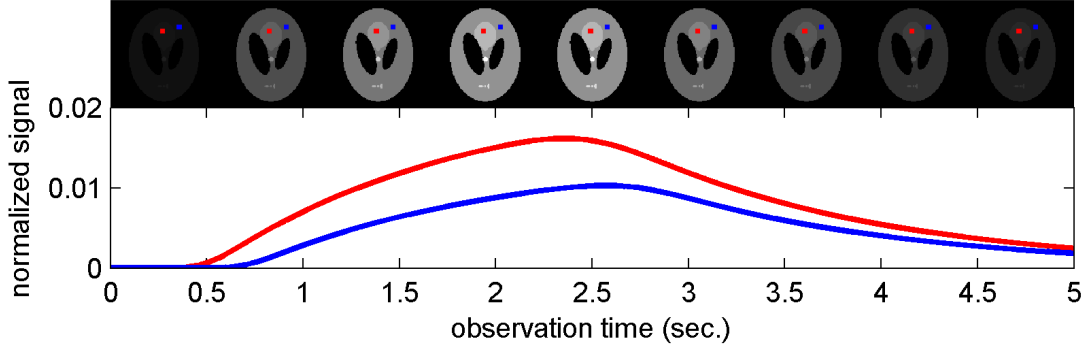


Figure 4.1: Evolution of dynamic ASL signals in a numerical phantom showing the underlying assumptions of this work. The signal from an individual pixel is temporally slowly varying. The dynamic signals in different pixels (blue and red) follow the same nonlinear perfusion model with different parameter values.

4.2.3 Compressed Sensing Solver

This image reconstruction problem is a nonlinear optimization problem. We apply the following four steps to solve this problem, as shown in Fig. 4.2:

- 1, Define x as the ASL perfusion-weighted images. The k-space data is subtracted pair-wise to get the data y with ASL contrast. x_0 is initialized by gridding and zero padding.
- 2, The multi-OT ASL images are projected onto the pre-trained dictionary D pixel by pixel. Orthogonal matching pursuit is used to enforce sparsity in the over-complete dictionary.

$$\begin{aligned}
 & \text{minimize} : \|S\|_0 \\
 & \text{subject to} : \|x - SD\| < \epsilon
 \end{aligned} \tag{4.7}$$

Q represents this model based sparsity in the image space.

$$Q = SD \tag{4.8}$$

3, The TV constraint is enforced by a shrinkage with a penalty method [86].

$$P = \frac{TV(x)}{\sum \|TV(x)\|_2} \max \left(\sum \|TV(x)\|_2 - \frac{\lambda 2}{\beta}, 0 \right) \quad (4.9)$$

4, A least squared function was solved by the conjugate gradient method to maintain the data fidelity and enforce the constraints of model based sparsity Q and total variation P .

$$\hat{x} = \arg \min_x \|Fx - y\|_2 + \lambda 1 \|x - Q\|_2 + \lambda 2 \|TV(x) - P\|_2 \quad (4.10)$$

If in-plane k-space is undersampled for acceleration, we can recover the image by using information from multiple channels. SPIRiT [82] is an autocalibrated parallel reconstruction method that can be used with non-Cartesian trajectories. When using undersampled k-space, we combine the calibration consistency penalty and data fidelity terms:

$$\hat{x} = \arg \min_x \|Fx - y\|_2 + \lambda 1 \|x - Q\|_2 + \lambda 2 \|TV(x) - P\|_2 + \lambda 3 \|(G - I)x\|_2 \quad (4.11)$$

Where, G is the SPIRiT calibration kernel.

Step 2-4 are repeated until the stopping criterion (improvement of cost function is less than 0.01) is satisfied..

4.3 Pulse-sequence Design

4.3.1 Blood Tagging

Pseudo continuous arterial spin labeling (pCASL) [39] was used as described in Ch. 3.

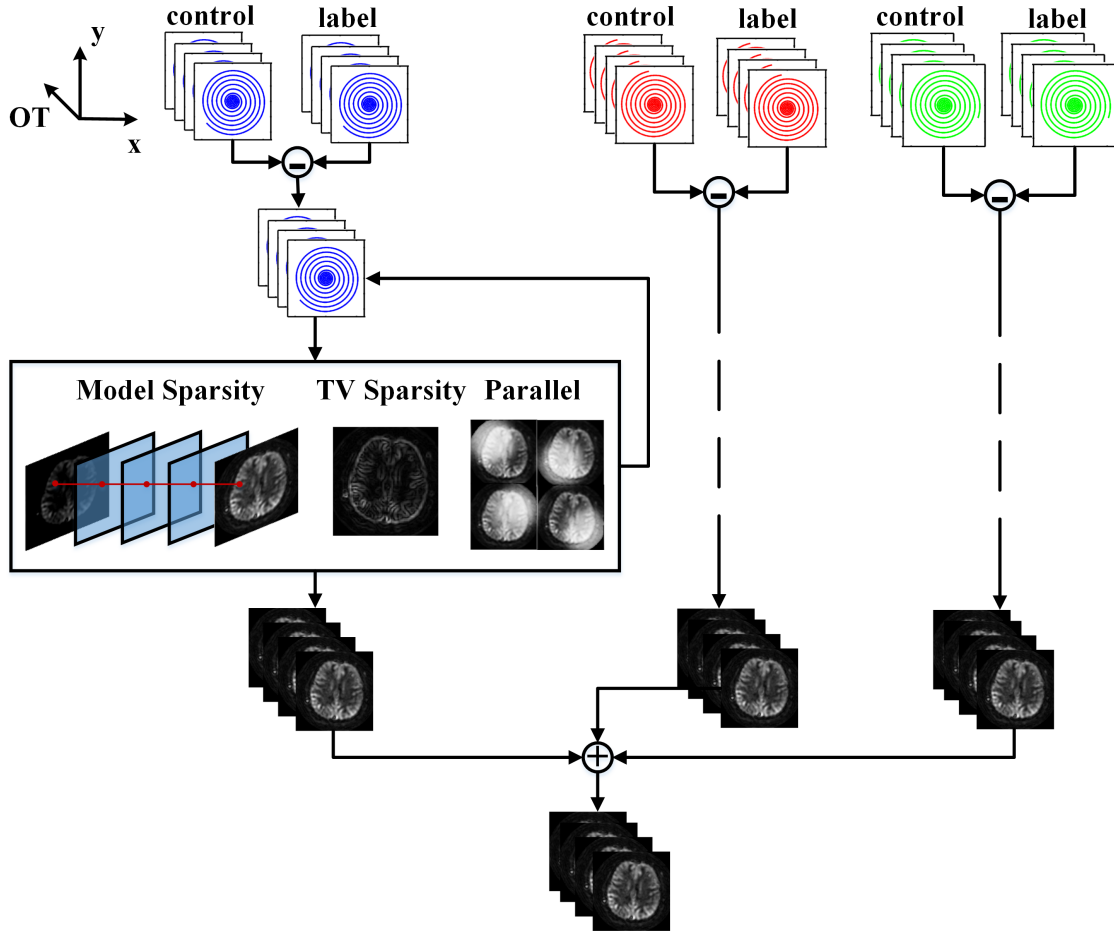


Figure 4.2: Overview of model-based reconstruction. The acquired data are processed separately according to the spiral initial angles. We subtract each label image dataset from the corresponding control image dataset to generate the k-space data with ASL contrast. The ASL images are recovered in a compressed sensing iterative reconstruction by pursuing model-based sparsity, spatial sparsity, and data consistency across multiple channel measurements.

4.3.2 Vessel Suppression

Adiabatic BIR4 preparation pulses were used to suppress the vascular blood signal, because intravascular signal often manifests as a bright spot in subtracted perfusion images and can result in over-estimation of CBF. To reduce the RF pulse duration and T_2 weighting, a single lobe crusher was used with gradient amplitude 22 mT/m, duration 5000 μs and rise time 440 μs . For the blood flow with laminar model, maximum vessel velocity is 1.5 cm/s at the first zero-cross of the attenuated sinc function [87].

4.3.3 Imaging Sequence

k-space data were collected with stack of spirals using a 3D turbo spin echo sequence [1, 81]. In-plane spiral encoding was inserted between hard RF refocusing pulses and phase encoding along the slice direction was performed centrically (Fig. 4.3a). Each echo in a particular TSE echo train collected the same spiral interleaf, with different through-plane phase encodings sampled during the echo train. RF chopping between averages was used to achieve a better slab selection profile by rotating the phase of refocusing RFs by 180 degrees on even averages [88]. Two dummy scans were performed before ASL data collection to build up steady state for the background signal.

4.3.4 Dual Density Spiral

Parallel imaging was used to accelerate ASL in-plane imaging by exploiting redundant information among multiple receiver channels. A dual-density spiral trajectory was used to acquire k-space, with 100% of Nyquist sampling during the first 1/4 of the readout and

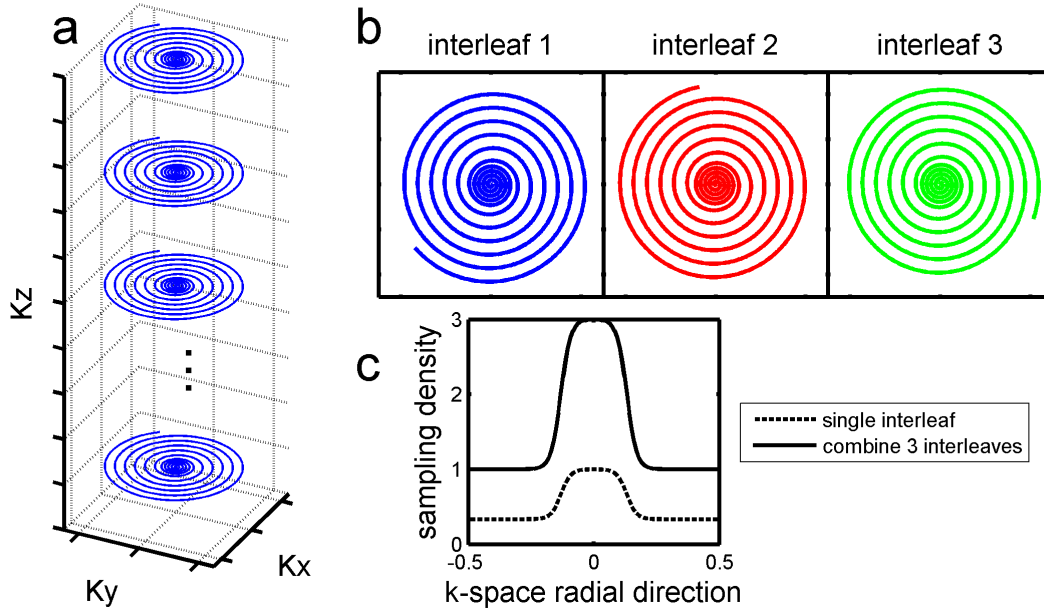


Figure 4.3: Dual-density spiral with 3D TSE k-space trajectory. In this TSE sequence, each echo train samples a particular spiral interleaf while the z direction is encoded centrally (a). Each dual-density spiral interleaf fully samples the center of k -space (dashed line in c), providing auto-calibration data for parallel image reconstruction. With different initial spiral angles (b), multiple interleaves can be combined into an oversampled k -space (solid line in c) and reconstructed by a simple gridding method for comparison with accelerated image reconstruction methods.

under-sample at a factor of 3 during the rest of the readout. The dual-density design covers a larger k -space area than a Nyquist-sampled constant-density spiral with similar readout length. Therefore, it enables single-shot imaging, reduces the scan time and improves the motion robustness.

By rotating the spirals, multiple dual-density spirals can be combined to form an oversampled k -space (Fig. 4.3b and Fig. 4.3c). This data can be reconstructed by gridding in k -space, yielding a reference image reconstructed using a standard method. This reference image can then be compared to images reconstructed using parallel imaging and compressed sensing methods.

4.4 Simulation

To demonstrate the performance of compressed sensing with a model-based constraint, a numerical phantom was used to mimic dynamic ASL imaging and CBF estimation. A numerical brain phantom [70] was separated into white matter (WM), gray matter (GM) and high perfusion (HP) ROIs, corresponding to CBF 20, 50, 80 ml/100g/min. The dynamic perfusion signal of each pixel was generated based on the local CBF value and calculated by the ASL dynamic model above. Nine perfusion images were simulated at OT = 600, 1100, 1600, 2100, 2600, 3100, 3600, 4100 and 4600 ms. Other parameters were chosen as follows: normalized equilibrium blood signal $M_{0,blood} = 1$, tissue blood partition coefficient $\lambda = 0.9$, tissue $T_1 = 1500$ ms, blood $T_{1,blood} = 1660$ ms, tagged bolus duration $\tau = 2000$ ms.

The noiseless dynamic ASL images were projected onto the trained dictionary, so as to verify the accuracy and sparsity of the model-based dictionary. For noisy ASL images, we assumed the signal could be recovered by enforcing its sparsity on the dictionary. This hypothesis was tested by representing the noisy dynamic ASL images with a few primary coefficients of the dictionary.

To test the performance of the model-based constraint on motion artifacts, we simulated random motion by translating the control image at OT 3600 ms, which mimicked rigid motion between the acquisition of control and label images.

To verify the noise suppression of proposed method, Gaussian noise was added, with $\sigma = 0.002$. The SNR was about 10, according to the highest signal in all perfusion images and was lower for the early/late OTs and low perfusion regions. These images were sampled to k-space and reconstructed by compressed sensing method. Spatial sparsity and model-

based sparsity have separate effects on image quality. To verify additional improvement by introducing the model-based sparsity, we reconstructed ASL images using spatial sparsity first and selected the Lagrange multiplier with the best performance. Then, the model-based constraint was added and evaluated.

In the simulation, because of the prior knowledge of the phantom structure, we can quantify the SNR more accurately by using the local standard deviation::

$$SNR = \frac{mean(ROI)}{std(ROI)} \quad (4.12)$$

Image structure and artifacts were also evaluated via the root of mean squared error (RMSE) and structural similarity index (SSIM) [71], compared to noiseless and motionless images.

4.5 In Vivo Measurements

4.5.1 Dynamic ASL Protocol

Six volunteers were imaged on a 3 Tesla Siemens Trio scanner (Erlangen, Germany) with a 12-channel head coil receiver array and body coil transmission. The scan followed the protocol approved by the University of Virginia and written informed consent was obtained from each subject.

For the multiple-OT ASL measurements, single-shot dual-density spiral scanning was used with an in-plane acceleration factor of 2. The spiral readout duration was 6 ms and the FOV was 200 mm, which gave a nominal spatial resolution of 4.5 mm \times 4.5 mm. The whole brain was covered by 24 slices with thickness 4.5 mm. Four pairs of control and label

images were averaged to improve SNR. Three repetitions of the dual-density spiral were performed with different initial spiral angles. TR was 5 s and TE was 22 ms. For each OT measurement, the total scan time was about 2 minutes.

To observe the early perfusion signal of a 2000 ms blood bolus, 9 OTs were designed by varying pCASL tagging durations and PLDs (Table 4.1). In the case of bolus duration less than 2000 ms, we assumed the blood bolus to remain in proximal artery by using a PLD much shorter than the ATT. In this way,, we are able to observe the entire dynamic ASL signal, even if only a portion of the blood bolus has arrived at the microvasculature at a given time.

Table 4.1: Observation Time Design (ms)

Design OT	600	1100	1600	2100	2600	3100	3600	4100	4600
Bolus Duration	500	1000	1500	2000	2000	2000	2000	2000	2000
Sequence PLD	100	100	100	100	600	1100	1600	2100	2600

To improve the CBF estimation, a saturation recovery sequence with the same 3D stack-of-spirals sequence and the same resolution was employed to measure a T_1 map. This sequence used two averages and was repeated 5 times with different TRs (1s, 2s, 3s, 4s and 5s) to acquire images with different T_1 weighting.

4.5.2 ASL Image Analysis

Image reconstruction and data analysis were performed by MATLAB 2012b (The MathWorks, Inc.) on a 4x GTX 680 Workstation (Amax Information Technologies, Inc.) with 12 CPUs (Intel Xeon E5-2640 2.50GHz Processor LGA2011).

A T_1 map was calculated from saturation recovery scans with multiple TRs. The images from each TR was reconstructed by SPIRiT. The equilibrium magnetization of the brain

signal M_0 and the T_1 map was estimated by minimizing the least squared error of the saturation recovery equation:

$$M_{sat} = M_0 \left(1 - \exp \left(-\frac{TR}{T_1} \right) \right) \quad (4.13)$$

ASL images ΔM_i from multiple observation times OT_i were fitted to the dynamic ASL model with minimization of the least squared error, resulting in model fitting CBF (M-CBF) and model fitting ATT (M-ATT).

In addition to calculating M-CBF and M-ATT based directly on fitting the images to a perfusion model, we tested other methods for calculating an ATT map and the associated CBF map. The PLD weighted delay method [20] is a robust method for calculating ATT. Because there is a monotonic relationship between ATT and averaged dynamic images with PLD weighting, we can obtain ATT reliably using a lookup table of weighted delays without knowledge of CBF. Here we developed a similar generalized weighted delay method based on our multiple-OT acquisition. The ATT map (W-ATT) is calculated based on the monotonic relationship between ATT and a weighted average of the images:

$$WT = \frac{\sum_{i=1}^9 OT_i \cdot \Delta M_i}{\sum_{i=1}^9 \Delta M_i} \quad (4.14)$$

Both methods showed the weighted delay as a monotonical function of ATT and insensitive to different CBFs. In PLD weighted delay method, when the ATT is smaller than the shortest PLD (0.7 s), the blood bolus has all arrived in brain tissue at imaging time and changes in ATT only results in ASL signal recovery difference, which is too small to detect,

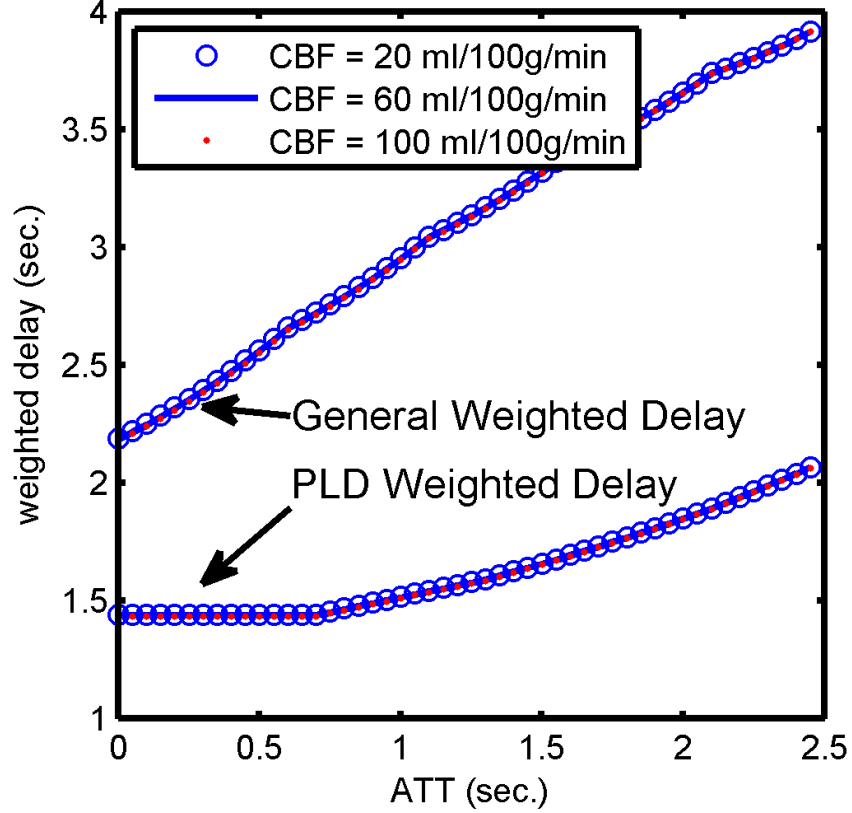


Figure 4.4: A general weighted delay in ATT calculation. Weighted by observation time, it keeps the monotonically increasing function for small ATT. In comparison, the PLD weighted delay method shows a flat region, which is insensitive to ATT changes. Both methods show similar robustness to the changes in CBFs.

shown as the flat region in Fig. 4.4. The general weighted delay acquires ASL images before the blood bolus all arrived and can estimate the small ATT more accurately.

Using the W-ATT, a CBF map was calculated at OTs that contain ASL signal (OT=1600, 2100, 2600, 3100, 3600, 4100 and 4600 ms) and averaged to obtain a weighted CBF (W-CBF).

Arterial cerebral blood volume (aCBV) was calculated by the product of the ATT map and the CBF map [89]:

$$aCBV = ATT \cdot CBF \quad (4.15)$$

This was designated as model-fitting aCBV (M-aCBV) and weighted average aCBV (W-

aCBV) below.

To compare with the performance of the proposed method, volunteer data were also reconstructed by a gridding method and a parallel imaging method with SPIRiT reconstruction. The residual error in M-CBF calculation and the SNR from the highest perfusion signal measurement were analyzed by the Wilcoxon signed-rank test. Two ROIs were chosen based on the T1 map: white matter (WM) 10-1300 ms and gray matter (GM) 1300-1900 ms.

To test the improvement in the CBF map by the proposed method, we compared the different reconstruction methods in a low SNR case. Low SNR images were obtained by using 1/3 of the data. The gridding method, the parallel image reconstruction and the proposed method were used to reconstruct the ASL images, which provided the low SNR CBF maps. Because DSC images were not available, we treated the CBF map from all available ASL data as a high SNR gold standard. By comparing the similarity of CBF maps between high SNR and low SNR cases, we evaluated the performance of reconstruction methods and analyzed the results by the Wilcoxon signed-rank test across six volunteers.

In order to independently assess image quality and the resulting parameter maps, a neuroradiologist graded the images using a Likert scale (1 for strongly disagree; 2 for disagree; 3 for neither agree nor disagree; 4 for agree and 5 for strongly agree). Seven criteria were evaluated: no motion artifact in perfusion images, good dynamic contrast in perfusion images, good CBF map quality with traditional model fitting, good CBF map quality with weighted average, good ATT map quality with traditional model fitting, good ATT map quality with weighted average, good aCBV map quality with traditional model fitting and good aCBV map quality with weighted average.

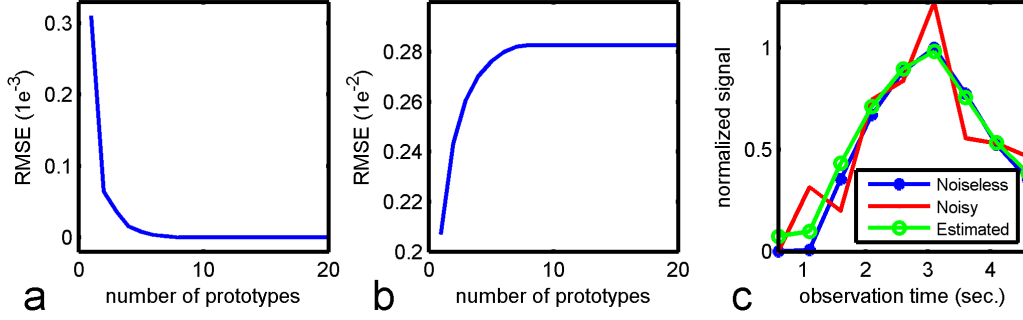


Figure 4.5: The trained dictionary represents the ASL signal. For noiseless data (a), only a few prototypes are needed to represent the signal with high accuracy. For noisy data (b), image denoising can be performed by projecting the signal onto a few prototypes. One selected ASL pixel illustrates that a dictionary representation can approximate the noiseless signal accurately (c).

4.6 Results

4.6.1 Simulation Results

The simulated multi-OT ASL images were represented by the over-complete dictionary and the approximation errors are shown in Fig. 4.5. The noiseless ASL signal was accurately approximated using just a few prototypes in the dictionary (Fig. 4.5a). More prototypes yielded improved signal approximation but also tend to approximate the noise, because of the low SNR of the ASL signal (Fig. 4.5b). In Fig. 4.5c, a noisy ASL signal ($\text{MSE} = 3.39\text{e-}6$) was projected onto the dictionary, then represented by a few primary prototypes, which suppresses noise and recovers the signal ($\text{MSE} = 3.36\text{e-}7$).

Fig. 4.6 shows that the model-based constraint reduced motion artifacts significantly. The rigid bulk motion resulted in ring-like artifacts around brain and a bright spot in the CSF region, as shown in noiseless ASL (a). Because this random motion artifact did not follow the ASL signal decay model, it was suppressed by the model-based dictionary (b). As

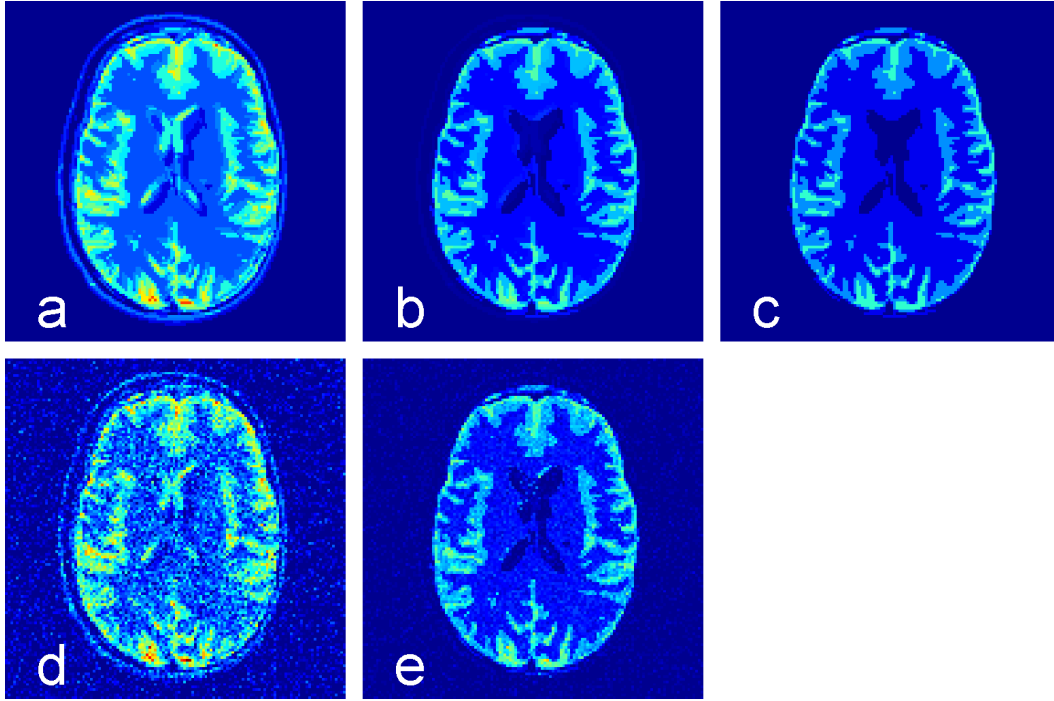


Figure 4.6: Model-based sparsity reduces motion artifacts in multi-OT ASL images. In the noiseless case, one of the dynamic ASL images contained motion artifact (a) from subtraction between control and label images. By projecting the multi-OT signal onto the model-based dictionary, the motion artifact was eliminated (b), because its dynamic pattern was distinct from the ASL model. As a reference, the noiseless and artifact-free image is shown in (c). Similar results were shown with noisy data (d, e).

a reference, the noiseless and motionless image is shown in (c). Similarly, in noisy data (d), the motion artifact and background noise were suppressed by projecting the dynamic signal onto the dictionary (e). Some motion artifacts remain near the CSF region in (e), because some random noise was fitted into the ASL model and represented by the dictionary.

The performance of constrained reconstruction depends on the choice of Lagrange multiplier. To demonstrate the image quality improvement achieved by enforcing model-based sparsity, the multipliers were chosen in two steps. First, with a spatial constraint only, we searched for the best TV weight minimizing RMSE. It was an "L-curve" as shown in Fig. 4.7 (left) and the minimum RMSE was achieved with the TV weight 0.0027. Then, model-based

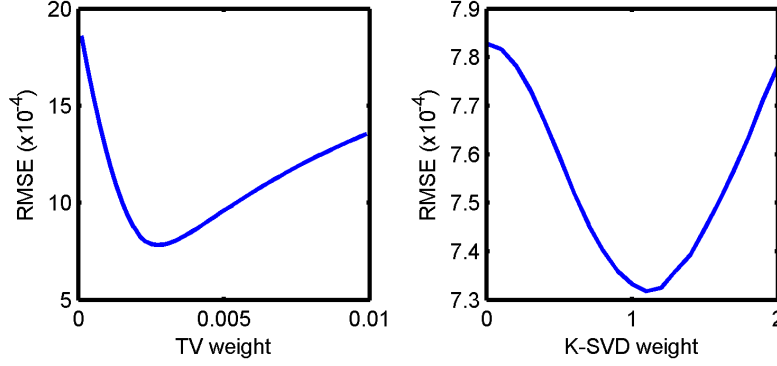


Figure 4.7: Regularization parameter searching in compressed sensing. Left: RMSE changed with spatial TV weights only. Based on the RMSE, the best TV weight was fixed at 0.0027. By adding the K-SVD constraint, we can reduce the error further (right)

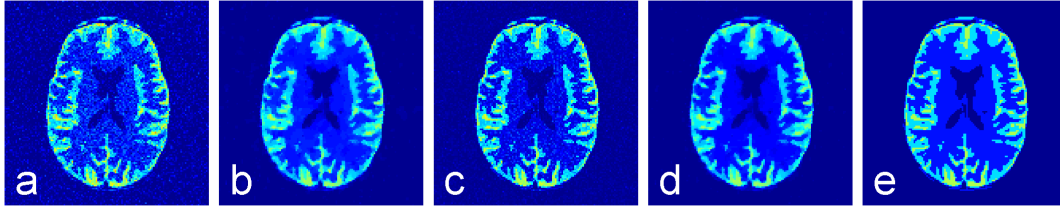


Figure 4.8: Simulated ASL images reconstructed by compressed sensing. The complex Gaussian noise in initial images (a) was suppressed by the compressed sensing reconstruction with spatial TV constraint (b) and model-based sparsity (c). By combining spatial and model-based sparsity, the image quality is improved further (d). The noiseless image (e) is shown as reference.

sparsity was combined with this "best" TV. From Fig. 4.7 (right), the RMSE was further reduced and K-SVD achieved its best performance at weight 1.1.

The above results are more clearly demonstrated in simulated ASL images (Fig. 4.8). Spatial TV (b) suppressed noise and improved the ASL image SNR. Model-based reconstruction (c) enforced the signal changes in OT encoding space towards the dynamic model and suppressed noise along the OT encoding dimension. The combination of the above two types of sparsity (d) improved the image quality further. Initial noisy images (a) and ideal images (e) are also shown for reference.

Quantitation of local SNR and estimation error are shown in Table 4.2. For all ROIs, the

compressed sensing reconstruction increased the SNR and the model-based sparsity improved it further. Compared with the noiseless ASL signal, compressed sensing with TV and K-SVD constraints increased the image similarity, reduced the error from background noise by a factor of 2.7, and reduced the residual in perfusion maps by a factor of 1.8.

Table 4.2: Improvement of ASL images quality and CBF map by compressed sensing.

	WM	GM	HP	Image	Image	CBF	CBF
	SNR	SNR	SNR	SSI	RMSE(e^{-4})	RMSE	residue
Initial	2.4	5.8	9.6	0.71	20	9.4	68.0
TV	5.3	7.8	11.3	0.83	7.8	7.1	39.3
Model	2.7	9.4	15.4	0.78	10.0	8.5	43.1
TV+Model	5.3	8.4	12.4	0.87	7.3	6.2	38.1

4.6.2 Experiments Results

Fig. 4.9 shows one slice from a 3D dynamic pCASL image set from a volunteer experiment. The simple non-Cartesian gridding reconstruction (a) resulted in high background noise and motion artifacts. Parallel reconstruction with SPIRiT (b) reduced noise and stabilized the image. As demonstrated by simulation, the compressed sensing reconstruction (c) suppressed the noise in the background and improved the SNR of volunteers ASL images further.

The proposed method corrected artifacts from motion. As highlight by the arrows in Fig. 4.9, the brain had rigid bulk motion between control and label measurements, which resulted in ring-like motion artifacts. Because the motion occurred irregularly, the model-based constraint eliminated the artifact as it had a poor representation in the model-based dictionary.

The CBF maps are shown on the right of Fig. 4.9. In the residual maps of CBF fitting, the proposed method reduced the residual in GM and WM regions, compared with the

gridding and parallel image reconstructions. It also reduced the error from CSF, which does not contain perfusion signal, and the edge of brain, which exhibits motion artifacts.

To show the improvement in accuracy of the proposed method, we considered the high SNR result from all the acquired data to be a gold standard and compared the CBF map from only one third of acquired data to it, which reduced the total scan time from 18 minutes to about 6 minutes. The results suffered lower SNR, became unstable and had higher fitting error with a parallel image reconstruction. Compressed sensing reconstruction (e) reduced the residual compared to the parallel reconstruction (d). The proposed method results in a CBF map that provided a better approximation to the high SNR results (a, b, c).

Fig. 4.10 is the statistical analysis of the six volunteers' images. Fig. 4.10a shows SNR improvement using the proposed method. In the gray matter region, the compressed sensing method significantly improved the SNR ($P < 0.05$) compared with gridding and parallel image reconstruction. Fig. 4.10b shows the model residual of CBF estimation in volunteers. The proposed method resulted in less estimation error versus parallel and gridding reconstruction in white matter ($P < 0.05$). Also, significant improvement is achieved in the grey matter compared with parallel imaging. If we treat the high SNR CBF map from all available data as a gold standard, the CBF maps from only 1/3 of data were evaluated by the similarity index, as shown in Fig. 4.10c. The proposed method resulted in significantly higher similarity to the high SNR results.

Table 4.3 shows the blinded reading scores of six volunteers' images by the neuroradiologist. The proposed method and the parallel reconstruction provided better image quality and parameter maps than the gridding reconstruction. The proposed method showed better dynamic contrast. The proposed method improved ATT and aCBV maps calculated

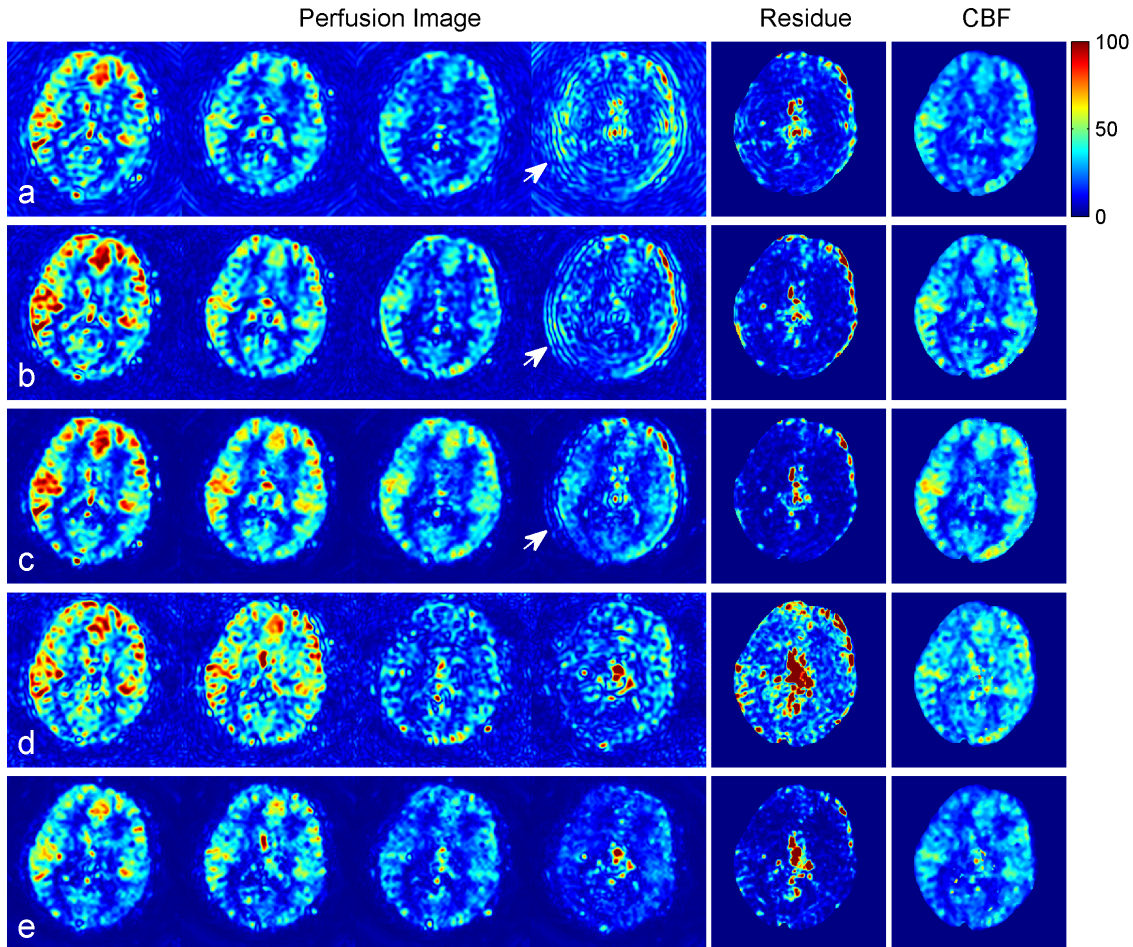


Figure 4.9: Dynamic pCASL perfusion images from selected OTs (2600, 3100, 3600, 4100 ms) in a normal volunteer. The gridding reconstruction (a) showed high motion artifacts and background noise. The SPIRiT reconstruction (b) eliminated most of the under-sampling artifacts of the dual-density spiral acquisition. The model-based reconstruction suppressed background noise and reduced the estimation error in the CBF (c). As the arrow highlights, the motion artifacts obtained using the gridding method (a) and SPIRiT reconstruction (b) were suppressed when the model-based sparsity constraint was used (c). When using only 1/3 of the acquired data and reducing the scan time to 40s at each OT, the SNR of perfusion images dropped quickly in SPIRiT and more error was shown in CBF calculation (d). Again, the proposed method improved the images, reduced the fitting error, and provided a similar CBF map to the high-SNR results (e). Center: Dynamic model fitting residual (a.u.). Right: CBF map (ml/100g/min).

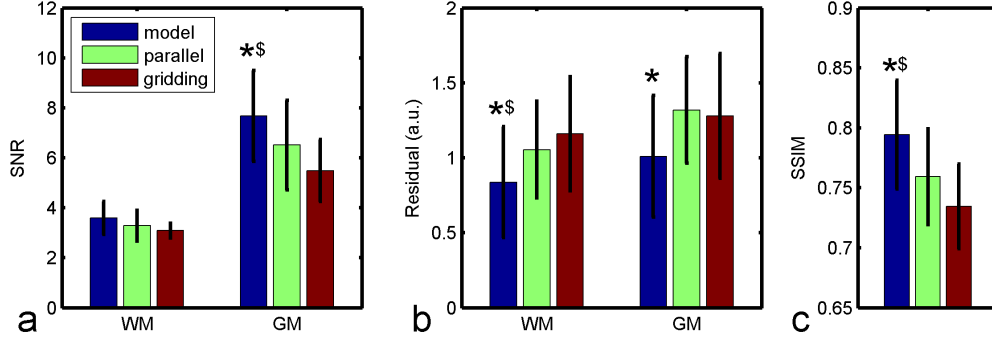


Figure 4.10: ASL image SNR and CBF estimation residual in volunteers ($N = 6$, mean \pm standard deviation). ROIs of grey matter (GM) and white matter (WM) were chosen based on T1 value. Compared with gridding and parallel image reconstruction, the proposed method improved SNR (a) and reduced estimation residuals (b) significantly. With 1/3 of the data, the proposed method also provided better structural similarity to the high SNR results (c). (In the same ROI, * $P < 0.05$ versus the parallel reconstruction method; \$ $P < 0.05$ versus the gridding method).

using the weighted average method. It also improved CBF and aCBV calculated using the model fitting method. The CBF, ATT and aCBF maps calculated with the weighted average method were preferred to the model fitting results.

Table 4.3: Mean rating of images and parameter maps from six volunteers in a blinded evaluation by a neuroradiologist.

	motion robust	dynamic contrast	M- CBF	W- CBF	M- ATT	W- ATT	M- aCBV	W- aCBV
Gridding	3.3 ± 0.8	3.7 ± 1.0	3.5 ± 0.5	4.7 ± 0.5	3.3 ± 0.8	3.5 ± 0.8	2.3 ± 0.8	3.2 ± 0.4
Parallel	4.5 ± 0.8	4.3 ± 0.8	3.8 ± 0.4	5.0 ± 0.0	3.7 ± 0.5	3.8 ± 0.8	2.7 ± 0.8	3.3 ± 0.5
Model	4.0 ± 0.6	4.5 ± 0.8	4.2 ± 0.8	4.8 ± 0.4	3.5 ± 0.8	4.0 ± 0.6	3.3 ± 0.5	3.8 ± 0.4

4.7 Discussion

This work presents a model-based image reconstruction for dynamic ASL perfusion imaging. The method was combined with single-shot 3D acquisition and parallel imaging, yielding whole-brain dynamic ASL image acquisition in 40 seconds to 2 minutes per temporal frame. In this method, prior knowledge of the dynamic ASL signal time course was exploited to

distinguish the ASL signal from noise and random motion artifacts. This compressed sensing image reconstruction method improved ASL image quality and robustness and yielded accurate CBF estimates. The results in this chapter were achieved without background suppression or motion compensation, in order to demonstrate the intrinsic robustness of the method.

As a reconstruction strategy, the proposed method is compatible with most current techniques in dynamic ASL. The proposed method can easily be adapted to use Cartesian readouts, such as 2D echo planar imaging or 3D GRASE [89]. While the model-based reconstruction intrinsically suppresses motion artifacts, motion compensation would further improve the robustness of the method. Background suppression could be added to further suppress artifacts. The method could be combined with new RF labeling pulse techniques, such as Hadamard encoding [52, 53].

Model-based sparsity assumes the signal in each pixel follows a given dynamic ASL model, with the parameters of the model varying from pixel to pixel. Here, we simply chose the basic CASL model [14]. An improved model could describe perfusion more accurately, for example by including the arterial input function (AIF) [23], but a complex ASL dynamic model could also require more OT measurements to estimate the parameters precisely, thus increasing imaging time.

The K-SVD method enforces the sparsity of the low-dimensional signal of ASL using an over-complete dictionary. The training data set included signal prototypes based on all reasonable values of the perfusion parameters (CBF and ATT). More accurate parameter ranges can be determined based upon a particular application, which will improve the sparsity and accuracy of representation in the dictionary. More prototypes in the K-SVD dictionary may

further improve the sparse representation, but would also increase the computational complexity for the orthogonal matching pursuit and prolong reconstruction time. Moreover, in our work, minor differences were noticed between dictionary sizes ranging from 32 to 512.

In the compressed sensing reconstruction, the model-based sparsity limits the way we prepare the initial k-space data y . Perfusion contrast in ASL is obtained by subtracting tagged images from control images. The low SNR in perfusion images makes it difficult to distinguish signal from noise. Therefore, to maximize the performance of spatial sparsity, one might propose to apply the compressed sensing reconstruction to control and label images separately prior to subtraction. However, because the ASL signal is less than 1% of normal MRI images, the dynamic evolution of ASL is too small to extract from the background signal before subtraction, so it would be difficult to exploit model-based sparsity based on component images. Therefore, in this work, we subtracted the k-space data of the label images from that of the control images as the first step in the image reconstruction. This complex subtraction may be less robust than magnitude subtraction, because it is more sensitive to variations in signal phase.

This work used a pCASL tagging method with the length of the tagging pulse reduced for early observation times. This tagging scheme was combined with a new general weighted-delay method of calculating perfusion maps. The combination of these two methods made it possible to begin measuring the ASL signal when only part of the blood bolus has arrived at the tissue of interest (Table 4.1). This in turn makes it possible to catch the rising edge of the perfusion signal and to detect small ATT values. So, changing the length of the tagging pulse has advantages in the design of dynamic pCASL experiments, but it does change the perfusion bolus duration. The alternative would be a more conventional design with constant

perfusion bolus duration and variable post-label delay. The reliability and accuracy of this variable perfusion bolus technique should be further evaluated in a future study.

This study used equally-spaced observation times. However, CBF estimation accuracy might be improved by optimal observation-time design (Zhao and Meyer, 2013, 2012). Non-equally-spaced sampling in the parameter encoding space might break the assumptions of some sparsity constraints, such as temporal TV, but it can be adapted into model-based sparsity by proper dictionary training.

4.8 Conclusion

This work introduces model-based compressed sensing to improve ASL image quality and CBF accuracy. By enforcing sparsity in the observation-time encoding domain, noise and motion artifacts were suppressed and the estimated CBF maps were more accurate. These benefits can be used to accelerate dynamic ASL, so that it can be achieved in a feasible scan time.

Optimal ASL Experiment

Dynamic arterial spin labeling (ASL) can provide important information (such as cerebral blood flow maps) for the care of stroke and brain tumor patients. Currently this technique requires significant signal averaging to improve image quality and parametric accuracy. By sampling the perfusion bolus at multiple observation times (OT) instead of simply averaging the signal at one OT, we can obtain additional perfusion parameters and achieve more accurate estimation. The design of OTs and the design of estimators are conventionally based on a Gaussian noise assumption. However, in a rapid dynamic perfusion experiment, the signal-noise-ratio is low and we cannot approximate the noise of an MRI magnitude signal by a Gaussian model. Using an inaccurate noise model will result in biased parameter estimation with the least squares method and a sub-optimal OT design. In this chapter, we present new methods for solving two related problems: (1) the optimal design of OTs for a dynamic ASL experiment assuming a realistic Rician noise model; and (2) an unbiased maximum likelihood estimator of perfusion parameters from dynamic ASL data assuming a Rician noise model.

5.1 Introduction

ASL provides a non-contrast, non-invasive perfusion imaging option for patients. It labels the natural signal of blood by inversion of its longitudinal magnetization and acquires the perfusion image in a downstream slice of interest. Modeling the spins in blood as a freely diffusible tracer, ASL is used to generate cerebral blood flow (CBF) maps. To measure the dynamics of cerebral perfusion, it is possible to measure images at multiple OTs and then use nonlinear regression to estimate the parameters in a perfusion model. However, the blood signal decays with longitudinal relaxation rate T_1 as it transits from the labeling region to the capillary exchange site. Typical ASL images contain 1% of the signal of a conventional MR image. Therefore, low SNR is a key limiting factor of ASL.

In addition to improved tagging techniques and image reconstruction methods, we can also improve the CBF map by experimental design with no extra scan time. As an estimation problem, optimal OT design will provide precise (stable, lower variance) and accurate (close to the real value) results.

In estimation theory, the variance of a parameter estimated from noisy data is subject to the Cramér-Rao lower bound (CRLB) [90]. By designing OTs, we try to maximize the Fisher matrix so as to minimize the CRLB. Even if the CRLB is not achievable, some researchers have shown the benefits of maximizing the Fisher matrix so as to minimize the variance of our estimated parameters [91, 92].

This lower bound can be approached by maximum likelihood estimation (MLE) when the data set is large enough, regardless of the noise model. In the case of additive white Gaussian noise, a least squared (LS) error estimator equates to MLE and therefore yields

an efficient estimator, which should be better than other estimators, such as absolute error (L1) estimator.

MRI acquisition results in complex Gaussian noise, and after the magnitude operation it has a Rician distribution. With high SNR, the Rician noise can be approximated by a Gaussian distribution, which is the conventional noise model in optimal experimental design. This assumption is usually true in MRI, such as in T_1 mapping, where the SNR is typically more than 10. In the case of ASL perfusion images, the SNR is low and the Rician noise can no longer be accurately approximated by a Gaussian model. Thus, a LS estimator results in biased estimation and the more general method of MLE is needed for an unbiased estimate [93]. Therefore, the optimal design should follow the actual Rician model.

In this work, we will present the optimal OT design for CBF estimation based on a pCASL single-compartment dynamic perfusion model and compare the resulting accuracy using both LS and L1 estimators with a Gaussian noise model. Further, a more practical situation with Rician noise and low SNR will be considered. A new optimal OT design and an unbiased maximum likelihood estimator are designed with a Rician noise model. The new designs are evaluated in a numerical phantom study and a volunteer scan.

5.2 Theory

5.2.1 Cramér-Rao Lower Bound

Multiple-OT ASL images provide accurate CBF maps by fitting to a dynamic perfusion model. The variance of the CBF estimate can be further reduced by optimal OT design.

For N OTs, the measured signal $y(i)$ can be expressed as:

$$y(i) = f(x, n(i), i), 1 \leq i \leq N \quad (5.1)$$

where x is the parameter to be estimated and the $n(i)$ are the noise in the measurements and are assumed to be independent and identically distributed random variables (i.i.d.).

There are various estimators that yield optimal estimates \hat{x} that satisfy a particular criterion. The key questions are what is the most accurate estimator, whether it exists and whether it is reachable. The Cramér-Rao lower bound gives the lower bound on the variance of the estimated parameter, in terms of only the statistical properties of the observations. It assumes the probability density function $p(y|x)$ satisfies the 'regularity' condition:

$$E \left[\frac{\partial \ln p(y|x)}{\partial x} \right] = 0 \quad (5.2)$$

where the expectation is taken with respect to $p(y|x)$.

Then any unbiased estimator \hat{x} satisfies:

$$\text{var}(\hat{x}) \geq \frac{1}{\mathcal{F}} \left(\frac{d\psi(y)}{dy} \right)^2 \quad (5.3)$$

where $\psi(y)$ is the estimator of x

\mathcal{F} is the Fisher information matrix:

$$\mathcal{F} = -E \left[\frac{\partial^2 \ln p(y|x)}{\partial x^2} \right] = E \left[\left(\frac{\partial \ln p(y|x)}{\partial x} \right)^2 \right] \quad (5.4)$$

This lower bound can be achieved if and only if

$$\frac{\partial \ln p(y|x)}{\partial x} = \mathcal{F}(x)[\psi(y) - x] \quad (5.5)$$

The efficient estimator is

$$\hat{x} = \psi(y) \quad (5.6)$$

It achieves the minimum variance unbiased result:

$$\text{var}(\hat{x}) = \frac{1}{\mathcal{F}(x)} \quad (5.7)$$

5.2.2 Gaussian Noise

Suppose the observation is contaminated by additive noise n :

$$y = f(x) + n \quad (5.8)$$

In the case of Gaussian distributed noise and an unbiased estimator, the best estimate is achieved when

$$E[(\hat{x} - x)^2|x] \geq \frac{1}{\mathcal{F}} = \sigma^2 \frac{1}{\left(\frac{\partial f(x)}{\partial x}\right)' \left(\frac{\partial f(x)}{\partial x}\right)} \quad (5.9)$$

More details are provided in Appendix 5.A.

Multiple optimization criteria can be set for the Fisher information matrix, such as the determinant (D-optimality) criterion. Here we choose to minimize the variance in CBF estimation.

With a dynamic ASL signal model, the optimal OTs are given as:

$$\hat{t} = \arg \min_t \frac{\mathcal{F}(2, 2)}{\mathcal{F}(1, 1)\mathcal{F}(2, 2) - \mathcal{F}(1, 2)\mathcal{F}(2, 1)} \quad (5.10)$$

where

$$\mathcal{F} = E \begin{bmatrix} \sum \left(\frac{\partial \Delta M}{\partial f} \right)^2 & \sum \frac{\partial \Delta M}{\partial f} \frac{\partial \Delta M}{\partial \Delta t} \\ \sum \frac{\partial \Delta M}{\partial \Delta t} \frac{\partial \Delta M}{\partial f} & \sum \left(\frac{\partial \Delta M}{\partial \Delta t} \right)^2 \end{bmatrix} \quad (5.11)$$

$$\frac{\partial \Delta M}{\partial f} = 2M_0\alpha T_1 \exp\left(-\frac{\Delta t}{T_{1,b}}\right) Q \quad (5.12)$$

$$\frac{\partial \Delta M}{\partial \Delta t} = \begin{cases} 0 \\ 2M_0\alpha f T_1 \left(-\frac{1}{T_{1,b}} \exp\left(-\frac{\Delta t}{T_{1,b}}\right) + \left(\frac{1}{T_{1,b}} - \frac{1}{T_1} \right) \exp\left(-\frac{\Delta t}{T_{1,b}}\right) \exp\left(-\frac{t-\Delta t}{T_1}\right) \right) \\ 2M_0\alpha f T_1 \left(1 - \exp\left(-\frac{\tau}{T_1}\right) \right) \left(\frac{1}{T_1} - \frac{1}{T_{1,b}} \right) \exp\left(-\frac{\Delta t}{T_{1,b}}\right) \exp\left(-\frac{t-\Delta t-\tau}{T_1}\right) \end{cases} \quad (5.13)$$

More details are provided in Appendix 5.B.

5.2.3 Rician Noise

When a magnitude operation is performed on a data set with a complex Gaussian distribution, the distribution is changed to Rician [94, 95]. MR signals and images contain complex Gaussian noise. In parameter estimation, model regression is typically performed on magnitude images, which is contaminated by Rician noise:

$$P(x, A, \sigma) = \frac{x}{\sigma^2} e^{-(x^2 + A^2)/2\sigma^2} I_0\left(\frac{x A}{\sigma^2}\right) \quad (5.14)$$

where σ is the variance of the complex Gaussian noise and A is actual signal amplitude. I_0 is the 0th-order modified Bessel function of the first kind.

In the high SNR situation, the Rician distribution can be approximated by a Gaussian distribution, and thus optimal OT design combined with a conventional LS estimator could provide accurate CBF estimation. However, when the SNR is low, the resulting Rician noise will result in biased estimation and sub-optimal experimental design if the Gaussian approximation is used. Dynamic ASL images intrinsically have low SNR; therefore, we need to use a Rician noise model in the design of both the OTs and the estimator.

The general maximum likelihood estimator with a Rician noise model is as follows:

$$\left(\frac{\partial \Delta M}{\partial f}\right)^T \mathbf{V}(\mathbf{I}S - \Delta M) = 0 \quad (5.15)$$

where

$$\mathbf{V} = \begin{pmatrix} \frac{1}{\sigma_1^2} & 0 & \cdots & 0 \\ 0 & \frac{1}{\sigma_2^2} & \cdots & 0 \\ \vdots & \vdots & \ddots & \vdots \\ 0 & 0 & \cdots & \frac{1}{\sigma_N^2} \end{pmatrix} \quad (5.16)$$

and

$$\mathbf{I} = \begin{pmatrix} \frac{I_1(z(t_1))}{I_0(z(t_1))} & 0 & \cdots & 0 \\ 0 & \frac{I_1(z(t_2))}{I_0(z(t_2))} & \cdots & 0 \\ \vdots & \vdots & \ddots & \vdots \\ 0 & 0 & \cdots & \frac{I_1(z(t_N))}{I_0(z(t_N))} \end{pmatrix} \quad (5.17)$$

with

$$z(t_k) = \frac{S(t_k)\Delta M(t_k)}{\sigma_k^2} \quad (5.18)$$

The details of the derivation can be found in [93].

The Fisher information matrix was given based on Rician noise, which leads to the optimal design of OTs. When estimating two variables from the measurements, the Fisher information matrix is 2 by 2 with elements:

$$\mathcal{F}_{i,j}(t_1, \dots, t_N) = \left(\frac{\partial \Delta \mathbf{M}}{\partial x_i} \right)^T \mathbf{V} E[\mathbf{R}] \left(\frac{\partial \Delta \mathbf{M}}{\partial x_j} \right) \quad (5.19)$$

where

$$E[\mathbf{R}]_{k,k} = -\frac{\Delta M(t_k)^2}{\sigma^2} + E \left[\frac{S(t_k)^2 I_1^2((t_k))}{\sigma^2 I_0^2((t_k))} \right] \quad (5.20)$$

The partial derivative is performed corresponding to $x_1 = f$ and $x_2 = \Delta t$.

The optimal OT design has an analytical solution with Gaussian noise model. It follows the optimization of Eq. 5.9. With the Rician distribution, the first difficulty is that the noise model is not separable and cannot be expressed analytically in a simple form. The expectation in Eq. 5.19 does not have an analytical solution. Therefore, numerical integration was used with reasonable accuracy [96]. Here, we used the recursive adaptive Lobatto quadrature method, with an interval from 0 to $10\Delta M$.

Another computational problem is the optimization of the Fisher information matrix. Due to the large N , we adopt the method in Santos's work [97] to calculate the optimal OTs iteratively. When the problem is convex, the iterative optimal results yield the global optimal Fisher matrix:

$$\mathcal{F}(t_1, t_2, \dots, t_n) = \mathcal{F}(t_1, t_2, \dots, t_{n-1}) + \frac{1}{\sigma^2} \frac{\partial \Delta M(t_n)}{\partial f} \frac{\partial \Delta M(t_n)}{\partial \Delta t} E[R_{n,n}] \quad (5.21)$$

5.3 Methods

5.3.1 Simulation

All simulations were performed using MATLAB 2013b. The classic single-compartment pseudo continuous ASL model [14] was used to simulate the dynamic pCASL signal in a selected pixel. In the optimal OT designs, we assume both ATT and CBF are unknown, and design to minimize CBF variance. Assume that we measure the ASL signal from brain perfusion with CBF 50 ml/100g/min. Other common assumptions are made for the perfusion model: tissue $T_1 = 1500$ ms, blood $T_{1b} = 1600$ ms, labeling efficiency $\alpha = 0.9$, partition coefficient $\lambda = 0.9$, bolus duration $\tau = 2000$ ms, and arterial transit time $ATT = 700$ ms.

Suppose we perform ASL imaging with a total scan time of 7 minutes. With a 5-second TR, each ASL image pair (control image and label image) is collected in 10 s. Therefore, about 40 ASL images are collected in this scan time, which can be averaged with a single-PLD measurement or can be acquired by dynamic ASL with optimal OT design.

Image SNR is specified based on the highest possible perfusion signal in the dynamic images, which can be much lower at the early and late OTs. The 'SNR' is defined by the noise level in a single measurement; for example, $SNR = 2$ means $\sigma = 0.5\%M_{0,blood}$ for one measurement (assuming the maximum ASL signal is 1% of the fully relaxed equilibrium magnitude of blood signal). When multiple measurements are averaged, the image SNR is improved by $\sqrt{\text{number of averages}}$.

Synthetic ASL data were generated, and then the CBF was estimated from noisy images. In each case, the generation and estimation are repeated 10000 times to verify the statistical

performance of OT design and estimator.

We designed the following simulations to answer these questions: (a) whether optimal OT design helps the quantification of CBF; (b) how it performs with low SNR; (c) how we improve the quantification when SNR is low.

First, we would like to verify the optimal OT design, by comparing the following different OT designs: (1) 5 evenly spaced OTs with 8 averages at each; (2) 10 evenly spaced OTs with 4 averages at each; (3) 40 evenly spaced OTs; (4) optimal OT design based on a Gaussian noise model. The CBF value was calculated by two estimators: LS and L1. To simplify the problem, we used high $\text{SNR} = 10$ here.

We then performed simulations with the more accurate Rician noise model. We contaminated the ASL image with Rician noise and estimated the CBF with a LS estimator. We used $\text{SNR} = 10$ and 2 corresponding to the high SNR and low SNR cases.

For the case of Rician noise with low SNR, we compared the performance of the maximum likelihood estimator designed with a Rician noise model to the performance of the LS estimator.

Finally, we tested the optimal OT design based on a Rician noise model and compared it to the result from optimal design with a Gaussian noise model.

5.3.2 Experiment

To assess the performance of the optimal OT design in practice, experiments were performed on a 3T Siemens scanner with healthy volunteers. 3D pCASL was used with a single-shot dual-density spiral trajectory with resolution $5 \text{ mm} \times 5 \text{ mm} \times 5 \text{ mm}$. Other parameters were as follows: TR 5380 ms (limited by SAR); TE 22 ms; 24 slices; readout 6 ms; FOV

200 mm; initial spiral density 1.0; and final spiral density 0.4. The proposed OT design was implemented with 40 optimally designed OTs based on Rician noise and two averages at each OT. The control experiment used 5 evenly spaced OTs with 16 averages at each OT.

5.4 Results

Figure 5.1 shows the improvement with optimal OT design. We assumed Gaussian noise with an $\text{SNR} = 10$ for each measurement. Four OT schemes are shown on the left. The right figure shows the estimation results from each sampling scheme. In all cases, the CBF was estimated accurately without bias. For each OT design, the LS estimator resulted in lower variance than the absolute error estimator. More importantly, both estimators yielded more precise (lower standard deviation) estimates with optimal OT design than with the other OT schemes.

Figure 5.2 shows simulations with Rician noise. With higher SNR (right, $\text{SNR} = 10$), the LS estimator yielded unbiased and precise results. This is as expected, because Rician noise is closely approximated by a Gaussian model for high SNR. The red line indicates the true CBF value in the simulation (50 ml/100g/min). When the SNR was low ($\text{SNR} = 2$), the LS estimator resulted in wider spread estimates, which corresponds to a larger standard deviation of the error estimate, as expected. It also resulted in a biased CBF value. As shown on the right, the mean value of the CBF estimates is larger than the true CBF.

Figure 5.3 demonstrates the performance of the maximum likelihood estimator with Rician noise. In the case of low SNR ($\text{SNR} = 2$) Rician noise, the maximum likelihood estimator provided accurate CBF values. The LS estimator and L1 estimator yielded biased

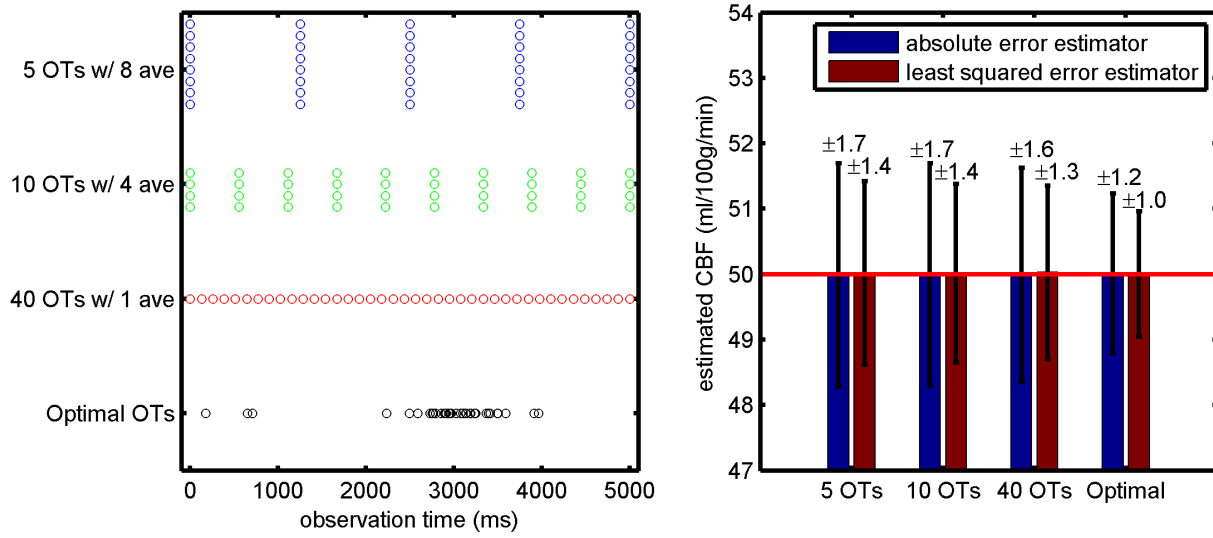


Figure 5.1: Improved estimation by optimal OT design. With the assumption of high SNR ($\text{SNR} = 10$ for each measurement), different OT designs are shown in the left figure. The optimal OTs were designed based on the Gaussian noise model. Observation time were chosen as follows: 5 evenly spaced OTs with 8 averages each; 10 evenly spaced OTs with 4 averages each; and 40 evenly spaced OTs with 1 average each. The CBF estimation results are shown in the right figure. The LS estimator yielded lower variance than the absolute error estimator. The optimal OT design yielded more precise results than the other OT schemes.

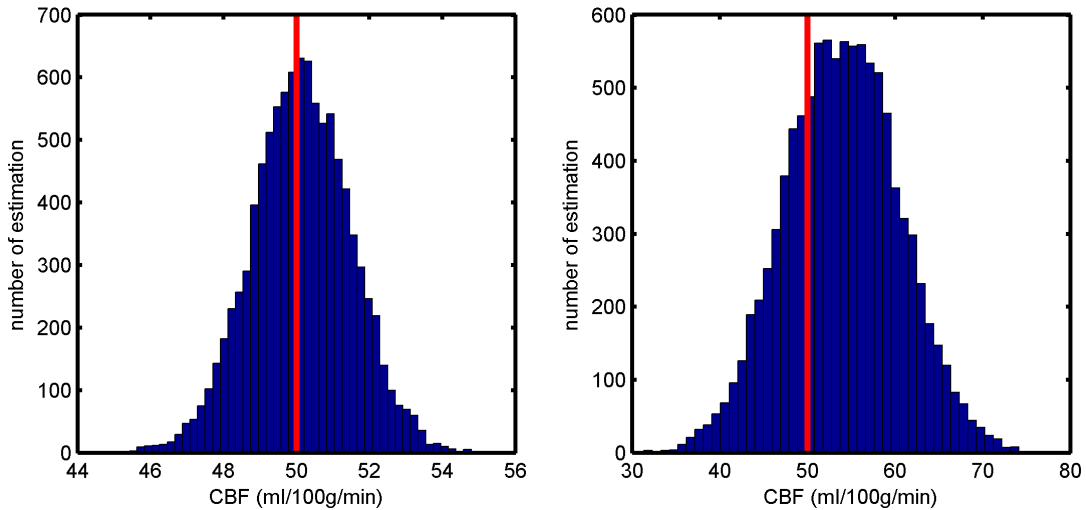


Figure 5.2: Biased estimation by a LS estimator in the presence of Rician noise with low SNR. Left: With high SNR ($\text{SNR} = 10$ for each measurement), the LS estimator yielded accurate CBF estimation in the presence of Rician noise. Right: With low SNR ($\text{SNR} = 2$ for each measurement), the Rician noise resulted in a biased CBF estimate with a LS estimator.

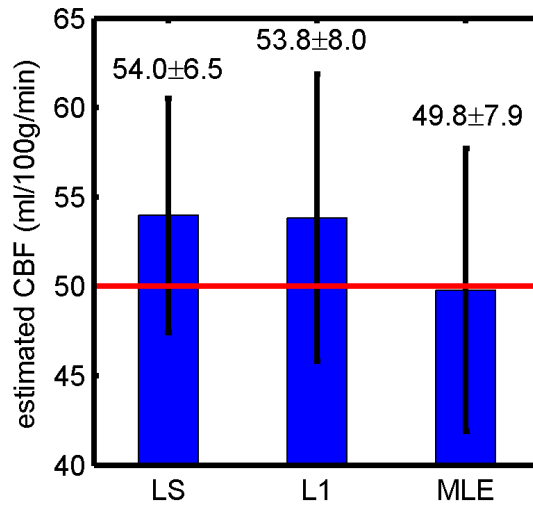


Figure 5.3: Maximum likelihood estimator provides unbiased estimation. With Rician noise and low SNR ($\text{SNR} = 2$ for each measurement), both the LS and L1 estimators resulted in biased estimation. The designed maximum likelihood estimator provided accurate CBF. The true CBF is 50 ml/100g/min.

results.

In the practical situation with low SNR Rician noise, we verified the performance of optimal OT designs with different noise models, as shown in Fig. 5.4. Three sampling schemes were chosen : evenly spaced OTs, optimal OTs based on a Gaussian noise model and optimal OTs based on a Rician noise model (shown on the left) with low SNR ($\text{SNR} = 2$) Rician noise. The estimation results on the right show that the optimal OT designs gave more precise result than the evenly spaced OT designs, and the results were improved by using the Rician model instead of the Gaussian model.

An experimental result is shown in Fig. 5.5. The CBF map with optimal OT design has less noise in the background than the map based on evenly spaced OTs. However, this preliminary result is insufficient to prove the benefit of optimal OT design.

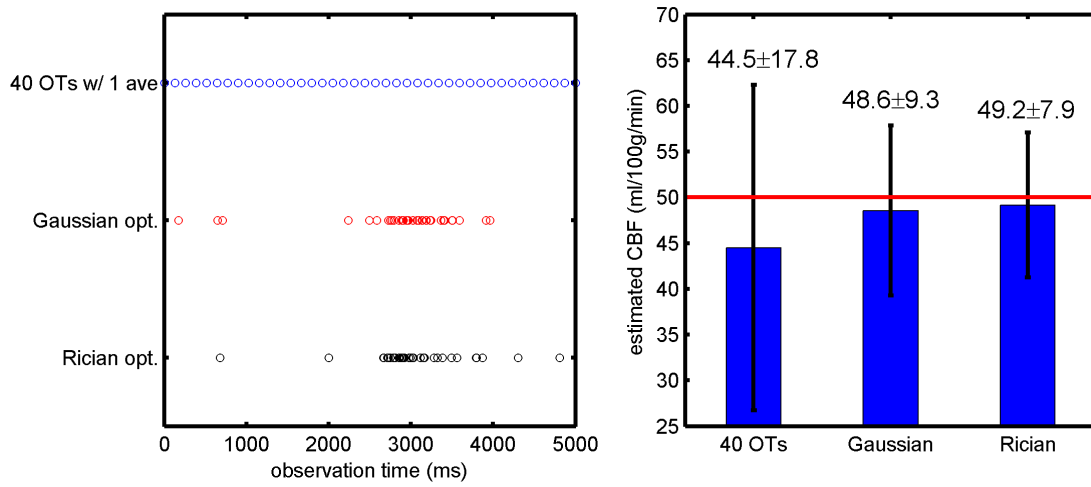


Figure 5.4: Comparison of optimal observation time designs. Left: OT designs used for the simulations: evenly-spaced samples; optimal OT design assuming Gaussian noise; and optimal OT design assuming Rician noise. Right: Simulations performed with Rician noise and low SNR ($\text{SNR} = 2$ for each measurement). The CBF values were estimated using the proposed maximum likelihood estimator. The optimal OT designs yielded more accurate and more precise estimates than the evenly-spaced design. The Rician OT design yielded more precise estimates than the Gaussian OT design.

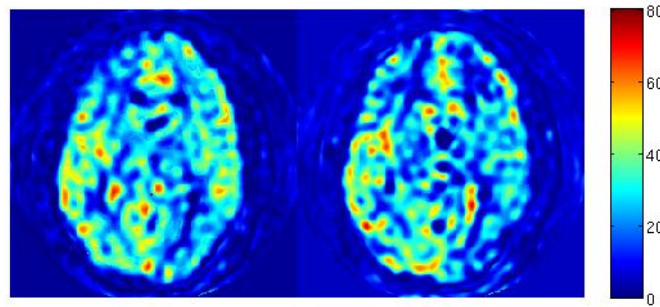


Figure 5.5: Optimal OTs experiment result. Left figure is the CBF map with optimal design with 40 OTs and 2 average. Right figure is the control scan with 5 OTs with 16 average each. CBF maps are shown in ml/100g/min.

5.5 Discussion

In this work, we have initial results showing that optimizing OTs can achieve significantly improved estimation performance, regardless of noise model. ASL imaging is a natural fit for this design, because it requires a large number of measurements to improve image quality and SNR. The proposed method can exploit the scan time more efficiently and enable dynamic ASL imaging instead of conventional averaging. Furthermore, ASL images have intrinsically low SNR, which makes it more important to design the OTs carefully to improve CBF quantification and save scan time.

The LS estimator resulted in lower variance than the L1 estimator with Gaussian noise, as shown in Fig. 5.1. This is consistent with theory; the efficient maximum likelihood estimator reduces to a LS estimator with a Gaussian noise model.

With low SNR and Rician noise, LS estimation results in biased estimation, whereas MLE with a Rician noise model gives the correct value. We should also note that although the Rician MLE is unbiased, it has slightly higher variance than the LS estimator, as shown in Fig. 5.3. This is because the variance of estimation depend on both the Fisher information matrix and the estimator. One explanation can be found in the CRLB with Gaussian noise model of Eq. 5.30, where the estimator ψ also limits the variance of x . We could achieve lower variance (mean squared error) when we use a biased estimator. Therefore, an interesting question arises: do we prefer a biased estimate with a lower variance or an unbiased estimate?

The optimal OT design with Rician noise model shows slight improvement compared to optimal Gaussian design. Both designs are significantly better than averaging at evenly-spaced OTs.

The optimal OT design for ASL was difficult to validate experimentally. There are two possible reasons. First, the experiment was contaminated by physiological noise. The optimal OTs are designed for minimizing thermal noise from the MRI system. However, ASL usually contains physiological noise, such as body motion and resting state blood flow changes, which could dominate the result. Second, the result is not statistically significant. To show the improvement statistically, we used 10000 repetitions in the simulations. Therefore, one experiment lacks the power to demonstrate the improvement.

This method is proposed as an optimization for ASL parameter estimation with the Buxton perfusion model [14], but it can be adapted into more complex model, such as first pass perfusion with dispersed AIF [23]. A smooth perfusion model without discontinuity could distribute OTs more widely when solved by a similar algorithm. But a more complex model could require more sample points to show improvement. It can also be adapted into other parameter mapping designs, such as T_1 mapping [92] and ADC mapping in diffusion imaging [98]. A simple signal model (e.g., T_1 decay model) could yield an optimized result and improve the stability of estimation.

The uncertainty of reference parameters influences the performance of OT design. Typically, several of the parameters in the ASL model are not estimated; the CBF is calculated based on a series of reference values, such as T_1 and M_0 . The variations of these reference values have an impact on the precision of CBF estimation, which is ignored in the current work. More accurate methods could follow the Bayesian framework [97] to consider the variance of input parameters. Furthermore, the design of optimal OTs is based on the assumption of pre-targeted CBF and ATT. In this work, we used 50 ml/100g/min for CBF and 700 ms for ATT. If the measured CBF is different from this designed value, the proposed method can

still provide improved estimates. However, the tolerance to this deviation requires further study.

Sampling pattern design has been discussed in 2D and 3D spatial domains, but it is underdeveloped in the temporal domain. Most compressed sensing performed on dynamic imaging or parameter estimation is randomly (Poisson or multi-level [72]) sampled in the spatial domain, but evenly sampled in t-space or p-space. Optimal OT design demonstrates that a non-uniform sampling pattern is more efficient to exploit the information in p-space. There is more theoretical work needed to combine the two domains of undersampling pattern design in parameter space compressed sensing.

5.6 Conclusion

Optimal observation time design for dynamic ASL can reduce CBF estimation variance significantly without extra scan time. With low SNR, a maximum likelihood estimator should be used for unbiased estimation in the typical Rician noise situation, instead of a conventional least squared error estimator.

5.A Derivation of CRLB with Gaussian Noise

For the measurements with additive Gaussian noise n and standard deviation σ :

$$y = f(x) + n \tag{5.22}$$

$$y - f(x) = n \sim N(0, \sigma^2) \tag{5.23}$$

In the experiment of N measurements, the covariance matrix of noise is $N \times N$:

$$E[nn'] = C \quad (5.24)$$

The joint probability density function of y on parameter x is also Gaussian distributed:

$$p(y|x) = A \exp[-0.5(y - f(x))'C^{-1}(y - f(x))] \quad (5.25)$$

$$\ln p(y|x) = \ln A - 0.5(y - f(x))'C^{-1}(y - f(x)) \quad (5.26)$$

The maximum of the likelihood function is determined using a first order differential equation:

$$\frac{\partial \ln p(y|x)}{\partial x} = (y - f(x))'C^{-1} \frac{\partial f(x)}{\partial x} \quad (5.27)$$

Because C is a symmetric matrix, the Fisher information matrix can be expressed as:

$$\left(\frac{\partial \ln p(y|x)}{\partial x} \right)^2 = \left(\frac{\partial f(x)}{\partial x} \right)' C^{-1} (y - f(x)(y - f(x))'C^{-1} \frac{\partial f(x)}{\partial x} \quad (5.28)$$

We can simplify the above equation as:

$$E \left[\left(\frac{\partial \ln p(y|x)}{\partial x} \right)^2 \right] = \left(\frac{\partial f(x)}{\partial x} \right)' C^{-1} \left(\frac{\partial f(x)}{\partial x} \right) \quad (5.29)$$

From CRLB 5.3, we can get

$$E[(\hat{x} - x)^2|x] \geq \frac{\left(\frac{\partial \psi(x)}{\partial x} \right)^2}{\left(\frac{\partial f(x)}{\partial x} \right)' C^{-1} \left(\frac{\partial f(x)}{\partial x} \right)} \quad (5.30)$$

where

$$\hat{x} = \psi(x) = x + \varphi(x) \quad (5.31)$$

$\varphi(x)$ is the bias. If the Gaussian noise is i.i.d. and estimator $\psi(x)$ is unbiased:

$$C = \sigma^2 I \quad (5.32)$$

$$E[(\hat{x} - x)^2 | x] \geq \sigma^2 \frac{1}{\left(\frac{\partial f(x)}{\partial x}\right)' \left(\frac{\partial f(x)}{\partial x}\right)} \quad (5.33)$$

5.B Derivation pf CRLB of ASL model with Gaussian Noise

For the typical single compartment ASL perfusion model [14]:

$$\Delta M = 2M_0 \alpha f T_1 \exp\left(-\frac{\Delta t}{T_{1,b}}\right) Q(t) \quad (5.34)$$

$$Q(n) = \begin{cases} 0 & \text{if } 0 < t < \Delta t \\ 1 - \exp\left(-\frac{t-\Delta t}{T_1}\right) & \text{if } \Delta t \leq t \leq \Delta t + \tau \\ \exp\left(-\frac{t-\tau-\Delta t}{T_1}\right) - \exp\left(-\frac{t-\Delta t}{T_1}\right) & \text{if } \Delta t + \tau < t \end{cases} \quad (5.35)$$

We assume the measured signal contains additive white Gaussian noise.

$$S = \Delta M + n \quad (5.36)$$

Suppose we have N measurements and the probability density function is $p(S(t_i, f))$.

$$p(S, f) = \frac{1}{(2\pi\sigma^2)^{N/2}} \exp \left[-\frac{1}{2\sigma^2} \sum_{i=1}^N (S(t_i) - \Delta M(t_i))^2 \right] \quad (5.37)$$

$$\ln p(S, f) = \text{const.} - \frac{1}{2\sigma^2} \sum_{i=1}^N (S(t_i) - \Delta M(t_i))^2 \quad (5.38)$$

As mentioned in Equation 5.3 and 5.33, both f and Δt will be estimated. The Fisher Information Matrix is

$$\mathcal{F} = E \begin{bmatrix} \sum \left(\frac{\partial \Delta M}{\partial f} \right)^2 & \sum \frac{\partial \Delta M}{\partial f} \frac{\partial \Delta M}{\partial \Delta t} \\ \sum \frac{\partial \Delta M}{\partial \Delta t} \frac{\partial \Delta M}{\partial f} & \sum \left(\frac{\partial \Delta M}{\partial \Delta t} \right)^2 \end{bmatrix} \quad (5.39)$$

To achieve the lower bound:

$$\frac{\partial \Delta M}{\partial f} = 2M_0\alpha T_1 \exp \left(-\frac{\Delta t}{T_{1,b}} \right) Q \quad (5.40)$$

$$\frac{\partial \Delta M}{\partial \Delta t} = \begin{cases} 0 \\ 2M_0\alpha f T_1 \left(-\frac{1}{T_{1,b}} \exp(-\frac{\Delta t}{T_{1,b}}) + \left(\frac{1}{T_{1,b}} - \frac{1}{T_1} \right) \exp(-\frac{\Delta t}{T_{1,b}}) \exp(-\frac{t-\Delta t}{T_1}) \right) \\ 2M_0\alpha f T_1 \left(1 - \exp(-\frac{\tau}{T_1}) \right) \left(\frac{1}{T_1} - \frac{1}{T_{1,b}} \right) \exp(-\frac{\Delta t}{T_{1,b}}) \exp(-\frac{t-\Delta t-\tau}{T_1}) \end{cases} \quad (5.41)$$

The estimation of CBF is limited by the Fisher information matrix:

$$\text{var}(f) \geq \mathcal{F}^{-1}(1, 1) \quad (5.42)$$

To minimize the variance of CBF, the optimization is performed as follow:

$$\hat{t} = \arg \min_t \frac{\mathcal{F}(2, 2)}{\mathcal{F}(1, 1)\mathcal{F}(2, 2) - \mathcal{F}(1, 2)\mathcal{F}(2, 1)} \quad (5.43)$$

Conclusion

6.1 Overview of Findings

ASL has been improved significantly over the past 20 years, but low SNR remains its primary limitation. As mentioned in the Introduction, the primary goal of this dissertation was to develop accurate and accelerated ASL techniques for a limited scan time, in order to promote dynamic imaging. Chapter 2 focuses on a new method for accelerated parameter mapping. While this technique has not yet been directly applied to ASL, it could be used to estimate relaxation time parameters needed for ASL quantification. Chapters 3, 4 and 5 address ASL problems associated with robust measurement at a single delay time and dynamic ASL imaging, with discussion of image quality and accuracy of quantification.

Prior to describing the main work, we briefly reviewed the current status of ASL, including clinical applications, theory, perfusion models, pulse sequences and intrinsic problems.

Chapter 2 describes a new method for parameter mapping. As a parameter estimation problem, ASL quantification is highly dependent on other reference parameters, such as T_1 and T_2 . We propose the first use of the unscented Kalman filter for parameter estimation

in MRI. This method treats relaxation weighting as encoding states in parameter-space, so as to estimate the desired parameter directly from k-space data. It enables a high under-sampling ratio, maintains the accuracy of the parameter map and reduces computational complexity. This chapter focuses on demonstrating this method for accelerated T_2 mapping. But the proposed method can be adapted to other parameter estimation problems, such as T_1 mapping.

Chapter 3 attempts to develop a robust single post label delay ASL imaging method. 3D spiral turbo spin echo is a rapid and SNR-efficient readout sequence, which addresses the speed and SNR limitations of ASL. Interleaved spiral acquisition yields improved resolution and reduces susceptibility artifacts, but multi-shot readout makes the scan more sensitive to patient and physiological motion (e.g., flow in large vessels). Image reconstruction using parallel imaging improves data consistency and accelerates image acquisition. A single-shot 3D ASL was developed with a dual-density spiral k-space trajectory, which provides moderate resolution and freezes motion artifacts. Spatial sparsity of the ASL image is used to improve the image quality further.

Chapter 4 describes improvements in dynamic ASL imaging. To achieve reliable and accurate fits to a perfusion model requires data at multiple observation times, instead of a single post label delay. This additional parameter space dimension is similar to temporal sampling. We can improve image quality and CBF estimation by introducing k-p space sparsity, which uses the similar spatial structure from different image frames and prior knowledge about temporal ASL signal evolution. Instead of conventional reconstruction of each measurement, we efficiently use the relationship of images from different observation times to improve the image quality and the CBF estimation, by exploiting the model-based sparsity

of multi-observation-time ASL perfusion images.

Chapter 5 discusses the dynamic ASL sampling pattern and quantification. Since the SNR is even lower in dynamic ASL, it is important to improve the calculation accuracy in both dynamic experiment design and perfusion parameter estimation. The dynamic information is efficiently exploited by observation time design according to the Cramér-Rao lower bound, instead of averaging naively. However, low SNR breaks the Gaussian noise assumption and result in biased CBF in conventional least squared error estimation. Therefore, a more realistic Rician noise model is adapted into observation time design and estimator design.

6.2 Future Directions

6.2.1 Sequence

3D stack-of-spirals

As a general 3D acquisition method, stack-of-spirals has potential applications requiring fast imaging.

The main competitor of stack-of-spirals is 3D GRASE (stack-of-EPIs). Recent research has compared GRASE and stack-of-spirals in ASL [99, 100]. The results confirm the SNR efficiency of 3D sequences and suggest that the performance mainly depends on the echo time and length of readout. The spiral trajectory is more motion robust, because it has nearly null gradient moments at the center of k-space. This should make stack-of-spirals a preferable sequence for motion sensitive imaging, such as ASL, but confirming this requires further study of repeatability.

Off-resonance results in blurring in spiral images. Therefore, some groups prefer multiple interleaved spirals with short readouts. However, this strategy will introduce motion among the interleaves. An alternative strategy is single-shot dual-density spiral as proposed in this work, which freezes motion within each measurement. This strategy also covers more of the center of k-space, which has the potential to improve SNR.

In the single-shot dual-density spiral trajectory, k-space is fully-sampled at the center and undersampled at outer k-space. The images are recovered by a parallel reconstruction method. According to the undersampling scheme of compressed sensing, a multiple levels sampling scheme [101] should be performed to increase incoherence of MRI data. An optimal-density spiral trajectory can be designed according to the multiple level scheme, which could increase the coverage and spatial resolution further.

ASL Tagging

ASL was developed based on tagging RF pulses followed by preparation RF pulses. The pCASL tagging pulse mimics the flow driven inversion condition by splitting the long RF into a large number of short duration RFs. There are two problems in this approximation: high SAR, which prolongs the scan time, and unknown tagging efficiency, which limits the accuracy in quantification. A systematic RF pulse design could improve the performance of tagging pulses.

The dynamic ASL imaging in this work is performed by multiple observation time measurements. The SNR can be increased by Hadamard encoding.

6.2.2 Model-based Reconstruction

In k-space, an incoherent sampling pattern promotes noise-like artifacts and successful image recovery by compressed sensing reconstruction. An optimized k-t sampling pattern could improve performance by including different spatial and temporal information. Cartesian k-space can be optimized by selecting which phase encoding steps to omit, and the sampling pattern of a spiral trajectory can be optimized by choosing the initial angle of the spiral trajectory. However, since we are mainly concerned with noise and motion artifacts, not under-sampling artifacts, the compressed sensing reconstruction might not produce the theoretical improvements from sampling pattern optimization in practice.

However, sampling design in the parameter encoding space is still interesting. Most compressed sensing performed on dynamic imaging or parameter estimation is randomly (or pseudo randomly) sampled in the spatial domain, but evenly sampled in the temporal domain. Optimal OT design results in a non-uniform sampling pattern in parameter space. There is more theoretical work needed to combine the two domains in undersampling pattern design of parameter space with compressed sensing.

6.2.3 Parameter Tracking

The parameter tracking in Chapter 2 has a high undersampling factor in k-space, but still requires a large number of samples in p-space. If the prior knowledge is accurate enough, measurement of proton density in a separate scan could further improve the Kalman filter, as shown in the simulation. In this design, we did not include Kalman filter training for the matrices. Actually, these matrices are 'trained' in the first few iterations by the under-

sampled data. This can slow down the Kalman filter convergence and limit the estimation map accuracy. An alternative approach is to train these matrices with separately acquired data.

By treating each echo in a TSE sequence as having a different TE, we can view the data in k-p space, which may help to solve T_2 -shadowing in a TSE sequence and has the potential for single-shot T_2 mapping.

6.3 Collaborations and Contributions

The work in this dissertation includes a lot of contributions from collaborators. I would like to sincerely thank them for their efforts here.

The spiral techniques are the teamwork of Dr. Meyer's lab. The spiral offline reconstruction was mostly modified by Dr. Xue Feng. The gridding reconstruction of spirals with Chebyshev approximation was originally developed by Dr. Weitian Chen and Dr. Christopher Sica. The 3D sequence with turbo spin echo and stack-of-spirals was developed by Dr. Samuel Fielden. Of course, Dr. Craig Meyer guided all of the work and discussed most of the ideas.

Bibliography

- [1] Fielden SW, Mugler JP, Hagspiel KD, Norton PT, Kramer CM, Meyer CH. Non-contrast peripheral MRA with spiral echo train imaging. *Magnetic Resonance in Medicine*. 2014;. iii, 48, 49, 76
- [2] Lin DDM, Kleinman JT, Wityk RJ, Gottesman RF, Hillis AE, Lee AW, et al. Crossed cerebellar diaschisis in acute stroke detected by dynamic susceptibility contrast MR perfusion imaging. *American Journal of Neuroradiology*. 2009;30(4):710–5. 1
- [3] Thomsen HS. Nephrogenic systemic fibrosis: A serious late adverse reaction to gadodiamide. *European Radiology*. 2006;16(12):2619–21. 1
- [4] Weinreb JC, Abu-Alfa AK. Gadolinium-based contrast agents and nephrogenic systemic fibrosis: why did it happen and what have we learned? *Journal of Magnetic Resonance Imaging*. 2009;30(6):1236–1239. 1, 2
- [5] Williams DS, Detre JA, Leigh JS, Koretsky AP. Magnetic resonance imaging of perfusion using spin inversion of arterial water. *Proceedings of the National Academy of Sciences of the United States of America*. 1992;89(1):212–6. 1, 7
- [6] Detre JA, Leigh JS, Williams DS, Koretsky AP, Leight JS. Perfusion imaging. *Magnetic Resonance in Medicine*. 1992;23(1):37–45. 1, 7, 8
- [7] Wang DJJ, Alger JR, Qiao JX, Hao Q, Hou S, Fiaz R, et al. The value of arterial spin-labeled perfusion imaging in acute ischemic stroke: comparison with dynamic susceptibility contrast-enhanced MRI. *Stroke; a journal of cerebral circulation*. 2012;43(4):1018–1024. 3, 13, 48
- [8] Lauterbur PC. Image Formation by Induced Local Interactions: Examples Employing Nuclear Magnetic Resonance. *Nature*. 1973;242(5394):190–191. 3
- [9] Liang ZP, Lauterbur PC. Principles of magnetic resonance imaging: a signal processing perspective. SPIE Optical Engineering Press; 2000. 3
- [10] Nishimura DG. Principles of magnetic resonance imaging. Stanford University; 1996.

- [11] Haacke EM, Brown RW, Thompson MR, Venkatesan R. *Magnetic Resonance Imaging: Physical Principles and Sequence Design*. Wiley; 1999. 3
- [12] Buxton RB. *Introduction to Functional Magnetic Resonance Imaging: Principles and Techniques*. Cambridge University Press; 2009. 5
- [13] Wintermark M, Sesay M, Barbier E, Borbely K, Dillon WP, Eastwood JD, et al. Comparative overview of brain perfusion imaging techniques. *Stroke; a journal of cerebral circulation*. 2005;36(9):e83–99. 6, 7
- [14] Buxton RB, Frank LR, Wong EC, Siewert B, Warach S, Edelman RR. A general kinetic model for quantitative perfusion imaging with arterial spin labeling. *Magnetic Resonance in Medicine*. 1998;40(3):383–396. 7, 12, 72, 91, 102, 109, 112
- [15] Zhou J, Wilson DA, Ulatowski JA, Traystman RJ, van Zijl PCM. Two-Compartment Exchange Model for Perfusion Quantification Using Arterial Spin Tagging. *Journal of Cerebral Blood Flow & Metabolism*. 2001;21:440–455. 7
- [16] Fanea L, David LI, Lebovici A, Carbone F, Sfrangeu SA. Theoretical Compartment Modeling of DCE-MRI Data Based on the Transport across Physiological Barriers in the Brain. *Computational and Mathematical Methods in Medicine*. 2012;. 7
- [17] Lu H, Clingman C, Golay X, Zijl PCMV. Determining the Longitudinal Relaxation Time (T1) of Blood at 3.0 Tesla. *Magnetic Resonance in Medicine*. 2004;682:679–682. 13
- [18] Ethofer T, Mader I, Seeger U, Helms G, Erb M, Grodd W, et al. Comparison of Longitudinal Metabolite Relaxation Times in Different Regions of the Human Brain at 1.5 and 3 Tesla. *Magnetic Resonance in Medicine*. 2003;1301:1296–1301. 13
- [19] Alsop DC, Detre Ja. Reduced transit-time sensitivity in noninvasive magnetic resonance imaging of human cerebral blood flow. *Journal of cerebral blood flow and metabolism*. 1996;16(6):1236–1249. 13, 68
- [20] Dai W, Robson PM, Shankaranarayanan A, Alsop DC. Reduced resolution transit delay prescan for quantitative continuous arterial spin labeling perfusion imaging. *Magnetic Resonance in Medicine*. 2012;67(5):1252–1265. 13, 17, 68, 72, 81
- [21] Chen Y, Wang Z, J A Detre. Impact of Equilibrium Magnetization of Blood on ASL Quantification. *Proc Intl Soc Mag Reson Med*. 2011;19(1):2011. 14
- [22] Çavuşoğlu M, Pfeuffer J, Uğurbil K, Uludağ K. Comparison of pulsed arterial spin labeling encoding schemes and absolute perfusion quantification. *Magnetic resonance imaging*. 2009;27(8):1039–1045. 14
- [23] Calamante F. Arterial input function in perfusion MRI: A comprehensive review. *Progress in Nuclear Magnetic Resonance Spectroscopy*. 2013;74:1–32. 15, 91, 109

- [24] Petersen ET, Lim T, Golay X. Model-free arterial spin labeling quantification approach for perfusion MRI. *Magnetic Resonance in Medicine*. 2006;55(2):219–232. 15
- [25] Alsop DC, Detre JA, Golay X, Günther M, Hendrikse J, Hernandez-Garcia L, et al. Recommended implementation of arterial spin-labeled perfusion MRI for clinical applications: A consensus of the ISMRM perfusion study group and the European consortium for ASL in dementia. *Magnetic Resonance in Medicine*. 2014;00:n/a–n/a. 15, 17
- [26] Wong EC. An Introduction to ASL Labeling Techniques. *Journal of Magnetic Resonance Imaging*. 2014;40:1–10.
- [27] Golay X, Hendrikse J, Lim TCC. Perfusion Imaging Using Arterial Spin Labeling. *Top Magn Reson Imaging*. 2004;15:10–27.
- [28] Wong EC. Quantifying CBF With Pulsed ASL: Technical and Pulse Sequence Factors. *Journal of Magnetic Resonance Imaging*. 2005;22(6):727–731. 15
- [29] Alsop DC, Detre JA. Multisection cerebral blood flow MR imaging with continuous arterial spin labeling. *Radiology*. 1998;208:410–416. 16
- [30] Wang J, Zhang Y, Wolf RL, Roc AC, Alsop DC, Detre JA. Amplitude-modulated Continuous Arterial Spin-labeling 3.0-T Perfusion MR Imaging with a Single Coil: Feasibility Study1. *Radiology*. 2005;235:218–228.
- [31] Wu WCC, Wang J, Detre JA, Ratcliffe SJ, Floyd TF. Transit delay and flow quantification in muscle with continuous arterial spin labeling perfusion-MRI. *Journal of Magnetic Resonance Imaging*. 2008;28:445–452. 16
- [32] Wong EC, Buxton RB, Frank LR. Implementation of Quantitative Perfusion Imaging Techniques for Functional Brain Mapping using Pulsed Arterial Spin Labeling [Journal article]. *NMR in Biomedicine*. 1997;10:237–249. 16
- [33] Golay X, Stuber M, Pruessmann KP, Meier D, Boesiger P. Transfer insensitive labeling technique (TILT): application to multislice functional perfusion imaging. *Journal of magnetic resonance imaging*. 1999;9(3):454–61. 16
- [34] Kim SG. Quantification of relative cerebral blood flow change by flow-sensitive alternating inversion recovery (FAIR) technique: application to functional mapping. *Magnetic Resonance in Medicine*. 1995;34(3):293–301. 16
- [35] Wong EC, Cronin M, Wu WC, Inglis B, Frank LR, Liu TT. Velocity-selective arterial spin labeling. *Magnetic Resonance in Medicine*. 2006;55(6):1334–1341. 16
- [36] Zun Z, Wong EC, Nayak KS. Assessment of Myocardial Blood Flow (MBF) in Humans Using Arterial Spin Labeling (ASL): Feasibility and Noise Analysis [Journal article]. *Magnetic Resonance in Medicine*. 2009;62:975–983. 16

- [37] Guo J, Wong EC. Pulmonary Blood Flow Measurement using Velocity-Selective Arterial Spin Labeling at 3.0T. *Proc Intl Soc Mag Reson Med*. 2013;21:2149. 16, 18
- [38] Garcia D, de Bazelaire C, Alsop DC. Pseudo-continuous Flow Driven Adiabatic Inversion for Arterial Spin Labeling. In: *Proc. Intl. Soc. Mag. Reson. Med.*; 2005. p. 37. 16
- [39] Dai W, Garcia D, de Bazelaire C, Alsop DC. Continuous Flow-Driven Inversion for Arterial Spin Labeling Using Pulsed Radio Frequency and Gradient Fields. *Magnetic Resonance in Medicine*. 2008;60(6):1488–1497. 49, 50, 74
- [40] Wu WC, Fernández-Seara M, Detre JA, Wehrli FW, Wang J. A theoretical and experimental investigation of the tagging efficiency of pseudocontinuous arterial spin labeling. *Magnetic Resonance in Medicine*. 2007;58(5):1020–1027. 16, 50
- [41] Jung Y, Wong EC, Liu TT. Multiphase pseudocontinuous arterial spin labeling (MP-PCASL) for robust quantification of cerebral blood flow. *Magnetic Resonance in Medicine*. 2010;64:799–810. 17
- [42] Chappell MA, Okell TW, Jezzard P, Woolrich MW. A general framework for the analysis of vessel encoded arterial spin labeling for vascular territory mapping. *Magnetic Resonance in Medicine*. 2010;64:1529–39. 17
- [43] Ye FQ, Mattay VS, Jezzard P, Frank JA, Weinberger DR, McLaughlin AC. Correction for Vascular Artifacts in Cerebral Blood Flow Values Measured by Using Arterial Spin Tagging Techniques. *Magnetic Resonance in Medicine*. 1997;37:226–235. 17
- [44] Wong EC, Buxton RB, Frank LR. Quantitative Imaging of Perfusion Using a Single Subtraction (QUIPSS and QUIPSS 11). *Magnetic Resonance in Medicine*. 1998;39:702–708. 17
- [45] Luh WM, Wong EC, Bandettini PA, Hyde JS. QUIPSS II With Thin-Slice TI 1 Periodic Saturation: A Method for Improving Accuracy of Quantitative Perfusion Imaging Using Pulsed Arterial Spin Labeling. *Magnetic Resonance in Medicine*. 1999;41(6):1246–1254. 17
- [46] Ye FQ, Frank JA, Weinberger DR, McLaughlin AC. Noise Reduction in 3D Perfusion Imaging by Attenuating the Static Signal in Arterial Spin Tagging (ASSIST). *Magnetic Resonance in Medicine*. 2000;44(1):92–100. 17, 68
- [47] Maleki N, Dai W, Alsop DC. Optimization of background suppression for arterial spin labeling perfusion imaging. *Magnetic Resonance Materials in Physics, Biology and Medicine*. 2011;25(2):127–133. 17, 68
- [48] Garcia DM, Duhamel G, Alsop DC. Efficiency of inversion pulses for background suppressed arterial spin labeling. *Magnetic Resonance in Medicine*. 2005;54(2):366–372. 17, 68

- [49] Vidorreta M, Wang Z, Rodríguez I, Pastor MA, Detre JA, Fernández-Seara MA. Comparison of 2D and 3D single-shot ASL perfusion fMRI sequences. *Neuroimage*. 2013;66:662–671. 18
- [50] MacIntosh BJ, Filippini N, Chappell MA, Woolrich MW, Mackay CE, Jezzard P. Assessment of arterial arrival times derived from multiple inversion time pulsed arterial spin labeling MRI. *Magnetic Resonance in Medicine*. 2010;63(3):641–647. 19
- [51] Günther M, Bock M, Schad LR. Arterial spin labeling in combination with a look-locker sampling strategy: inflow turbo-sampling EPI-FAIR (ITS-FAIR). *Magnetic Resonance in Medicine*. 2001;46(5):974–984. 19
- [52] Wells JA, Lythgoe MF, Gadian DG, Ordidge RJ, Thomas DL. In Vivo Hadamard Encoded Continuous Arterial Spin Labeling (H-CASL). *Magnetic Resonance in Medicine*. 2010;63(4):1111–1118. 19, 91
- [53] Dai W, Shankaranarayanan A, Alsop DC. Arterial Transit Delay Effects on Perfusion Measurement in an Elderly Cohort. *Proc Intl Soc Mag Reson Med*. 2013;69(4):2192. 19, 91
- [54] Chan I, Wells W, Mulkern RV, Haker S, Zhang J, Zou KH, et al. Detection of prostate cancer by integration of line-scan diffusion, T2-mapping and T2-weighted magnetic resonance imaging; a multichannel statistical classifier. *Medical Physics*. 2003;30(9):2390–2398. 22
- [55] Oh J, Cha S, Aiken AH, Han ET, Crane JC, Stainsby JA, et al. Quantitative apparent diffusion coefficients and T2 relaxation times in characterizing contrast enhancing brain tumors and regions of peritumoral edema. *Journal of Magnetic Resonance Imaging*. 2005;21(6):701–708. 22
- [56] Siemonsen S, Mouridsen K, Holst B, Ries T, Finsterbusch J, Thomalla G, et al. Quantitative t2 values predict time from symptom onset in acute stroke patients. *Stroke; a journal of cerebral circulation*. 2009;40(5):1612–1616. 22
- [57] Giri S, Chung YC, Merchant A, Mihai G, Rajagopalan S, Raman SV, et al. T2 quantification for improved detection of myocardial edema. *Journal of cardiovascular magnetic resonance*. 2009 Jan;11(1):56. 22
- [58] Baudrexel S, Nürnberger L, Rüb U, Seifried C, Klein JC, Deller T, et al. Quantitative mapping of T1 and T2* discloses nigral and brainstem pathology in early Parkinson's disease. *NeuroImage*. 2010;51(2):512–520. 22
- [59] Liu F, Chaudhary R, Hurley SA, Samosonov A, Alexander A, Deoni SC, et al. Multi-Component T2 Analysis of Cartilage Degradation Model Using mcDESPOT at 3.0T. *Proc Intl Soc Mag Reson Med*. 2013;21:1655. 22
- [60] Velikina JV, Alexander AL, Samsonov A. Accelerating MR parameter mapping using sparsity-promoting regularization in parametric dimension. *Magnetic Resonance in Medicine*. 2013;70(5):1263–1273. 23

- [61] Block KT, Uecker M, Frahm J. Model-based iterative reconstruction for radial fast spin-echo MRI. *IEEE Transactions on Medical Imaging*. 2009;28(11):1759–1769. 23
- [62] Huang C, Graff CG, Clarkson EW, Bilgin A, Altbach MI. T2 mapping from highly undersampled data by reconstruction of principal component coefficient maps using compressed sensing. *Magnetic Resonance in Medicine*. 2012;67(5):1355–1366. 23, 71
- [63] Doneva M, Börnert P, Eggers H, Stehning C, S  n  gas J, Mertins A. Compressed sensing reconstruction for magnetic resonance parameter mapping. *Magnetic Resonance in Medicine*. 2010;64(4):1114–1120. 23, 32, 33
- [64] S  mb  l U, Santos JM, Pauly JM. A practical acceleration algorithm for real-time imaging. *IEEE Transactions on Medical Imaging*. 2009;28(12):2042–2051. 23
- [65] Feng X, Salerno M, Kramer CM, Meyer CH. Kalman filter techniques for accelerated Cartesian dynamic cardiac imaging. *Magnetic Resonance in Medicine*. 2012;69(5):1346–1356. 23
- [66] Wan E, Merwe RVD, Nelson A. Dual Estimation and the Unscented Transformation. *Neural Information Processing Systems*. 2000;p. 666–672. 23
- [67] Welch G, Bishop G. *An Introduction to the Kalman Filter*. University of North Carolina. 2001;. 24
- [68] Wan EA, Merwe RVD. The unscented Kalman filter for nonlinear estimation. *Proceedings of the IEEE 2000 Adaptive Systems for Signal Processing, Communications, and Control Symposium*. 2000;p. 153–158. 29
- [69] Pruessmann KP, Weiger M, Scheidegger MB, Boesiger P. SENSE: sensitivity encoding for fast MRI. *Magnetic Resonance in Medicine*. 1999;42(5):952–962. 30
- [70] Guerquin-Kern M, Lejeune L, Pruessmann KP, Unser M. Realistic analytical phantoms for parallel magnetic resonance imaging. *IEEE Transactions on Medical Imaging*. 2012;31(3):626–636. 32, 62, 78
- [71] Wang Z, Bovik AC, Sheikh HR, Simoncelli EP. Image quality assessment: from error visibility to structural similarity. *IEEE Transactions on Image Processing*. 2004;13(4):600–612. 33, 79
- [72] Adcock B, Hansen AC, Poon C, Roman B. Breaking the coherence barrier: A new theory for compressed sensing. *arXiv preprint arXiv:13020561*. 2013;. 45, 110
- [73] Wu B, Lou X, Wu X, Ma L. Intra- and interscanner reliability and reproducibility of 3D whole-brain pseudo-continuous arterial spin-labeling MR perfusion at 3T. *Journal of Magnetic Resonance Imaging*. 2014;39(2):402–409. 48
- [74] Cutajar M, Thomas DL, Banks T, Clark Ca, Golay X, Gordon I. Repeatability of renal arterial spin labelling MRI in healthy subjects. *Magnetic Resonance Materials in Physics, Biology and Medicine*. 2012;25:145–153. 48

- [75] Gillis Ka, McComb C, Foster JE, Taylor AHM, Patel RK, Morris STW, et al. Inter-study reproducibility of arterial spin labelling magnetic resonance imaging for measurement of renal perfusion in healthy volunteers at 3 Tesla. *BMC Nephrology*. 2014;15:23. 48
- [76] guofan Xu, Rowley HA, Wu G, Alsop DC, Shankaranarayanan A, Dowling M, et al. Reliability and precision of pseudo-continuous arterial spin labeling perfusion MRI on 3.0 T and comparison with ^{15}O -water PET in elderly subjects at risk for Alzheimer's disease. *NMR in Biomedicine*. 2010;23(3):286–293. 48
- [77] Lustig M, Donoho D, Pauly JM. Sparse MRI: The application of compressed sensing for rapid MR imaging. *Magnetic Resonance in Medicine*. 2007;58(6):1182–1195. 48, 54, 68
- [78] Günther M, Oshio K, Feinberg Da. Single-shot 3D imaging techniques improve arterial spin labeling perfusion measurements. *Magnetic Resonance in Medicine*. 2005;54:491–498. 49
- [79] Nishimura DG, Irarrazabal P, Meyer CH. A velocity k-space analysis of flow effects in echo-planar and spiral imaging. *Magnetic Resonance in Medicine*. 1995;33(4):549–556. 49
- [80] Meyer CH, Hu BS, Nishimura DG, Macovski A. Fast spiral coronary artery imaging. *Magnetic Resonance in Medicine*. 1992;28:202–213. 49
- [81] Fielden SW, Meyer CH, Mugler III JP. Variable-flip angle 3D-turbo spin echo imaging utilizing spiral acquisitions. *Proc Intl Soc Mag Reson Med*. 2011;p. 2820. 49, 76
- [82] Lustig M, Pauly JM. SPIRiT: Iterative self-consistent parallel imaging reconstruction from arbitrary k-space. *Magnetic Resonance in Medicine*. 2010;64(2):457–471. 58, 74
- [83] Qiu M, Maguire RP, Arora J, Planeta-Wilson B, Weinzimmer D, Wang J, et al. Arterial Transit Time Effects in Pulsed Arterial Spin Labeling CBF Mapping: Insight From a PET and MR Study in Normal Human Subjects. *Magnetic Resonance in Medicine*. 2010;63(2):374–384. 68
- [84] Dai W, Robson PM, Shankaranarayanan A, Alsop DC. Modified pulsed continuous arterial spin labeling for labeling of a single artery. *Magnetic Resonance in Medicine*. 2010;64(4):975–982. 68
- [85] Aharon M, Elad M, Bruckstein A. K-SVD : An Algorithm for Designing Overcomplete Dictionaries for Sparse Representation. *IEEE Transaction on Signal Processing*. 2006;54(11):4311–4322. 71
- [86] Lingala SG, Hu Y, Dibella E, Jacob M. Accelerated dynamic MRI exploiting sparsity and low-rank structure: k-t SLR. *IEEE Transactions on Medical Imaging*. 2011;30(5):1042–1054. 74

- [87] Duhamel G, de Bazelaire C, Alsop DC. Evaluation of systematic quantification errors in velocity-selective arterial spin labeling of the brain. *Magnetic Resonance in Medicine*. 2003;50(1):145–153. 76
- [88] Mugler JP. Optimized three-dimensional fast-spin-echo MRI. *Journal of Magnetic Resonance Imaging*. 2014;39:745–767. 76
- [89] Wang DJ, Alger JR, Qiao JX, Gunther M, Pope WB, Saver JL, et al. Multi-Delay Multi-Parametric Arterial Spin-Labeled Perfusion MRI in Acute Ischemic Stroke Comparison with Dynamic Susceptibility Contrast Enhanced Perfusion Imaging. *NeuroImage: Clinical*. 2013;3:1–7. 82, 91
- [90] Kay SM. *Fundamentals of Statistical Signal Processing, Volume I: Estimation Theory* (v. 1). 9th ed. Prentice Hall; 1993. 95
- [91] Xie J, Gallichan D, Gunn RN, Jezzard P. Optimal design of pulsed arterial spin labeling MRI experiments. *Magnetic Resonance in Medicine*. 2008;59(4):826–834. 95
- [92] Akçakaya M, Weingärtner S, Roujol S, Nezafat R. On the selection of sampling points for myocardial T1 mapping. *Magnetic Resonance in Medicine*. 2014;00. 95, 109
- [93] Karlsten OT, Verhagen R, Bovée WMMJ. Parameter estimation from Rician-distributed data sets using a maximum likelihood estimator: Application to T1 and perfusion measurements. *Magnetic Resonance in Medicine*. 1999;41(3):614–623. 96, 100
- [94] Gudbjartsson H, Patz S. The Rician distribution of noisy MRI data. *Magnetic Resonance in Medicine*. 1995;34(6):910–914. 99
- [95] Kobayashi H, Mark BL, Turin w. *Probability, Random Processes, and Statistical Analysis*. Cambridge University Press; 2011. 99
- [96] Andersson JLR. Maximum a posteriori estimation of diffusion tensor parameters using a Rician noise model: Why, how and but. *NeuroImage*. 2008;42(4):1340–1356. 101
- [97] Santos N, Sanches JM, Sousa I, Figueiredo P. Optimal sampling and estimation in PASL perfusion imaging. *IEEE Transactions on Biomedical Engineering*. 2011;58(11):3165–74. 101, 109
- [98] Brihuega-Moreno O, Heese FP, Hall LD. Optimization of diffusion measurements using Cramer-Rao lower bound theory and its application to articular cartilage. *Magnetic Resonance in Medicine*. 2003;50(5):1069–76. 109
- [99] Vidorreta M, Wang Z, Rodríguez I, Pastor MA, Detre JA, Fernández-seara MA. *NeuroImage Comparison of 2D and 3D single-shot ASL perfusion fMRI sequences*. *NeuroImage*. 2013;66:662–671. 117
- [100] Vidorreta M, Balteau E, Wang Z, Vita ED, Thomas DL, Detre JA, et al. Whole-brain High-resolution ASL at 3T. *Proc Intl Soc Mag Reson Med*. 2014;22:2699. 117

- [101] Zhao L, Meyer CH. Sampling pattern design for 2D compressed sensing using a multilevel variable-density spiral trajectory. *Proc Intl Soc Mag Reson Med*. 2014;22:1543. 118